

Electronic Thesis and Dissertation Repository

6-13-2018 2:30 PM

Defect-Related Magnetic Properties of Nanostructured Nickel Oxide Thin Films for Solar Cell Applications

Angela E. Ezugwu
The University of Western Ontario

Supervisor
Prof. Giovanni Fanchini
The University of Western Ontario

Graduate Program in Physics
A thesis submitted in partial fulfillment of the requirements for the degree in Master of Science
© Angela E. Ezugwu 2018

Follow this and additional works at: <https://ir.lib.uwo.ca/etd>

 Part of the [Condensed Matter Physics Commons](#)

Recommended Citation

Ezugwu, Angela E., "Defect-Related Magnetic Properties of Nanostructured Nickel Oxide Thin Films for Solar Cell Applications" (2018). *Electronic Thesis and Dissertation Repository*. 5445.
<https://ir.lib.uwo.ca/etd/5445>

This Dissertation/Thesis is brought to you for free and open access by Scholarship@Western. It has been accepted for inclusion in Electronic Thesis and Dissertation Repository by an authorized administrator of Scholarship@Western. For more information, please contact wlsadmin@uwo.ca.

Abstract

Transparent conducting oxides (TCOs) are extensively investigated because of their applications as transparent electrodes in solar cells and light-emitting devices. TCOs of interest include indium-tin oxide, aluminum-doped zinc oxide, nickel oxide (NiO), and their combinations. There is strong interest in NiO because no heteroatoms are required to “dope” it at high transparency levels. It has been speculated that paramagnetic defects due to Ni³⁺ centers and O interstitials are responsible for the electrical conductivity of otherwise insulating and antiferromagnetic NiO, but direct investigation of such defects has been limited. Here, the electrical conductivity in nanostructured NiO thin films is investigated and correlated to the paramagnetic defect density extracted from electron spin resonance (ESR). Two types of ESR-active centers are identified and assigned, respectively, to localized paramagnetic defects and surface electronic states. Our work points at defect engineering as a necessary step to optimize NiO thin films for their applications as TCOs.

Keywords

Nickel oxide thin films, Electron spin resonance (ESR), Defects, Paramagnetism, Antiferromagnetism, Surface ferromagnetism.

Co-authorship statement

This thesis is partially based on an article “relationship between growth conditions, paramagnetic centers and electrical transport in nickel oxide thin films”, currently submitted to ACS Applied Materials & Interfaces. The list of co-authors includes Dr. Paul Bazylewski, Mr. Victor Wong, and Dr. Giovanni Fanchini. I am the first author in this paper, and have been responsible for carrying out the parametric growth of NiO thin films at different annealing temperature, performing the essential characterization, including atomic force microscopy, and kelvin probe force microscopy technique presented in the paper and in this thesis. Dr. Paul Bazylewski assisted with the electron spin resonance spectroscopy measurements, while Mr. Victor Wong did the work on the magnetic force microscopy measurements. The entire work was conducted under the supervision of Dr. Giovanni Fanchini, and he provided assistance for scientific analysis and editing of the paper and the thesis.

Acknowledgments

I would like to express my sincere gratitude to my supervisor, Prof. Giovanni Fanchini for his continuous support throughout this thesis work. I sincerely want to thank prof. Giovanni for his understanding, guidance and for his useful suggestions and discussions during the writing of this thesis.

I would like to thank the members of Giovanni's group: Victor Wong, Sheldon Van Middelkoop, Edith Yeung, Jaewoo Park, Andason Cen, and Dr. Paul Bazylewski. I sincerely appreciate every one of you for your help in time of difficulties.

It gives me immense pleasure to thank my advisory committee members, Prof. Tamie Poepping and Mahi Singh for their time, useful suggestions and encouragements during advisory committee meetings.

This work was partially characterized at Western University's nanofabrication Facility. Technical assistance from Dr. Todd Simpson and Tim Goldhawk at the Nanofab is gratefully acknowledged.

Finally, I would express a deep sense of gratitude to my family and my lovely kids: Ebubechukwu Ezugwu, Madeliene Ezugwu, and Ifunanya Ezugwu, for their love, prayer and support and also my lovely husband, Dr. Sabastine Ezugwu for his unflinching support and love.

Table of Contents

Abstract	i
Co-Authorship Statement.....	ii
Acknowledgments	iii
Table of Contents	iv
List of Tables	viii
List of Figures	ix
Chapter 1	
1 A Review of nanostructured nickel oxide	1
1.1 Transparent conducting oxides	1
1.2 NiO _x and its applications.....	2
1.3 Magnetic properties of materials	5
1.3.1 Diamagnetism	5
1.3.2 Paramagnetism	7
1.3.3 Ferromagnetism	10
1.3.4 Antiferromagnetism	11
1.4 Theory of magnetism	12
1.5 Neel temperature	13
1.6 Effect of nanostructuring on Neel temperature of NiO _x	14
1.7 Ferromagnetic surfaces in NiO _x	15

1.8	Electrical transport in solids and in NiO _x	16
1.8.1	Extended-state transport in metals / intrinsic semiconductors.....	17
1.8.2	Extended-state transport in doped semiconductors	19
1.8.3	Localized-state transport by hopping	21
1.8.4	The role of defects in hopping processes	22
1.8.5	Charge-compensated Ni vacancies.....	26
1.9	Summary and thesis overview	26
1.10	References	28
Chapter 2		
2	Experimental Techniques.....	32
2.1	Thin film fabrication by solution growth method	33
2.1.1	Fundamental principle of solution growth methods	33
2.1.2	Factors influencing solution-growth deposition	34
2.2	Synthesis of nickel oxide by solution-growth	36
2.2.1	Preparation of stock solutions	36
2.2.2	Substrate cleaning	37
2.2.3	Deposition of Ni(OH):NiO _x	37
2.3	Deposition of Nickel Oxide Powder samples	39
2.4	Sample Characterization	40
2.4.1	X -ray Diffraction	40

2.4.2	Atomic force microscopy	45
2.4.2.1	Contact mode operation of AFM	47
2.4.2.2	Non-contact mode/close-contact mode	48
2.4.2.3	Intermittent-contact (or tapping) mode.	49
2.5	Magnetic force microscopy	49
2.6	Electron spin resonance	50
2.6.1	Microwave power and relaxation times	53
2.6.2	Magnets	54
2.6.3	Radiation source and resonator system	55
2.6.4	Phase-sensitive detection system.....	55
2.6.5	Signal intensity	57
2.6.6	Spin density and areal spin density calculations.....	58
2.7	UV-Visible spectrophotometry	60
2.8	Conclusion	62
2.9	References	62
Chapter 3		
3	Properties of nanostructured NiO _x fabricated from chemical bath deposition method	66
3.1	Structural properties of nanostructured NiO _x thin films.....	67
3.1.1	Morphology and thickness	67

3.1.2	SEM / EDX analysis of NiO _x thin films.....	69
3.1.3	Crystal structure of NiO _x thin films deposited from solution growth method.....	70
3.2	Electrical properties of NiO _x thin films	72
3.2.1	Electrical conductivity	72
3.2.2	The Work function of nanostructured NiO _x thin films	74
3.3	Electron spin resonance	76
3.3.1	Origin of magnetic centers in NiO _x from ESR powder spectra.....	76
3.3.2	ESR signal at varying measuring temperature.....	79
3.3.3	Spin density versus annealing temperature in NiO _x thin films	80
3.3.4	Correlation between electrical conductivity and spin density.....	81
3.4	Magnetic force microscopy (MFM) study of NiO _x films	84
3.5	Conclusion	86
3.6	References	87
Chapter 4		
4	Conclusions and Future work	88
4.1	Conclusions	88
4.2	Future work	90
	Curriculum Vitae	92

List of Tables

Table 1.1: Antiferromagnetic crystals	13
Table 1.2: Review of Neel temperature, a transition ordering temperature for different nanoscale NiO _x system	15
Table 2.1: Comparison of the experimental and theoretical values of the Bragg angle and intensity of XRD reflection of NiO _x showing fcc structure	44

List of Figures

- Figure 1.1:** Schematic drawings of the bulk-heterojunction photovoltaic device structures used here without (a) and with (b) an interfacial electron-blocking layer/hole-transporting layer (EBL/HTL). The chemical structures of PEDOT: PSS and the active layer components P3HT and PCBM are also shown. (c) Energy level diagram of device components referenced to the vacuum level. The published valence and conduction band energies NiO_x as HTL/EBL is shown. [26] Reprinted by permission from the National Academy of Sciences. Copyright (2007).....4
- Figure 1.2:** (a) Schematic illustration of diamagnetism showing the decrease in concentration of magnetic field lines and (b) Diamagnetism due to internal dipolar magnetic field caused by magnetic dipoles induced by Larmor precession in a system of opposite spins.7
- Figure 1.3:** (a) Random orientation of unpaired spins in the absence of external magnetic field and $B = 0$; and (b) preferential orientation of unpaired spins and magnetic moments in direction parallel or antiparallel to the magnetic field at $B \neq 0$. The difference between parallel and antiparallel spin population is approximately inversely proportional to the temperature of the system, which leads to Curie Law.8
- Figure 1.4:** Different temperature behaviour of the susceptibility in paramagnetic systems dominated by localized states (Curie Law, eqn. 1.10) and extended states (Pauli paramagnetism, eqn. 1.12).9
- Figure 1.5:** Three different types of magnetic spin ordering in (a) ferromagnetism with exchange integral $J > 0$; (b) antiferromagnetism with exchange integral $J < 0$; and (c) ferrimagnetism, in which different sublattices have opposite net magnetic moments, with a nearly zero total magnetic moment of the two sublattices.....10

Figure 1.6: Structure of NiO showing antiferromagnetic spin structure: (a) two sublattices of Ni ions and (b) two FCC sublattices of opposite spins with diatomic base. In NiO, oxygen ions have no net magnetic moments and the spin moments of Ni²⁺ ions are aligned anti parallel to each other in adjacent atoms. The Miller indices notation of planes signifies ferromagnetic surfaces as indicated in the structure and only one sublattice faces the plane.....11

Figure 1.7: (a) Electronic band structure of NiO showing a light-electron conduction band and heavy-hole valence band and indirect gap [52] (adapted by permission from Institute of Physics Publishing Ltd National Academy of Sciences. Copyright (2013)); and (b) Simplified band diagram with gap-state defects in NiO_x with possible p-type transport mechanisms by extended states and hopping. Although extended states are a more likely transport process in semiconductors, the heavy-hole, low-mobility valence band of NiO_x suggests hopping as another plausible conductivity mechanism.18

Figure 1.8: Energy diagram of doped semiconductors (a) with donor impurities and (b) acceptor impurities. With increasing temperature, electrons can be excited into conduction band from donor states, and holes can be excited into the valence band from acceptor states.....19

Figure 1.9: Schematic diagram of doped semiconductors: (a) silicon doping with phosphorus adds one electron that diffuses in the conduction band upon thermal activation; (b) silicon doping with aluminum produces one hole that diffuses in the valence band20

Figure 1.10: Hopping transition between two localized states i and j with energies ε_i and ε_j , respectively. The solid and dashed lines show the carrier wave functions on sites i and j , respectively and a is the localization radius.....22

Figure 1.11: Diagram classifying defects in crystalline solids.....23

Figure 1.12: Diagram of point defects in ionic crystal due to (a) vacancies; (b) interstitials (foreign atom or a self-atom) occupying an off-lattice site; and (c) interstitials formed by atoms moving off-site creating, at the same time, a vacancy24

Figure 1.13: (a) The structure of ideal NiO crystal with diatomic (Ni, O) base face-centered cubic, (b) non-stoichiometric NiO_x with the presence of Ni²⁺ ion vacant site is compensated by 2Ni³⁺ centers, (c) NiO_x with vacancy is compensated by either Ni³⁺ ion center or O⁻ and (d) NiO_x with vacancy is compensated by 2O⁻26

Figure 2.1: Figure 2.1: (a) Steps involved in the solution growth method used for the deposition of NiO_x thin film. The set up consists of beaker with precursor solution along with the Pyrex glass substrate inserted in it. (b) Post-deposition heat treatment from low to high temperatures of 225–500°C was used to control the thin film properties. The as-deposited samples and those annealed below 300°C are greenish in color which changes to brownish to black color with increasing annealing temperature. The visually observed changes in the color of the films is expected to be accompanied by changes in the properties of the films and will be investigated in this thesis work.....38

Figure 2.2: Bragg scattering off of a plane of atoms in a crystal. The excess distance traveled by the wave striking the lower plane is $2d\sin\theta$. All points representing planes that can diffract are inside a sphere of finite radius, $2/\lambda$41

Figure 2.3: Debye Scherrer powder diffraction experiment set up comprises of an x-ray source oriented at an angle θ to the sample stage and a detector opposite the source that records the intensity of the diffracted x-ray at 2θ angle. The incident angle of the x-ray can be increased during sample exposure while the detector angle always remains at 2θ above the source path.....42

Figure 2.4: Nonius Kappa CCD powder x-ray facility in the Department of Chemistry at Western University Canada. The diffractometer was used in this work to study the crystal structure of NiO_x thin films at different annealing temperatures.....43

Figure 2.5: Plot of theoretical and experimental scattering intensities versus 2θ angle for NiO_x thin films annealed at 500°C. The experimental intensities match well with the theoretical calculation based on fcc structure.....45

Figure 2.6: The AFM cantilever showing the laser beam centrally positioned on a segmented photodiode at which the cantilever is considered to have zero deflection. Movement of the cantilever during a sample scan deflects the laser beam relative to the initial position and used to reconstruct the topography of the scanned surface at nano/micro scale resolution46

Figure 2.7: Atomic interaction forces between the AFM tip and the sample surface, which classifies the modes of AFM operation into contact, non-contact and tapping modes.....48

Figure 2.8: Zeeman splitting of energy levels of an electron placed in a magnetic Field, B . The absorption of microwave energy causes a transition from a lower energy state to a higher energy state.....51

Figure 2.9: (a) Jeol JES-FA200 ESR spectrometer; and (b) block diagram of the main components of an ESR spectrometer employing magnetic field modulation. The method is utilized to improve the signal/noise ratio by phase-sensitive detection. The principle for obtaining the derivative of the absorption is shown.....53

Figure 2.10: Power saturation curve, in which the signal amplitude is expressed as a function of the square root of the incident microwave power.....54

Figure 2.11: Schematic of phase-sensitive detection system. As the main field is scanned slowly through the EPR line, a small additional oscillating magnetic field, B_m , is applied in the same direction as the main field B . B_m is commonly at 100 kHz. As B_m increases from the value B_{m1} to B_{m2} , the crystal detector output increases from i_1 to i_2 . If the magnitude of B_m is small relative to line width, the detector current oscillating at 100 kHz has a peak-to-peak value that approximates the slope of the absorption curve. Consequently, the output of the 100-kHz phase-sensitive detector is the derivative of the absorption curve.....57

Figure 2.12: (a) Schematic diagram of first derivative of the absorption spectrum, (b) Area under the absorption curve (obtained from double integration) and (c) The number of spins in the sample and is proportional to the area under the curve.....58

Figure 2.13: (a) Chemical structure of TEMPO; and (b) ESR spectrum of TEMPO formed by three equally intense resonance lines due to hyperfine splitting from nuclear spins of nitrogen [46] Adapted by permission from Begell House Inc. Copyright (2011)..... 59

Figure 2.14: Figure 2.14: Schematic diagram of a double beam spectrophotometer. The monochromator ensures that sample is scanned continuously over a range of wavelength at a pre-set scan rate.....61

Figure 3.1: AFM topography images of nanostructured NiO_x thin films annealed at different temperatures of (a) 300°C, (b) 350°C, (c) 400°C, (d) 450°C and (e) 500°C. Images show films with different grain sizes and morphologies: spherical, needle-like, as well as nanobelts and microbelts at increasing annealing temperature.....68

Figure 3.2: Figure 3.2: (a) Contact mode AFM image of NiO_x thin film used to determine the thicknesses, (b) Profile of the line drawn along the substrate-sample interface (red line in (a)). The height of the gap from substrate to sample in the line profile gives the required thickness of the sample, and (c) variation of the thickness of NiO_x thin films with annealing temperatures.....68

Figure 3.3: (a) SEM image of NiO_x thin films obtained using LEO (Zeiss) 1530 field emission microscope shortly before EDX spectra were acquired. (b) EDX spectra showing the composition of NiO_x thin films annealed at 400 °C for 1 h in air and (c) A histogram of the elemental composition from panels (b). Si is from the silicon substrate used to deposit the sample C is impurity in trace amount.....69

Figure 3.4: (a) X-ray diffraction patterns of NiO_x thin films annealed at different temperatures, showing a crystalline face-centered cubic (FCC) lattice; (b) variation of crystallite size of NiO_x thin films as a function of annealing temperature, determined from the XRD patterns using the Debye-Scherrer's relation (equation 3.1). It can be observed that the crystallite diameter increases at increasing annealing temperature.....71

Figure 3.5: (a) Current–voltage characteristics of NiO_x thin films annealed at different temperatures. (b) Schematic of planar configuration used to measure the I-V curve of NiO_x

thin films. Electrical conductivity versus annealing temperature of NiO_x thin film determined from the I-V characteristics. The conductivity is non-monotonically but peaked at 450°C.....73

Figure 3.6: Leftmost column: AFM of NiO_x (right side of the images) and ITO substrate (left side) annealed at different temperatures: (a) 300°C; (b) 400°C; and (c) 450°C. Middle column: corresponding KPFM images at (e) 300°C, (f) 400°C and (g) 450°C. Rightmost column: work function histograms obtained from the KPFM images at (h) 300°C, (i) 400°C and (j) 450°C.....74

Figure 3.7: (a) Variation of the work function of NiO_x thin films with the annealing temperature and (b) Histogram of the work function of transparent conducting thin films frequently used in optoelectronic devices, also including our NiO_x thin film annealed at 450°C. The work function of the NiO_x thin film is very close to the work function of PEDOT:PSS.....75

Figure 3.8: (a) NiO_x powder ESR spectra at room temperature from fine grains, less than 130 μm, and measured quantities from 4 mg to 10 mg; (b) zoom of “A” signal recorded from the same sample; (c) direct proportionality between the double-integrated intensity of “A” signal and the sample mass, suggesting that signal “A” comes from defects in the grain bulk; (d) NiO_x powder spectra at room temperature from coarse grains of 1.2 ± 0.2 mm diameter, exhibiting a significantly lower intensity of signal “B” over signal “A” due to lower amount of surfaces; (e) zoom of “A” signal showing comparable linewidths with panel b; and (f) signal intensity as a function of mass. Both samples were annealed at 450 °C.....77

Figure 3.9: (a) ESR signal intensity of fine-grain NiO_x powder sample as a function temperature, consisting of two observed signals A and B. Signal B becomes progressively broader, anisotropic, and surface-related at lower temperature; (b) Curie plot for the intensity of signal A, strongly suggesting that it originates from localized states; and (c) intensity of signal B as a function of inverse temperature, showing neither Curie nor Pauli paramagnetism, but becoming constant below 120°K – a temperature that we identify as

the Neel temperature below which signal B becomes constant, anisotropic, and likely confined in the proximity of the surface.....78

Figure 3.10: (a) The ESR signal intensities of signal A and signal B, (b) spin density of signal A from bulk grains and (c) spin density of signal B surface grains with different annealing temperature from (225 – 500) °C of NiO_x thin films.....81

Figure 3.11: Electrical conductivity versus spin density of (a) signal A, (b) signal B. good linear relationship exist between the electrical conductivity and spin density of signal A related localized bulk states and contrarily, no correlation was found between Signal B related extended surface state.....82

Figure 3.12: MFM phase images obtained by tapping mode AFM technique for nanostructured NiO_x thin films at three distinct annealing temperatures: (a) 300 °C scan with demagnetized tip and the corresponding (b) magnetized tip, and (c) histogram of the two scans to obtain the phase shift. (d) 400 °C scan with demagnetized tip and the correspondence (e) magnetized tip and (f) histogram of the phase profile from the two scans. (g) 450 °C scan with demagnetized tip and the corresponding (h) magnetized tip and (i) histogram of the two scans to obtain the phase shift.....85

Figure 3.13: MFM phase shift in non-stoichiometric nickel oxide thin films. The reported phase corresponds to the average peak value in Figures 3.12 c, f, and I and is plotted as a function of annealing temperature. The increase in phase shift strongly suggests that the Neel temperature transitions from above room temperature to below room temperature at annealing temperatures about 400 °C.....86

Chapter 1

A Review of Nanostructured Nickel Oxide

Nickel oxide (NiO_x) is an important transition metal oxide with face centered cubic lattice structure. It exhibits anodic electrochromism, high resistance to wear, electrochemical stability and high transparency [1]. This promising material displays antiferromagnetic behaviour up to 523 K, an unusually high Neel Temperature (T_N) for an antiferromagnet, while it is paramagnetic above T_N [2]. Non-stoichiometric and nanostructured nickel oxide exhibits a more complex magnetic behaviour: for instance, a certain degree of paramagnetism is sometimes found below T_N [3], and recent reports of dislocation-related ferromagnetism have been published [4]. Furthermore, T_N has been found to depend on the crystallite diameter and shape, and is significantly lower (down to 30 K) in nanostructured NiO_x materials and nanoparticles [1, 4-7]. In this first chapter of my thesis, I will review the literature that discusses the intriguing magnetic properties of NiO_x in relation to the fundamental physics of antiferromagnetic, ferromagnetic and paramagnetic materials. NiO_x is considered a prototypical p-type, wide band-gap (3.6–4.0 eV) semiconducting oxide, [8-9] but is peculiar in that no heteroatoms are required to “dope” it at high transparency levels, contrary to other transparent semiconducting oxides such as tin oxide (that requires In, Sb or other elements) or zinc oxide (requiring Al) [10]. Nanostructure nickel oxide thin films have been the subject of a considerable number of research studies in relation to the electrical conductivity emerging from these intriguing “self-doping” effects [7]. To introduce these phenomena, we will here discuss what is known on the electrical conductivity of NiO_x , especially for what concerns its relationship with non-stoichiometry and defects.

1.1 Transparent conducting oxides

Transparent conducting oxides (TCOs) are widely investigated thin-film materials because of their potential applications in devices, such as flat light-emitting diodes and solar cells [11, 12]. TCO materials of practical interest include CdO, aluminum-doped zinc oxide (AZO), NiO_x , and combinations of these binary compounds [13]. Historically, Indium tin oxide (ITO) has been the TCO of choice in thin-film optoelectronics. It exhibits a low sheet

resistance (R_s) and a high optical transparency in the visible photon energy range due to its wide band gap, of (3.6–4.0 eV). ITO exhibits tunable electrical conductivity, and high stability under adverse environmental conditions [14-15]. Although ITO possesses such desirable properties, there is an increasing demand to develop TCOs other than ITO due to the limited supply and high cost of indium [16]. This has also imparted negatively to the flat panel display industry, which has witnessed a progressive decrease in the use of ITO [13]. Alternative TCOs at a reduced cost are extremely important to keep the industry and other utilizers of transparent electrodes flourishing.

Among the various choices of TCOs that can serve as possible alternatives to ITO, ZnO has been sometimes considered for use as a transparent conductor in flat panel displays. However, the long-term stability of ZnO devices is problematic, because of the extreme susceptibility of this material to environmental degradation [17]. Similarly, CdO is often avoided, because of the toxicity of cadmium. NiO_x is an excellent candidate as a conducting oxide, with the potential to reach performance comparable to ITO, both in optical transparency and electrical conductivity. It is a p-type transparent conductor with wide band gap energy [8]. Because of these properties, NiO_x has a lot of application potential, especially in the fabrication of devices in which electrodes with extended transparency in the near-ultraviolet (UV), (3.2-4.0 eV) range are essential.

1.2 NiO_x and its applications

There are many applications of nickel oxide in energy devices that can be found in the literature, for instance in: electrochemical capacitors/supercapacitors [19], electrodes for batteries [20], gas sensors [7], composite anodes, and cathodes for fuel cells and solar cells [21], magnetic-based data storage devices, [22] and electrochromic coatings [23-25]. Among these applications, we are particularly interested in the use of nickel oxide thin films as a solar cell electrode. Therefore, I will focus my review to this application area.

A potential application of nickel oxide is as a cathode material for hole transport layers in polymeric bulk-heterojunction solar cells (BHJ) [26]. To minimize interfacial power losses, thin (5–80 nm) layers of NiO_x inserted between the ITO cathode and the organic active layer [e.g. poly(3-hexylthiophene) (P3HT) mixed with 6,6-phenyl-C₆₁-butyric acid

methyl ester (PCBM)] [26]. One way to enhance the performance of BHJ solar cells is to suppress the power losses to the greatest extent possible. An effective electron blocking layer (EBL), or hole-transporting layer (HTL), achieves this goal by preventing current leakage towards the cathode, which leads to enhanced diode rectification properties [27]. It has been suggested that a material to serve as an interfacial HTL/EBL in BHJ solar cells should possess the following properties [27]:

- (i) sufficient optical transparency to allow a photon or photons to access the active layer, which requires wide band-gap semiconductors ($E_g > 3$ eV) transparent in the visible spectral region;
- (ii) effective blocking of electron leakages towards the cathode, while efficiently transporting holes to such electrode;
- (iii) appropriate energy-level alignment with respect to the valence and conduction band of the semiconducting active layer, in order to allow ohmic contact to the electron-donating material; and
- (iv) good chemical stability.

Figure 1.1 shows the architecture and band diagram of a typical BHJ solar cell incorporating a hole transport layer for enhanced device performance. In BHJ solar cells, [26] a strongly correlated electron-hole pair (a.k.a. exciton) is formed upon light absorption in an electron-donating, p-type, organic material. As strongly-correlated excitons have very short diffusion length (~ 5 nm [27]) the p-type and n-type organic materials need to be mixed at the nanoscale to ensure a sufficient electron-hole dissociation rate. This also means that a significant parasitic current of electrons may leak to the ITO cathode, if not prevented to do so by an electron-blocking layer. Therefore, although HTL/EBL are frequently used in many type of thin-film solar cells, they are particularly important in organic BHJ photovoltaics, and NiO_x has been proposed for this application, even though further enhancement of its properties, towards best structure-performance optimization, is required.

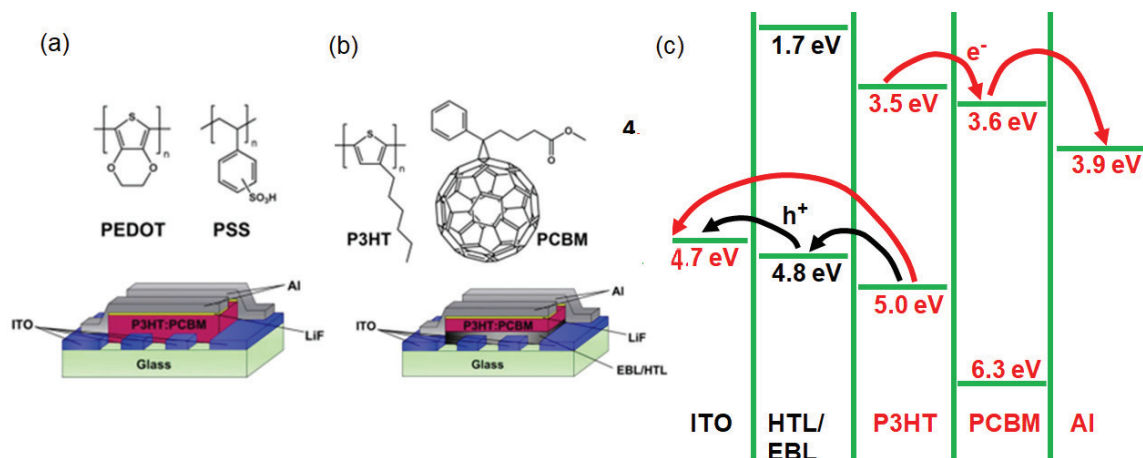


Figure 1.1: Schematic drawings of the bulk-heterojunction photovoltaic device structures used here without (a) and with (b) an interfacial electron-blocking layer/hole-transporting layer (EBL/HTL). The chemical structures of PEDOT:PSS and the active layer components P3HT and PCBM are also shown. (c) Energy level diagram of device components referenced to the vacuum level. The published valence and conduction band energies NiO_x as HTL/EBL are shown. [26]. Reprinted by permission from the National Academy of Sciences. Copyright (2007).

Normally, in order to prevent electron leakage to the cathode, to aid in photo-generated hole extraction, and to planarize the ITO surface, a thin semiconductor layer of poly(3,4-ethylenedioxythiophene):poly(styrene-sulfonate) (PEDOT:PSS) is used as a HTL/EBL in BHJ solar cells. However, its acidity, tendency to absorb water, and inability to block electrons efficiently are all factors that contribute to the degradation of devices incorporating PEDOT:PSS [28]. Devices incorporating NiO_x as an HTL/EBL are more stable in air than devices using PEDOT:PSS.

There are several additional applications of nickel oxide nanoparticles, apart from potential applications in solar cells and as a replacement of ITO transparent electrodes. NiO_x thin films are used in magnetic data-storage technology. This use of nickel oxide is enabled by its antiferromagnetism that persists at very high temperatures [29]. To fully understand this phenomenon, we will review the fundamentals of magnetism in materials.

1.3 Magnetic properties of Materials

Magnetism is a response of materials to an external magnetic field. The magnetic moment of an atom has three principal sources: the spin with which electrons are endowed, their orbital angular momentum, and the change in orbital moment induced by an external magnetic field. Atoms with all filled electron shells have zero net spin and zero net orbital moment [30]. The magnetization \mathbf{M} represents the net sum of magnetic moments per unit volume of material. It is directly proportional to the magnetization field \mathbf{H} , so that

$$\mathbf{M} = \chi \mathbf{H}, \quad (1.1)$$

provided that the field is not too strong. For sufficiently small \mathbf{H} , the relationship between \mathbf{H} and the external magnetic field \mathbf{B} is linear, and

$$\mathbf{H} = \mathbf{B} / \mu, \quad (1.2)$$

where μ is the magnetic permeability of the material. Equation (1.2) implies that the material is isotropic and responds in the same way to external magnetic fields applied along different directions. In vacuum, the magnetization field is defined as

$$\mathbf{H} = \mathbf{B} / \mu_0. \quad (1.3)$$

Therefore, in vacuum, where there is no matter to magnetize, the magnetic susceptibility χ vanishes, and the permeability is μ_0 . That's why μ_0 is called permeability of the free space, $\mu_0 = 4\pi \times 10^{-7} \text{ H m}^{-1}$. Substituting equation (1.3) in equation (1.1), we thus obtain that

$$\mathbf{M} = \chi \mathbf{B} / \mu_0. \quad (1.4)$$

The magnetic susceptibility χ is a dimensionless quantity that varies from one substance to another. If it is positive, the substance is a paramagnet while the substance is a diamagnet if χ is negative. In order to better understand this concept, we need to discuss the origin of diamagnetism and paramagnetism at a microscopic level.

1.3.1 Diamagnetism

Diamagnetic materials are also known as nonmagnetic. However, even in these nonmagnetic materials, the density of magnetic field lines is always smaller than in vacuum due to Larmor precession of pairs of electrons of opposite magnetic moments [31]. This effect is demonstrated in Figure 1.2. In the absence of an external magnetic field, the motion of electrons of opposite spins, one moving in clockwise direction and the other one

moving counterclockwise, produces a zero-net current. The electron orbital motion is affected by the presence of a magnetic field, however. If an external magnetic field is applied to a conducting coil, or loop, an electrical current will flow through such loop, and will create a magnetic dipole moment opposite to the applied field. Due to this field, there will be a precession of the angular velocity of the electron, which for small enough \mathbf{B} , can be written as

$$\text{Precessional angular frequency, } \boldsymbol{\omega} = e\mathbf{B}/2m, \quad (1.5)$$

where e and m are, respectively, the electron charge and mass. If the applied field is slowly varying over time, the motion in the rotating reference frame will be the same as the original motion in the system at rest in the absence of external field. The fact that electrons of opposite spin undergo a change in angular frequency in the same direction due to precession, will cause a net current in the double coil that represents the classical equivalent of their orbits. Therefore, the current due to precession of Z electrons in an element of atomic number Z will be given by

$$I = \frac{-Ze\omega}{2\pi} = \frac{-Ze^2B}{4\pi m} \quad (1.6)$$

The magnetic moment m of a conducting loop of radius R is given by the product of the current, expressed by equation (1.6) and the area ($A = \pi R^2$) inside the coil, so we obtain

$$m = I \langle A \rangle = -\frac{Ze^2B}{4m} \langle R^2 \rangle, \quad (1.7)$$

where $\langle A \rangle = A \langle \cos \theta \rangle$, and brackets $\langle \dots \rangle$ indicate the averaging of values of A , R and $\cos \theta$ over all the possible orientations of magnetic field between $\theta = 0$ and $\theta = 180^\circ$. Equation (1.7) determines the magnetic moment of a single atom. There are N magnetic moments in a solid with N atoms per unit volume, for a total magnetization $M = Nm$. Therefore, by replacing M calculated via equation (1.7) into equation (1.4), the magnetic susceptibility can be calculated:

$$\chi = \frac{\mu_o M}{B} = -\frac{\mu_o NZe^2}{4m} \langle R^2 \rangle. \quad (1.8)$$

This classical result indicates that the calculation of the susceptibility of a diamagnetic system is reduced to the calculation of $\langle R^2 \rangle$ for electrons localized about a given atomic nucleus [32]. In summary, diamagnets produce their own magnetic moment opposite to the direction of an applied external magnetic field. Magnetic field lines of an external magnetic field are weakly expelled by a diamagnet. In addition, equation (1.8) shows that the higher the atomic number of a diamagnetic element, the higher the effect on the magnetic susceptibility. This demonstrates why metals of heavy elements (e.g. gold or bismuth) are often diamagnetic even though metals also exhibit paramagnetism, another form of magnetic behaviour which is due to electrons with unpaired spins.

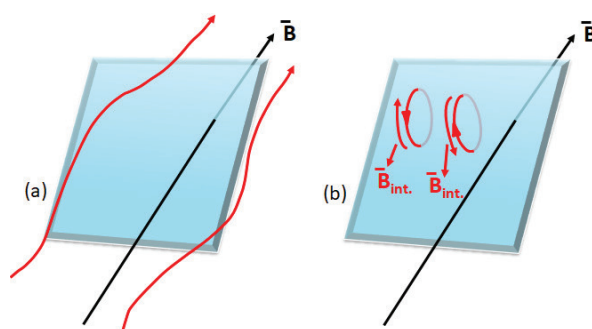


Figure 1.2: (a) Schematic illustration of diamagnetism showing the decrease in concentration of magnetic field lines, and (b) diamagnetism due to internal dipolar magnetic field caused by magnetic dipoles induced by Larmor precession in a system of opposite spins.

1.3.2 Paramagnetism

Paramagnetic systems are usually formed by atoms, molecules and radicals with odd number of electrons, in which unpaired electron spins represent an inherent source of paramagnetic centers. Metals also exhibit paramagnetism, because free electrons at energies $E \approx \pm k_B T$ in the proximity of Fermi level are unpaired at nonzero absolute temperature T . Magnetic moments of unpaired electrons are randomly oriented which leads to zero magnetization in the absence of an external field (Figure 1.3, panel a) and a

preferential orientation of the unpaired spins parallel to the magnetic field when such field exists (Figure 1.3, panel b) [33]. This preferential orientation is contrasted by the disordering effect of temperature. Therefore, in many paramagnets, the susceptibility is inversely proportional to the temperature, which is known as the Curie's Law (see Figure 1.4):

$$\chi = \frac{C}{T}, \quad (1.9)$$

where C , the Curie constant, can be shown to be proportional to n_s , the concentration of paramagnetic centers in the system [34] according to

$$C = n \mu^2 n_s / k_B. \quad (1.10)$$

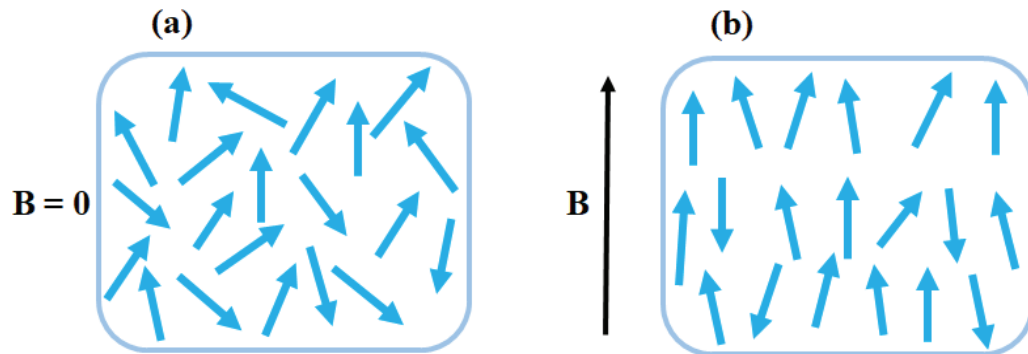


Figure 1.3: (a) Random orientation of unpaired spins in the absence of an external magnetic field and $B = 0$; and (b) preferential orientation of unpaired spins and magnetic moments in a direction parallel or antiparallel to the magnetic field at $B \neq 0$. The difference between parallel and antiparallel spin populations is approximately inversely proportional to the temperature of the system, which leads to Curie's Law.

Equation (1.9) assumes that n_s is temperature independent. This is normally true for localized paramagnetic centers in the absence of temperature-induced structural changes in a solid (such as, for instance, chemical reactions, phase transitions, defect annealing, site ionization, etc.). However, n_s is not constant over temperature in the presence of itinerant electrons in metals, doped semiconductors and, in general, in systems where free electrons are present.

At zero absolute temperature, free electrons in metals are all paired and each occupied electronic state is filled by two electrons at opposite spin number $\pm 1/2$, while all electronic states at energies larger than the Fermi level are unoccupied. This is a consequence of the Fermi-Dirac statistical distribution, obeyed by free electrons, which is a step function at $T = 0$. At nonzero temperature, and for small energy differences from the Fermi energy, the Fermi-Dirac distribution assumes the form

$$f(E) = 1 / [1 + \exp(E/k_B T)]. \quad (1.11)$$

According to equation (1.11), unpaired electrons, corresponding to singly occupied free-electron energy levels, occupy a shell of thickness $\approx k_B T$ about the Fermi surface, whereas the area of the Fermi surface is G_F , the electron density of states at the Fermi level. The density of unpaired electrons is $n_s \approx G_F k_B T$, which is proportional to temperature. By replacing this expression into equations (1.9) and (1.10), we thus obtain

$$\chi \approx \mu_B^2 G_F. \quad (1.12)$$

We can conclude that, in metals, and paramagnetic systems dominated by extended states and free electron states in general, the magnetic susceptibility is independent of temperature. This will offer us a tool to distinguish between extended-state paramagnetism and localized-state paramagnetism in nickel oxide and other solid systems.

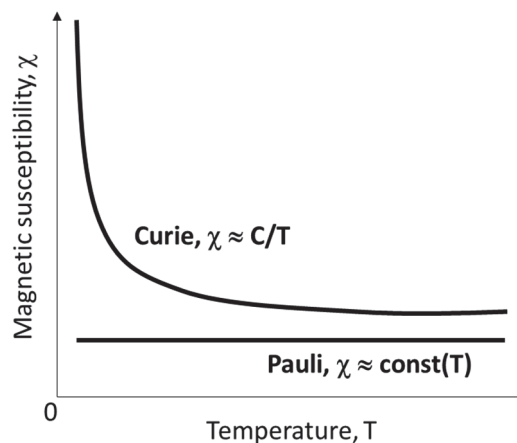


Figure 1.4: Different temperature behaviour of the susceptibility in paramagnetic systems dominated by localized states (Curie's Law, eqn. 1.10) and extended states (Pauli paramagnetism, eqn. 1.12).

1.3.3 Ferromagnetism

A ferromagnet has a spontaneous and permanent magnetic moment even at zero applied magnetic field [32]. The existence of spontaneous magnetism indicates that electron spins and magnetic moments are arranged in a regular fashion due to self-consistent and collective effects: [32] each spin is aligned by the local internal magnetic field produced by the nearest neighbor sites. When a ferromagnetic material is placed in an external magnetic field, the moments of spontaneously aligned magnetic domains align along the direction of the field, and they form a large net magnetic moment as demonstrated in Figure 1.5a. Ferromagnets behave similarly to paramagnets in the sense that their susceptibility is positive, even though, normally, it is significantly higher [35]. Examples of ferromagnetic elements at room temperature are the three-familiar transition-metal ferromagnets: iron, nickel and colbalt.

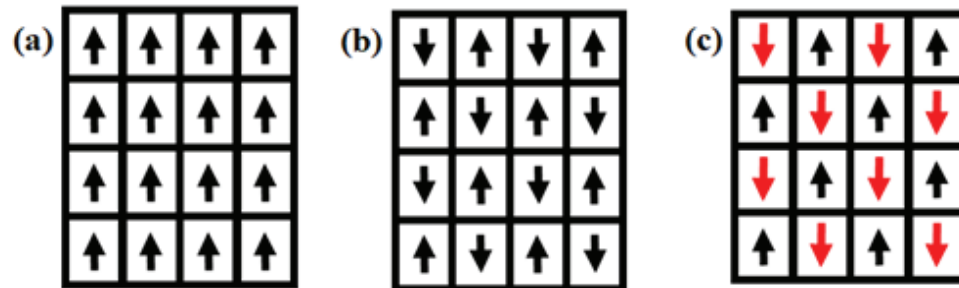


Figure 1.5: Three different types of magnetic spin ordering in (a) ferromagnetism with exchange integral $J > 0$; (b) antiferromagnetism with exchange integral $J < 0$; and (c) ferrimagnetism, in which different sublattices have opposite net magnetic moments, with a nearly zero total magnetic moment of the two sublattices.

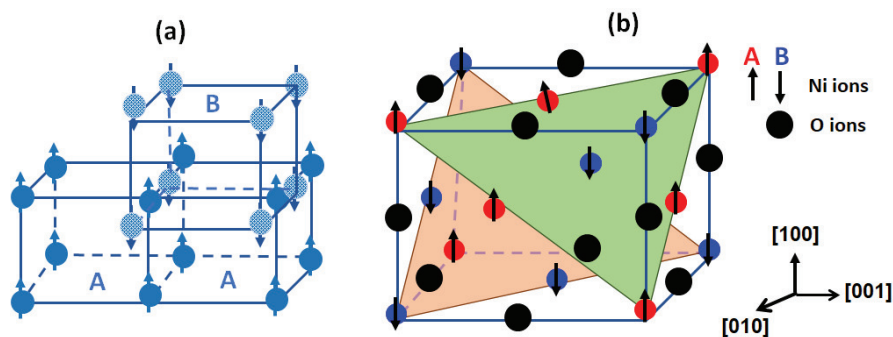


Figure 1.6: Structure of NiO showing antiferromagnetic spin structure: (a) two sublattices of Ni ions and (b) two FCC sublattices of opposite spins with diatomic base. In NiO, oxygen ions have no net magnetic moments and the spin moments of Ni^{2+} ions are aligned anti parallel to each other in adjacent atoms. The Miller indices notation of planes signifies ferromagnetic surfaces as indicated in the structure and only one sublattice faces the plane.

1.3.4 Antiferromagnetism

In addition to ionic solids and oxides, antiferromagnets include certain metals and alloys, normally with a diatomic base. Nickel oxide, the solid that is the subject of our thesis, is antiferromagnetic. In these systems, the net magnetic moment of a sub-lattice oriented parallel to the external magnetic field is cancelled out by the net magnetic moment of another sublattice aligned in the opposite direction. Like in ferromagnets, each spin is aligned by the local magnetic field produced by the nearest neighbor sites and, therefore, antiferromagnetism persists even in the absence of external field. This implies that an antiferromagnetic phase has zero net moment [32] as demonstrated in Figure 1.5b and 1.6. Basically this has to deal with the fact that exchange interaction is importantly affected by the lattice spacing, and there is only a very small range of separation between paramagnetic ions for which J_{ij} is positive and energy is at a minimum when spins are all parallel. Otherwise $J_{ij} < 0$ and spins tend to arrange in an antiparallel way. In other words, an antiferromagnet can be envisaged as to be formed by two interpenetrating sublattices of the same type as in the pristine lattice, but with double-length lattice vectors, each of the two sublattices having its ions with their spins parallel, but with the spins on one lattice being opposite as those on the other lattice.

As such, the information stored in antiferromagnetic moments would be invisible to common magnetic probes, insensitive to disturbing magnetic fields. The antiferromagnetic

element would not magnetically affect its neighbors, regardless of how densely the elements are arranged in the device [36]. For this reason, antiferromagnetic materials find their use as spacers in the data-recording industry. An intermediate situation between antiferromagnets and ferromagnets is represented by ferrimagnets (Figure 1.5c), where the two sublattices are slightly different, the total magnetic moment is not exactly zero, and a limited magnetization persists even in the absence of external field. A similar situation also occurs in disordered antiferromagnets. When an antiferromagnetic crystal is nanostructured or amorphized, the antiferromagnetic phase is locally perturbed. In my thesis, the understanding of nanostructured nickel oxide will be essential to investigate the different magnetic properties caused by crystal size variation, surface effects, and intrinsic point defects and impurities.

1.4 Theory of magnetism

The origin of diamagnetism in materials is due to orbital angular momentum of bound electron of opposite spins, while the origin of paramagnetism is related to unpaired spins and the magnetic properties of materials are, to a large degree, determined by the interactions between them. Such spin-spin interactions also control the phase transitions between paramagnetic and ferromagnetic, (or antiferromagnetic, or ferrimagnetic) states of matter. The relevant interaction in these cases is the exchange interaction, which can be generally described by the Heisenberg Hamiltonian [37];

$$H = -\sum_{ij} J_{ij} S_i S_j \quad (1.13)$$

where the sum is over all spins in the system, S_i and S_j , and J_{ij} is the exchange constant between sites (i) and (j) or atomic spins (i) and (j). The exchange interaction has a very short range, [38] and therefore, the sum is often limited to nearest neighbor sites. When J_{ij} is positive, parallel spin alignment is favored, which leads to ferromagnetic (FM) ordering and a large net magnetic moment. When J_{ij} is negative, antiparallel orientation is favored, the net magnetic moment is zero, and the solid is antiferromagnetic (antiFM). At sufficiently high temperature, the exchange energy in eq. (1.13) is smaller in magnitude than the thermal energy and FM and antiFM systems undergo a phase transition at a certain

critical temperature at which that happens. Spins will be randomly aligned above such temperature, and the system will be in a paramagnetic phase. When the temperature is lower than the critical temperature, the thermal energy is too small to allow for incoherent motion of individual spins, and it becomes favourable for the system to order magnetically [39]. Specifically, the critical transition temperature between paramagnetic and antiFM phases in systems at $J_{ij} < 0$ is known as the Neel temperature, and will play an important role in our work.

1.5 Neel temperature

The Neel temperature is named after Louis Neel, a French physicist, who in 1936 offered one of the first explanations of antiferromagnetism [40]. Different Neel temperature are characteristic of each antiFM material [41]. The Neel temperature presents significant analogies with the Curie temperature of ferromagnets, the temperature above which spontaneous magnetization vanishes. The Neel temperature separates the disordered paramagnetic phase at $T > T_C$ from the ordered ferromagnetic phase at $T < T_C$. Transition between antiFM and paramagnetic states are significantly different from first-order transitions between solids and liquids, or between liquids and vapors which involve a constant temperature. Transitions between magnetically ordered and disordered spin phases are the second-order type [38] and occur continuously. In this way, the two phases do not coexist with each other under quasistatic equilibrium conditions. The system will undergo a decrease of the ordered parameter with a continuous and significant decrease of the size of the magnetically ordered domains up to the Neel temperature (T_N). T_N in bulk NiO is 523 K and has the highest value among all antiferromagnetic transitions in metal monoxides that possess a cubic lattice structure [42].

Table 1.1 Antiferromagnetic crystals

Substance	Crystalline structure	Transition temperature, T_N , in K
MnO	FCC	116
MnS	FCC	160
CoO	FCC	291
FeO	FCC	198
NiO	FCC	523

Some crystalline antiferromagnetic materials have relatively high Neel temperatures, well above room temperature, but never as high as in nickel oxide. Additionally, the Neel temperatures of nickel oxide nanoparticles, nanostructured nickel oxide, and nickel oxide thin films are affected by varying the particle size, growth morphology, lattice distortions, and defect type and density. These effects will be discussed more extensively in the next section.

1.6 Effect of Nanostructuring on Neel temperature of NiO_x

In this section, I will review the effect of nanostructured morphologies on the Neel temperature of nickel oxide as this is critical for this thesis. The magnetic properties of NiO_x nanoparticles are very sensitive to size, crystallinity, and morphology. By varying the particle size, one can obtain interesting magnetic properties continuously tunable from localized to bulk-like behavior [43-44]. Duan *et al.* [45] reported about NiO_x nanoparticles with particle diameters of 3.5-12.4 nm, synthesized by the thermal decomposition of nickel acetate at different temperatures in NaCl and Li₂CO₃ salts. Their results showed an increase in saturation magnetization, and remnant magnetization at decreasing nanoparticle size [45]. Magnetization measurements reported by Tadic *et al.* revealed that NiO nanoparticles with a 5-nm size prepared by sol-gel combustion synthesis, are antiferromagnetic with a Neel temperature as low as 56 K [4]. This is much smaller than the reported value for bulk NiO_x, as seen in Table 1.1. Their work shows that T_N is diminished by small particle size, presence of extended and point defects and low crystallinity of the particles defect and crystallinity of the particles.

Grain diameter, morphology and degree of crystallinity have a strong influence on magnetic interactions in nanostructured nickel oxide [46]. Rinaldi *et al.*, reported nickel oxide nanoparticles obtained from the pyrolysis of Ni nitrate in a porous carbon matrix with average particle diameters in the range of 2-5nm. Their results indicate that ordering is maximally affected in a system of reduced dimensionality [47], with Neel temperatures not dissimilar from reference [46] at comparable diameters. A summary of literature report on the Neel temperature of NiO nanoparticles is shown in Table 1.2, which shows that very often, similar particle diameters result in different values of T_N. This may suggest that other

factors of influence (e.g. defects, lattice imperfections, impurities, shape, etc.) play an important role in determining T_N , which requires additional investigations.

Table 1.2: Review of Neel temperature, a transition-ordering temperature for different nanoscale NiO_x systems

Sample	Particle size	T_N	Deposition	Ref.
NiO nanoparticle	4 nm	461 K	Pyrolysis	[1,44]
NiO nanoparticle	6 nm	497 K	Pyrolysis	[1,42]
NiO nanoparticle	7 nm	513 K	Pyrolysis	[1,42]
NiO nanoparticle	20 nm	480 K	Oxidization/Reduction	[7,]
NiO nanoparticle	16 nm	30 K	Precipitation	[5]
nanostructured NiO	5 nm	56 K	Sol-gel	[4,44]
NiO nanoparticle	100 nm	123 K	Solution growth	This work
NiO nanoparticle	20 nm	470 K	Thermal decomposition	[6]
nanostructured NiO	10 nm	430 K	Thermal decomposition	[6,42]
Bulk NiO	n/a	523 K	--	[2]

1.7 Ferromagnetic surfaces in NiO_x

Nanostructured antiFM nickel oxide may have induced ferromagnetic ordering (FM) surfaces due to size effect, shape and point defects. The FM ordering is observed when a magnet is brought into proximity with the material in which the antiparallel spins domain

in the material tend to align parallel to the direction of the applied external field [44]. This is achieved by employing magnetic force microscopy measurement for which results will be discussed in detail in Chapter 3 of this thesis. Consequently, the existing FM surfaces in transition metal-doped semiconducting oxides remains unclear, however, Sundaresan et al. [7] have attributed it to intrinsic defects.

There are a few reports on the paramagnetic/ferromagnetic behaviour of nanostructured NiO samples in the literature, and different models have been proposed to account for their magnetic responses. Magnetism is attributed to unpaired spin owing to the presence of higher oxidation state (Ni^{3+}) ions in nanostructured NiO_x materials proposed to be responsible for the observed magnetic moment [48]. Meanwhile Ni^{2+} ion vacancies or/and oxygen interstitials are suggested to be accountable for the observed magnetic properties in NiO nanoparticles [49]. This finding was confirmed by temperature-dependent zero-field magnetization studies between the range of 20-300 K for NiO_x nanoparticles reported by Madhu et al [49]. In their work, they stated the presence of weak FM interactions over antiFM interactions demonstrated with a core-shell model. Nevertheless, the origin of ferromagnetic interactions is found to be associated with the presence and concentration of oxygen vacancies at the core being antiferromagnetic surfaces as an impurity donor that enhances the orientation of magnetic moments associated with Ni^{2+} ion vacancies at the shell [49]. This is critical because defect induce ferromagnetic surfaces along with antiferromagnetic interactions residing at the surface of non-stoichiometric NiO thin film, which contributes immensely to its electrical transport mechanism.

1.8 Electrical transport in solids and in NiO_x

In this section, I present the charge carrier transport in ordered and disordered materials, in which it normally occurs, respectively, by extended states and by localized states [50]. Localized states can act as traps, by limiting the carrier mobility during charge transport by extended states. However, they can promote electrical transport if they act as dopants in an extended-state system. They may also lead to localized-state transport processes, by tunneling, or in the hopping regime where the carriers move site-to-site between localized

states via thermally activated phenomena. Accordingly, we shall explain the different charge transport mechanisms in solids, especially as they apply to nickel oxide systems.

1.8.1 Extended-state transport in metals / intrinsic semiconductors

Ordered crystalline semiconductors are known to exhibit ideal periodicity at long range. A reciprocal lattice can always be defined from them, by a Fourier transformation of the real lattice. In the reciprocal lattice description of a solid, the electron crystal momenta, $\hbar\mathbf{k}$, act as independent coordinates in lieu of the spatial coordinates \mathbf{r} of the real lattice. According to Bloch's theorem [50], the diffusion of electrons in a long-range ordered crystal can be described in terms of combinations of plane waves at any wavenumber \mathbf{k} within the first Brillouin zone, the unit cell of the reciprocal lattice. Therefore, the crystal momentum is a "good" quantum number for these solids, and is directly related to the energy eigenvalues, $\varepsilon_j(\mathbf{k})$, associated with the electron wavefunctions. Plane waves correspond to states extended everywhere within the crystal, which may lead to excellent charge transport properties. However, fully occupied or fully unoccupied bands do not contain holes or electrons, with the capability to diffuse under an external electric field. Materials with entirely full valence band, $\varepsilon_v(\mathbf{k})$, and entirely empty conduction band, $\varepsilon_c(\mathbf{k})$, are expected to be insulators at zero absolute temperature. Accordingly, low-temperature electrical conductivity by extended states only occurs through bands that are partially empty or partially filled [51]. Materials with half-full (or half-empty) bands are known as metals.

Crystals are either metals or perfect insulators at zero absolute temperature. However, at finite temperature, a nonzero thermal energy, $k_B T$, may allow electrons to transition from the valence band to the conduction band in crystals with sufficiently small energy band gap. The band gap is given by

$$E_g = \varepsilon_c(\mathbf{k}_{\min}) - \varepsilon_v(\mathbf{k}_{\max}) \quad (1.14)$$

where \mathbf{k}_{\min} and \mathbf{k}_{\max} represent the reciprocal lattice wavevectors corresponding to the conduction band minimum and the valence band maximum, respectively. If $\mathbf{k}_{\min} = \mathbf{k}_{\max}$, the material is called a direct-band gap semiconductor, while the band gap is indirect for $\mathbf{k}_{\min} \neq \mathbf{k}_{\max}$. Specifically, crystalline NiO is an indirect band-gap semiconductor with $\mathbf{k}_{\min} =$

$\mathbf{0}$, but \mathbf{k}_{\max} corresponds to a point very close to the zone-center of the first Brillouin zone of the reciprocal lattice, to the point that the indirect nature of NiO can only be observed by sophisticated computer simulations, as shown Figure 1.7a. [52]

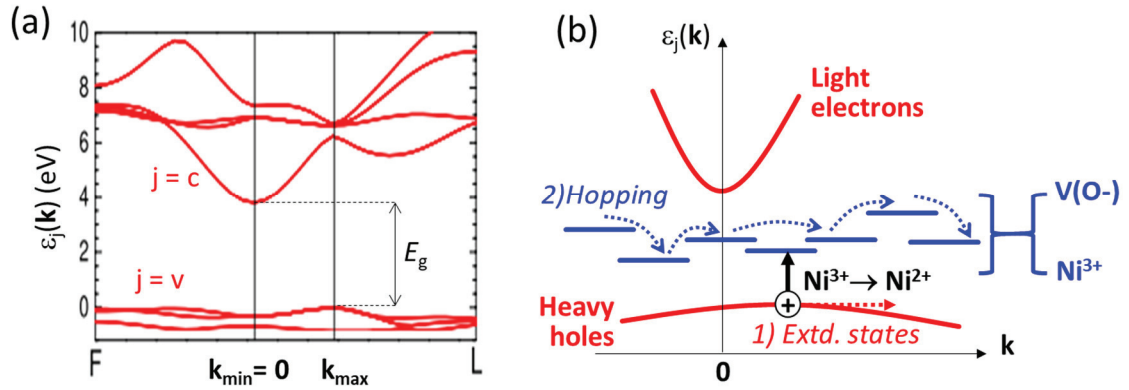


Figure 1.7 (a) Electronic band structure of NiO showing a light-electron conduction band and heavy-hole valence band and indirect gap [52] (adapted by permission from Institute of Physics Publishing Ltd National Academy of Sciences. Copyright 2013); and (b) simplified band diagram with gap-state defects in NiO_x with possible p-type transport mechanisms by extended states and hopping. Although extended states are a more likely transport process in semiconductors, the heavy-hole, low-mobility valence band of NiO_x suggests hopping as another plausible conductivity mechanism.

The concentration of electrons in the conduction band, and holes left behind in the valence band, will be given by the Fermi-Dirac statistics:

$$f(E_g) = \frac{1}{1 + \exp(E_g / k_B T)} \approx \exp\left(-\frac{E_g}{k_B T}\right), \quad (1.15)$$

where the second equality is a consequence of the fact that, normally, $E_g \gg k_B T$ (just consider that $E_g > 3$ eV in TCOs and $k_B T \approx 0.025$ eV at room temperature, which suggests that less than one electron over 40,000 transitions to the conduction band under these conditions). Equation (1.15) shows that extended-state transport in semiconductors and nickel oxide is a thermally activated process, with the band-gap functioning as an activation energy. Because activation energy is very high, transport properties of intrinsic

semiconductors are relatively poor, but they can be dramatically improved through the addition of impurities or, in the case of NiO_x , defects.

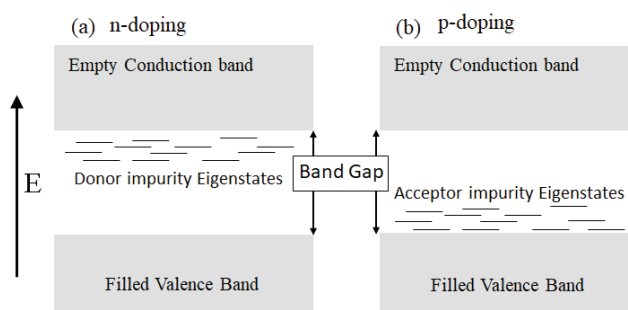


Figure 1.8: Energy diagram of doped semiconductors (a) with donor impurities and (b) acceptor impurities. With increasing temperature, electrons can be excited into the conduction band from donor states, and holes can be excited into the valence band from acceptor states.

1.8.2 Extended-state transport in doped semiconductors

In semiconductors, extended-state transport may be dramatically enhanced by doping. Impurities are intentionally added to control the type and concentration of charge carriers in doped semiconductors. An intrinsic semiconductor material presents an ideal crystalline lattice with zero impurity concentration, and the number of holes and electrons is equal. Semiconductors in which the electrical conductivity is strongly affected by the presence of impurities are known as extrinsic [53]. The concentration of dopant atoms that must be added to an intrinsic semiconductor varies by its level of conductivity [54]. Specifically, the dopant concentration that must be added to attain significant effects on the conductivity of TCOs is significantly higher than in well-known semiconducting materials, such as silicon and germanium. [55]. Furthermore, in the case of NiO_x an additional peculiarity is presented by the fact that dopants are non-stoichiometric defects, not heteroatoms. Therefore, the theory of doping valid for Si, Ge, and other tetrahedral semiconductors, may not necessarily be valid for TCOs in general and NiO_x in particular.

The energy diagrams of semiconductors with donor and acceptor impurity levels are shown in Figure 1.8a and 1.8b, respectively. For example, if a phosphorous atom with one excess valence electron is added to the tetrahedral silicon lattice, one electron will remain unbound. The phosphorous-related impurity level is very close to the conduction band of silicon and a small activation energy is sufficient to promote it. In this way, the activation energy in equation (1.15) is only a few meV, and is significantly lower than E_g . Consequently, the electron concentration in this n-type doped material is dramatically enhanced with respect to the hole concentration, with important effects on the electrical conductivity.

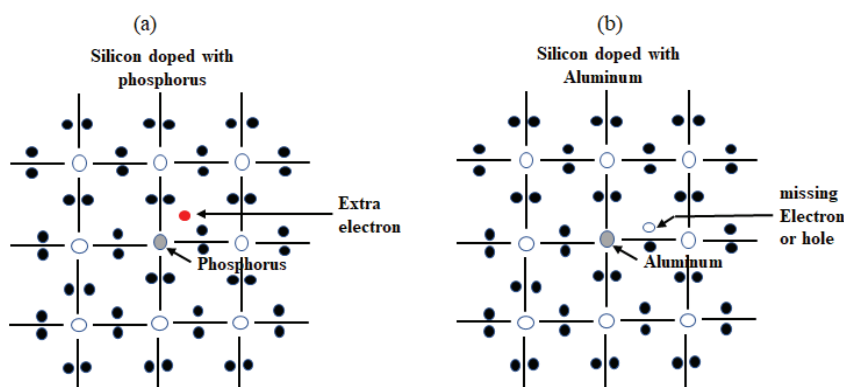


Figure 1.9: Schematic diagram of doped semiconductors: (a) silicon doped with phosphorus adds one electron that diffuses in the conduction band upon thermal activation; (b) silicon doped with aluminum produces one hole that diffuses in the valence band.

The electrical conductivity of silicon also increases when we consider adding aluminum. In this case, the dopant provides one fewer electron than silicon, so there will be one electron missing from the valence band with the production of a hole. Consequently, aluminum is known as an electron acceptor, or p-type dopant [53]. At moderate doping levels, dopant atoms create localized states that can donate electrons or holes by thermal activation, as demonstrated in Figure 1.9.

The situation is more complicated in NiO_x , however. The two bands, valence and conduction, do not have the same shape, as seen in Figure 1.7. The valence band is significantly flatter, which indicates that holes have a significantly higher effective mass

and lower mobility than electrons [39]. However, most of the impurities in TCOs tend to produce localized states with energy levels sitting in the proximity of the valence band, not the conduction band. NiO_x defects that may possibly produce such impurity levels include Ni³⁺ centers and single-negatively charged oxygen vacancies [V(O⁻)] as shown in Figure 1.7b and discussed in detail in Chapter 3 [1]. Reduction of Ni³⁺ centers into Ni²⁺ is possible, with the production of a valence-band hole. Likewise, low thermal activation energy may also lead to the reduction of V(O⁻) into O²⁻. Nevertheless, the low conduction-band hole mobility may also suggest considering alternative processes, in which defect-related localized states directly affect the charge transport mechanisms.

1.8.3 Localized-state transport by hopping

Charge transfer between localized states can play a key role in charge transport processes in both ordered and disordered systems [51]. Electron transport via extended states dominates the electrical conductivity in semiconductors at high enough temperatures above the mobility edge, at which significance fraction of charge carriers fill the conduction band. However, with decreasing temperature, the concentration of conduction electrons, given by equation (1.15), decreases exponentially. Accordingly, hopping of electrons, between localized states at the edges of the valence or conduction band, or through gap states, takes place in disordered systems even below room temperature. In order words, electrons and holes can hop from one lattice atom to another regardless of the existence, or not, of a long-range crystalline structure.

The tunneling transition probability of an electron from a localized state i to another localized state j that is lower in energy depends on the distance r_{ij} between the sites in which states i and j are localized [51]:

$$v_{ij} = v_o \exp\left(\frac{-2r_{ij}}{\alpha}\right), \quad (1.16)$$

where α , is the order range parameter, which is customarily assumed to be comparable for sites i and j . This parameter determines the exponential decay of the electron wave function of localized states, as shown in Figure 1.10. The pre-exponential factor v_o in equation

(1.16) depends on the specific tunneling or hopping process that causes electrical transport. Many processes have been proposed, [51] but their detailed discussion is beyond the scope of this work.

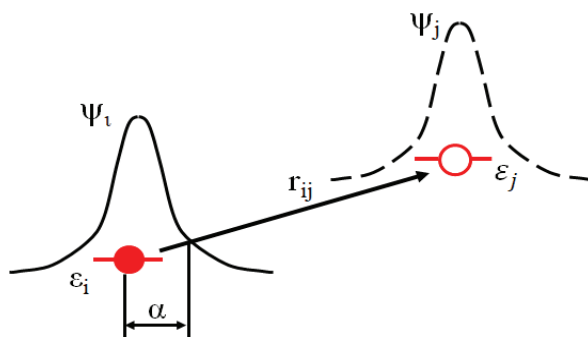


Figure 1.10: Hopping transition between two localized states i and j with energies ε_i and ε_j , respectively. The solid and dashed lines show the carrier wave functions on sites i and j , respectively.

Charge transport by localized states may be considered an option in disordered and nanostructured materials such as NiO_x thin films, because point defects (e.g. Ni^{3+} ion, O^{2-} vacancies) are randomly localized at lattice sites that produce gap-states and energy levels just above the valence band, as shown in Figure 1.7b. If that is the case in p-type NiO_x , electrons will hop from defect to defect, and defect engineering will be essential to enhance the electrical conductivity in nanostructured NiO_x .

1.8.4 The role of defects in hopping processes

Defects are any group of sites in a crystal where the macroscopic arrangement of ions differs from perfect, long-range, periodicity. In this section, various defects that can be found in crystalline solids, with a focus on the types observed in non-stoichiometric nickel oxide are presented. As shown in Figure 1.11, defects can be classified by their dimensionality: (i) zero-dimensional defects, for example vacancies, interstitials, their combinations, and substitutional defects, which all break the periodicity only at individual sites of a crystal; (ii) one-dimensional defects, which are line defects, edge dislocations and screw dislocations, and can sometimes be defined as 1D periodic structures of different periodicity from the host crystal; (iii) two-dimensional defects that may include stacking

faults along the base of layered solids, the surfaces of a finite-size crystals, and the grain boundaries along which different crystalline orientations are joined together [56]; and (iv) three-dimensional defects that affect the crystal periodicity over a medium-range volume, and include voids, clusters, and precipitates, which are small volumes of different crystalline structures. Defects may occur either under thermodynamic equilibrium, due to increase in entropy of the crystal, or they may be formed from external causes and out-of-equilibrium. For example, point defects may form due to the addition of impurities and are then known as extrinsic point defects.

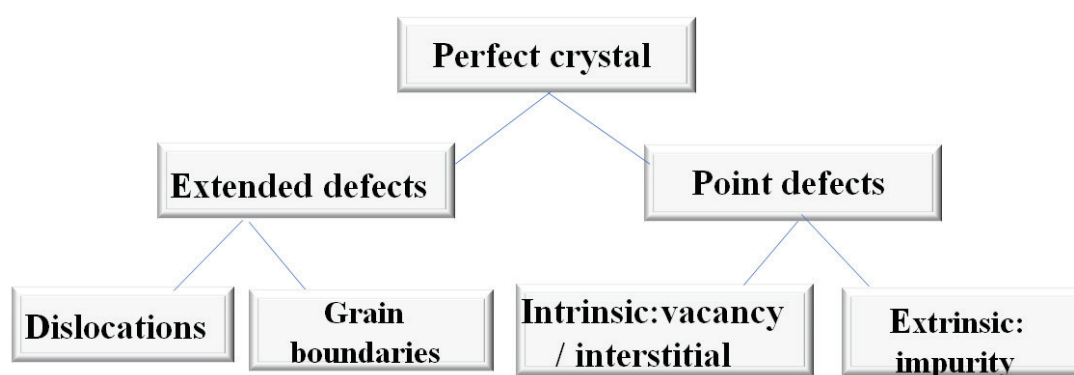


Figure 1.11: Diagram classifying defects in crystalline solids.

Vacancies: These are point defects that involve the absence of an atom from an atomic lattice site. At any finite temperature, some of the lattice points normally occupied by metal ions are not occupied by an ion in the perfect crystal, thus giving rise to vacancy defects [57]. Crystals may, or may not, rearrange to accommodate a vacancy, and vacancies may possess a different valence number from the surrounding medium and act as paramagnetic centers in a non-paramagnetic solid. Examples are singly charged vacancies $[V(O^{\cdot})]$ in NiO_x , in which oxygen sites are normally doubly-charged.

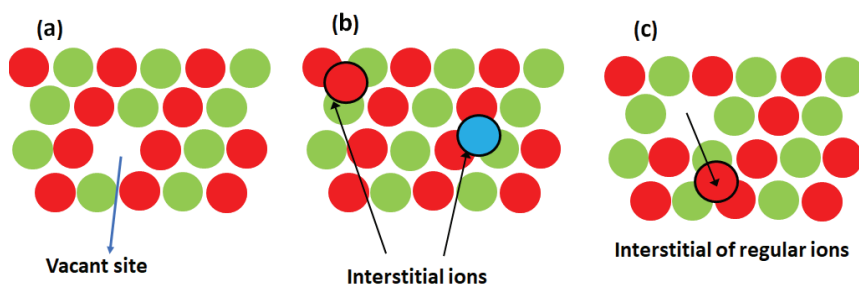


Figure 1.12: Diagram of point defects in ionic crystal due to (a) vacancies; (b) interstitials (foreign atom or a self-atom) occupying an off-lattice site; and (c) interstitials formed by atoms moving off-site creating, at the same time, a vacancy.

Interstitials: Another type of point defects is interstitial ions that occur when extra atoms occupy regions that are void in the perfect crystal, also known as off-lattice sites. This point defect is known as an interstitial defect. If the matrix atom occupies its own interstitial site, the defect is called *self-interstitial*. Self-interstitials in metals introduce large distortions in the surrounding lattice [57]. Self-interstitials tend to have a number of valence electrons different from the same atom in the crystal and, therefore, may form paramagnetic centers in diamagnetic or anti-ferromagnetic lattices. An example encountered in our work is Ni^{3+} centers in NiO.

Impurities: Foreign atoms are known as impurities. They can be deliberately added to the material to influence its electrical properties, or may be unintentionally added from contaminants in the synthesis precursors. Impurities may occupy a lattice site, in which case it is called a substitutional impurity or it may fill an interstitial site. Impurities also may have a different number of valence electrons than the surrounding medium, and thus form paramagnetic centers in a diamagnetic or antiferromagnetic crystal.

As said, specific point defects such as vacancies, interstitials and impurities may lead to paramagnetic centers in non-paramagnetic crystals. In addition, coordination defects also exist in disordered and amorphous solids where, locally, the coordination number is lower or higher than in most sites. These are termed coordination defects, and tend to form paramagnetic centers in diamagnetic amorphous solids as well.

A schematic diagram with the different known point defects in NiO is shown in Figure 1.12. Defects forming paramagnetic centers in antiferromagnetic NiO are particularly relevant to this study point defects (in particular: oxygen vacancies or Ni³⁺ ions interstitials) will be assigned to the paramagnetic centers to be detected by electron spin resonance in the work of this thesis. Hence, it was imperative to understand the nature of how these defects are created in materials, especially in an undoped NiO_x nanostructure. It is anticipated that the density of a specific defect type correlates well with electrical conductivity in nanostructured and non-stoichiometric NiO_x.

1.8.5 Charge-compensated Ni vacancies

Charge-compensated Ni vacancies: Non-stoichiometric materials are chemical compounds with non-integer values of the atomic composition. In certain cases, one of the positive ions is absent from its lattice site and the extra negative charge is balanced by some nearby metal ion acquiring two charges instead of one. The charge compensation could be achieved by changing their oxidation state.

In NiO_x, there is a creation of metal vacancies by heating in O² vapor in which some Ni²⁺ ions oxidized to 2Ni³⁺ to maintain electrical neutrality for 1 Ni²⁺ ion vacancy as shown in figure 1.13 (b). Another case of charge compensation for an absence of atom is either by Ni³⁺ ion and O⁻ or can be achieved by 2O⁻ as stated in panel 1.13 (c) and 1.13 (d) respectively. This type of defect is generally found amongst the compounds of transition metals which can exhibit variable vacancy and which can be specifically responsible for the electrical transport mechanism in NiO_x thin film.

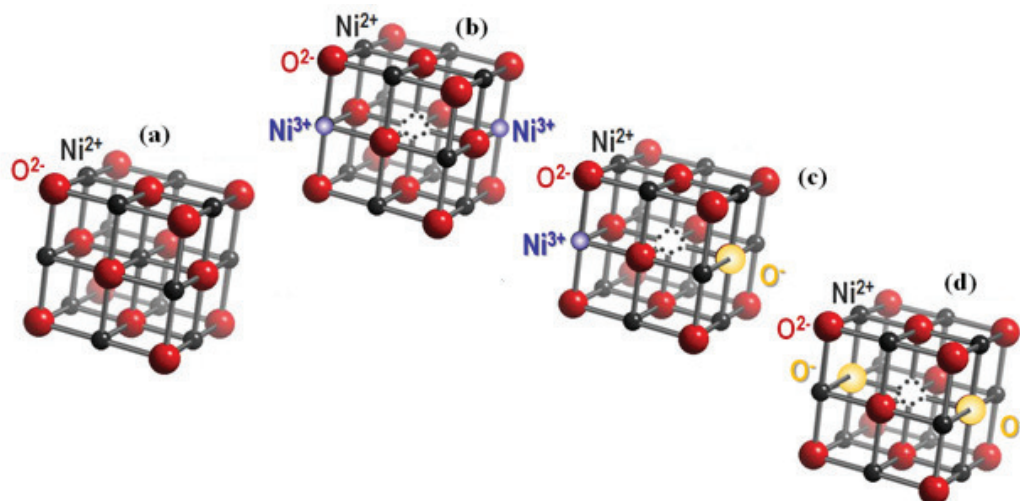


Figure 1.13: (a) The structure of ideal NiO crystal with diatomic (Ni, O) base face-centered cubic, (b) non-stoichiometric NiO_x with the presence of Ni²⁺ ion vacant site is compensated by 2Ni³⁺ centers, (c) NiO_x with vacancy is compensated by either Ni³⁺ ion center or O⁻ and (d) NiO_x with vacancy is compensated by 2O⁻

1.9 Summary and thesis overview.

In the introduction of this thesis, I have shown the different applications of nanostructured NiO_x particularly as a transparent electrode that makes use of hole injection in an optoelectronics device. Non-stoichiometric and nanostructured nickel oxide display some magnetic behaviour and to understand this phenomenon, different magnetic structures of matter were briefly discussed including diamagnetism, paramagnetism, ferromagnetism, ferrimagnetism and antiferromagnetism. Amongst these magnetic structures of matter stated here, antiferromagnetic NiO, an insulating material with zero magnetic moment though electrically conducting due to defects, is the area of interest.

NiO_x nanoparticles are very sensitive to size, crystal structure, and growth morphology of the sample. By varying the particle size of NiO_x, it leads to novel and interesting magnetic properties ranging from localized to bulk-like behavior. However, the appearance of defect-induced ferromagnetic surfaces in NiO nanoparticles residing at the surface are discussed and attributed to intrinsic point defects.

My motivation is mainly on the defect-induced electrical conductivity in non-stoichiometric nickel oxide thin film. On this content, the electrical transport in solids and in NiO are studied in which the charge transport in disordered and ordered material are presented. I discussed charge transport by extended states indicating that the charge carrier wave function is spread over the whole volume of a sample above the conduction band minimum where the electrical conductivity is dominated. Secondly, I discussed charge transport by hopping via localized states in which charge carriers are localized in a spatially restricted region below the mobility edge known as hopping conduction. These transport mechanisms play a very crucial role in understanding the mechanism of electrical conductivity in solids and in NiO_x thin films.

Therefore, my study will be divided as follows: in Chapter 2, I will discuss the experimental process used to deposit NiO thin film by solution growth method as one of the chemical processes of deposition. I will also describe the sample preparatory procedures, the advantages of solution growth method over other deposition methods, one of which is the ability to deposit over a wide range of deposition parameters. In this Chapter, I will discuss some basic concepts and instrumentation related to the main characterization techniques used in this thesis. They include, atomic force microscopy, X-ray diffraction (XRD), magnetic force microscopy, electron diffraction spectroscopy, UV-visible spectroscopy and electron spin resonance (ESR) measurement. ESR spectroscopy measurement is mainly my area of interest since it allows one to gain insight into the intricate paramagnetism of NiO_x samples grown at different temperatures.

Chapter 3 is based on my own research work. I will analyze and display the results of different characterized nickel oxide samples mentioned in Chapter 2 of this thesis. Amongst the characterized results shown, it was demonstrated that the ESR signal from nanostructured nickel oxide samples contains the signatures of two distinct types of magnetic centers. I will attempt to correlate the electrical conductivity of our samples with the concentration of either type of magnetic centers. In Chapter 4, I will conclude by summarizing my results and mention some future work for research direction.

1.10 References

- [1] P. Ravikumar, B. Kisan, A. Perumal, *J. of Appl. Phys. Adv.* **5**, 087116 (2015).
- [2] M. Jagodic, Z. Jaglicic, A. Jelen, J. B. Lee, Y. M. Kim, H. J. Kim and J. D. sek, *J. Phys. Condens. Matt.*, **21**, 215302 (2009).
- [3] S.S. Nkosi, B. Yalisi, D.E. Motaung, J. Keartland, E. Sideras-Haddad, A. Forbes, B.W. Mwakikunga, *J. Appl. Surf. Sci.*, **265** 860– 864 (2013).
- [4] M. Tadic, D. Nikolic, M. Panjan G. R. Blake, *J. of Alloys. and Compds*, **647**, 1061- 1068 (2015).
- [5] K. Karthik, G.K. Selvan, M. Kanagaraj, S. Arumugam, N. V. Jaya, *J. Alloys. Compds.*, **509** 181-184 (2011).
- [6] D. Alders, L. H. Tjeng, F. C. Voogt, T. Hibma, G. A. Sawatzky, C. T. Chen, J. Vogel, M. Sacchi, S. Iacobucci, *J. Phys. Rev. B* **57**, 11623 (1998).
- [7] A. Sundaresan, R. Bhargavi, N. Rangarajan, U. Siddesh, and C. N. R. Rao, *J. phys. Rev.* **74**, 161306 (2006).
- [8] H. L. Chen, *J. Surf. Coat. Technol.* **198**, 138 (2005).
- [9] H. Sato, T. Minami, S. Takata, T. Yamada, *J. Thin Solid Films*, **236**, 27 (1993).
- [10] T. Minami, H. Nanto and S. Takata, *Japanese J. Appl. Phy.* **23**, 280 - 282, (1984).
- [11] B. Issa, I. M. Obaidat, A. A. Borhan and Y. Haik, *J. Mol. Sci. Int.* **11**, 21266–21305 (2013).
- [12] W. B. Zhang, N. Yu, W. Y. Yu and B. Y. Tang, *J. Eur. Phys.* **64**, 153–158 (2008).
- [13] J. Cui, A. Wang, N.L. Edleman, J. Ni, P. Lee, N.R. Armstrong, T. J. Marks, *Adv. mater.* **13** 1476-1480 (2001).
- [14] D. Passeri, C. Dong, M. Reggente, L. Angeloni, M. Barteri, F. A. Scaramuzzo, F. De Angelis, F. Marinelli, F. Antonelli, F. Rinaldi, C. Marianecchi, M. Carafa, A. Sorbo, D. Sordi, I. WCE Arends, and M. Rossi, *J. Biomatt.* **4**, e29507 (2014).
- [15] M. Jlassi, I. Sta, M. Hajji and H. Ezzaouia, *J. Mater. Sci. in Semicond. Processing*, **21**, 7-13 (2014).
- [16] Y. H. Kwon, S. H. Chun, J. H. Han and H. K. Cho, *J. Met. Mater. Int.*, **18**, 1003-1007, (2012).

- [17] Y. Liu, Y. Li and H. Zeng, *J. nanomaterials* (2013).
- [18] P.S. Pati, I. L. D. Kadam, *J. Applied Sur. Science*, **(199)**, 211-221 (2002).
- [19] S. Morup and A. Hernando, *Studies of Superpara. in Sample of Ultrafine Particles, Nano magnetism*, Kluwer Academic Publishers, Boston pp. 93– 99 (1993).
- [20] H. K. Liu, G. X. Wang, Z. P. Guo, J. Z. Wang, K. Konstantinov, *T. Jour, J. New Mater. Electrochem. Syst.* **10**, 101 (2007).
- [21] E. R. Beach, K. Shqau, S. E. Brown, S. J. Rozeveld, P. A. Morris, *J. Mater. Chem. and Phys.* **115**, 371–377 (2009).
- [22] B.M. Ghosh, A. Sundaresan, C. N. R. Rao, *J. Mater. Chem.* **16** 106 (2006).
- [23] J. Y. Jeng, K. C. Chen, T. Y. Chiang, P. Y. Lin, Tzung-Da Tsai, Yun-Chorng Chang *Adv. Mater.* **26**, 4107–4113, (2014).
- [24] C.G. Granqvist, *Handbook of Inorganic Electrochromic Materials*, Elsevier, Amsterdam, the Netherlands, (1995).
- [25] J. Bandara and H. Weerasinghe, *J. Solar Energy Mater. Solar Cells* **85** 385 (2005).
- [26] D. Michael, D. Irwin, B. Buchholz, W. H. Alexander, P. H. C. Robert and J. M. Tobin, *The National Academy of Sciences of the USA*, **105**, 8 2783–2787 (2008).
- [27] A. W. Hains, ABF. Martinson, M.D. Irwin, Y. H Marks, *J. Polym Mater Sci Eng* **96**, 814 – 815 (2007).
- [28] R. J. Manders, S. W. Tsang, M. J. Hartel , T. H. Lai , S. Chen , C. M. Amb , J. R. Reynolds, and F. So, *J. Adv. Funct. Mater.*, **23**, 2993–3001 (2013).
- [29] F. Davar, Z. Fereshteha, M. S. Niasari, *J Alloys and Compds* **476** 797–801 (2009).
- [30] A. N. Spaldin, *Magnetic materials: fundamentals and device applications*. Cambridge Univ. Press, 89–106. (2006)
- [31] D.J Griffith, *Introduction to Electrodynamics*, Reed College, New Jeesey Press 07458 (1999).
- [32] C. Kittel, *Introduction to Solid State Physics*, (8th ed). Hoboken, NJ: John Wiley and sons, (2005).
- [33] D. Jiles, *introduction to Magetism and Magnetic Materials*, Chapman and hall, (1990).
- [34] Akbari-Sharbaf, *Defect-Related Magnetic and Electronic Properties of Graphene* The School of Graduate and Postdoctoral Studies Western University Canada,

- (2014).
- [35] B. Issa, I. M. Obaidat, A. A. Borhan and Y. Haik, *Int J. Mol Sci.* **14** 21266–21305 (2013).
- [36] T. Juagmarti, P. wadley, X. Marti and J. Wunderlich, *Nature Nanotechn.* **11** 231-241 (2016).
- [37] Duo, Lamberto, Finazzi, Marco, Ciccacci, *magnetic properties of antiferromagnetic oxide: Surfaces, interface and thin film.* (2010).
- [38] C. P. slitcher, *Principles of Magnetic resonance, springer series in solid state sciences,* (1978)
- [39] E. Brok, *Spin Structures in Antiferromagnetic Nanoparticles* PhD thesis Technical University of Denmark, (2013).
- [40] S. Thota, J. H. Shim and M. S. Seehra, *J. Appl. phys.* **114**, 214307, (2013).
- [41] C.G. Granqvist, *Electrochromic tungsten oxide films: Review of Progress, Solar Energy J. Mater. Solar Cells* **60** 201–262 (2000) .
- [42] M. Rubinsteina, R.H. Kodamab, A. Salah and C.I. Makhlof, *J. of Magnetism and Magnetic Materials* **234**, 289–293 (2001).
- [43] Brok, K. Lefmann, P. P. Deen, B. Lebech, H. Jacobsen, G. J. Nilsen, L. Keller, and C. Frandsen, *J. Phys. Rev. B* **91**, 014431, (2015).
- [44] V. Golosovsky, I. Mirebeau, G. André, M. Tovar, D. M. Tobbens, D. A. Kurduykov, and Y. A. Kumzerov, *J. AIP Adv.* **6**, 056104, (2016).
- [45] W.J. Duan, S.H. Lu, Z.L. Wu, *J. Phys. Chem. C* **116**, 26043-26051 (2012).
- [46] M. Tadic, D. Nikolic, M. P. Graeme, R. Blake, *J. of Alloys and Comps* **647**, 1061-1068 (2015).
- [47] N. Rinaldi-Montes, P. Gorria, D. Martínez-Blanco, A. B. Fuertes, I. Puente-Orench, L. Olivi, and A. B Jesús **6** 056104, (2016).
- [48] W. B. Zhang, N. Yu, W. Y. Yu and B. Y. Tang, *Eur. Phys. J. B*, **64**, 153–158 (2008).
- [49] G. Madhu, K. Maniammala and V. Biju, *Chem.Chem.Phys.*, **18**, 12135 (2016).
- [50] O. Madelung, *Introduction to Solid-State Theory*, ISBN 3-540-08516-5 Springer-Verlag Berlin Heidelberg New York, (1978).

- [51] S. D. Baranovsk and O. Rubel, *Charge Transport in Disordered Solids with Applications in Electronics*. John Wiley and sons, Ltd chi Chester (2006).
- [52] R. Gillen and J. Robertson, *J. Phys. Condens. Matter*, (2013)
- [53] S.H. Simon, *The Oxford Solid State Basics*, (ISBN978-0-19-968076-4) (2013).
- [54] Sze, S.M. and Kwok, N.G. (2006). *Phys of semicond. devices*. John Wiley & sons P. 789.
- [55] X. Zhu, X. Yu, and D. Yang *J. Crystal Growth*, **401**, 141-145, (2014)
- [56] W. Morris, Jr., C. R. Krenn, D. Roundy and m. L. Cohen, *J. mat. Sci. Eng. A*, 309-310, 121-124 (2001).
- [57] N. W. Ashcroft and N. D. Mermin, *Solis State Physics* (College edition), Highcourt College Publisher, (ISBN O-O3-38993-9) (1976).

Chapter 2

Experimental Techniques

My thesis is about a fundamental investigation of the origin of the electrical conductivity in nanostructured nickel oxide and nickel oxide-based thin-film materials. The study requires an efficient experimental procedure to deposit NiO_x thin films and a systematic characterization of their properties. Thin films of NiO_x can be fabricated by means of physical deposition processes such as thermal decomposition [1], pulsed laser deposition [2] and sputtering [3], all of which require ultra-high vacuum (UHV) equipment and hence are cost intensive. Wet chemical-based methods, including sol-gel, spray pyrolysis and solution growth methods, have also been used to fabricate nickel oxide samples [4-5]. Of the three wet-chemical techniques, the solution growth method guarantees efficient, defect engineered and reproducible fabrication of nickel oxide thin films required in this thesis work. With slight procedural modifications and manipulations both thin films and powder samples of nickel oxides with controlled defects are fabricated to suit different characterization requirements. Unlike the above mentioned physical deposition techniques, the solution growth method is cost efficient, requiring neither UHV equipment nor excessive high temperature needed for sol-gel method.

This chapter is comprised of two main sections. The first section describes in detail the principles of solution growth method adopted in this thesis work and some of the factors that allow us to control and optimize the deposition process, including the concentration of the reactant and complexing agents, the pH and temperature of the solution and the deposition time. These factors play significant roles in optimizing the deposition of nickel oxide thin films I report in this thesis. In the subsequent section, I will describe the characterization techniques used to study the properties of nickel oxide samples deposited by solution growth method.

2.1 Thin-Film Fabrication by Solution Growth Method

The solution-growth method of thin-film deposition is a wet-chemical based deposition technique that relies on slow release of metal ions from super-saturated solution. The

method is generally known as solution growth method or chemical bath deposition because films are deposited on a solid substrate from a reaction occurring in a solution in the presence of an appropriate complexing agent [6]. It has been used successfully to obtain thin films of oxides, sulfides, selenides and other semiconductor compounds because it offers several advantages over other methods of thin film fabrication [7-10].

With the solution growth method, films can be deposited on a non-planar substrate that might not be chemically or mechanically stable at high temperature [11]. The method does not require any sophisticated instruments such as UHV systems, and the starting chemicals are commonly available and cheap, and the preparative parameters are easily controlled. Many recent reports confirm that it produces uniform, adherent, and reproducible large area good quality thin films [12-13]. Hence, the method provides the prospect to fabricate devices requiring transparent electrodes, such as solar cells and light emitting devices, at a lower cost than those available in the market [14]. Added to its cost efficiency, the solution growth method allows easy control of growth factors, such as film thickness, deposition rate and quality of crystallites, by varying few deposition parameters such as solution pH, temperature and bath concentration. To control these growth factors to achieve specific purpose such as deliberate introduction of defects on NiO_x thin films required for our study, it is important to know the underlying principle of this deposition method as described in the following section.

2.1.1 Fundamentals of Solution-Growth Methods

The first step to obtain thin films by solution growth method is to prepare a reaction solution commonly referred to as the solution bath of the precursor of the sample to be deposited. For instance, a metal oxide film requires the solution bath containing the metal salts such as the chloride, sulphide, or nitrate of the metal. The metallic ions and non-metallic ions present in the bath react with each other and become neutral atoms which either precipitate simultaneously or very slowly in the reaction solution. When fast precipitation occurs in the solution, the expected film cannot form on the substrate immersed in the solution bath because of lack of stability and adhesion. When the reaction is constrained to proceed slowly, then a thin film of the neutral atoms is formed on the

substrate at optimal equilibrium condition [15]. The most common and effective way to achieve such slow precipitation is to add a suitable complexing agent to the reaction bath, which raises the ionic product of the precursor above the solubility product constant [16]. A supersaturation of the precursor is formed by dropwise addition of a suitable complexing agent, which would then gradually release metal ions in the solution [17]. Direct deposition of the film can then proceed by gradual release of the precursor ions from the supersaturated solution [18].

Two processes involved in the formation of the solid phase or thin films from the solution bath include nucleation and particle growth. Heterogeneous nucleation is a result of reaction taking place at the surface of the substrate, whereas homogeneous nucleation is a result of reaction occurring within the bulk of the solution to create the initial nuclei of the species [19]. In solution growth method, heterogeneous nucleation is mostly required as it allows fabrication of uniform thin films on substrates for potential application in devices. After the nucleation stage, the clusters of atoms or molecules formed undergo rapid decomposition and particles combine to build up to a certain thickness of the film on the substrate surface [15]. Substantial enhancement of the solution growth method facilitates the use of additional external factors to control the reaction medium during the synthesis process. For example, it is possible to control the film thickness and chemical composition by varying the deposition parameters such as bath temperature, precursor concentration, deposition time, complexing agents and the pH of the solution.

2.1.2 Factors influencing solution growth deposition

From the above section on the fundamental principle of solution growth method, it clearly appears that the film formation process is profoundly affected by the mechanism of precipitation and nucleation, which changes when certain critical growth factors reach their optimal condition. The influence of the reactant concentrations, temperature and pH of the solution bath, as well as the deposition time, are some of the deposition parameters or growth factors that have striking effects not only on the morphology and thickness of the ensuing thin films, but also on their quality, including film uniformity, crystallinity and defects. It is important to point out that careful optimization of these growth conditions are

important deposition steps to achieve the desired good quality films. In particular, control of the size, shape and orientation of NiO_x crystallites on the substrates is required for creation of high surface area materials for use in many types of devices including photovoltaic and optoelectronic devices [20].

In the general case of heterogeneous nucleation on a substrate, the film growth rate and the resulting thickness may be profoundly influenced by the solution bath temperature and the pH. For instance, when the bath temperature increases, the dissociation of the complexes in solution also increases, which leads to greater interaction between the metal ion and non-metallic ion in the solution [21]. The increased interaction between these ions ultimately increases the film growth rate via precipitation and subsequent nucleation of the neutral atoms on the substrate. For cations that are not easily hydrolyzed, such as Ni²⁺, precipitation of the metal hydroxide is promoted by raising the pH with a base such as ammonium hydroxide (NH₄OH) or by forming complexes with the metal using appropriate complexing agents [22]. The complexes are expected to act as a reservoir for metal, by buffering the free concentration to below the precipitation point. [23]. In solution processed NiO_x thin films, in which both the oxides and the hydroxides may form concurrently, the less stable phase in contact with a substrate will in general precipitate first. Under conditions such that the hydroxide precipitates first, varying the temperature or pH can result in the formation of the oxide via a dissolution/reprecipitation process or by a phase transformation. A lattice rearrangement, however, is more complicated and depends on the degree of rearrangement and dissolution of hydroxide to provide Ni²⁺. The uniformity of the initial hydroxide particles may be key in controlling the uniformity of the oxide particles as well [24].

The concentration of the reactants also plays a critical role in controlling the uniformity of thin film deposited by solution growth method. Due to less number of ions available for reactions at low concentrations, the films deposited in this condition are thin and mostly non-uniform. At a very high concentration, precipitation may occur extremely fast, and the ions do not have sufficient time to condense on the substrates, thus there will be fast precipitation in solution [25-27]. The growth of good quality thin films proceeds at a slower rate and deposition time could be used to control the film thickness and morphology by

producing uniform film with desired thickness since film thickness affects the optical properties of the films. In most cases, the thickness of the films increases up to a certain duration and then becomes saturated. After prolonged duration, the reactant ions available in the solution are exhausted leading to decrease in the thickness of the sample [28]. All the growth factors play an important role in fabricating high-quality films required for application in devices. To this end, sufficient efforts are made to optimize the conditions to make the contribution of each growth factor most relevant for our work.

2.2 Synthesis of nickel oxide by solution-growth

NiO_x thin films were deposited on Pyrex glass substrates using the solution-growth method. The step adopted in our fabrication process from solution bath preparation to post-deposition sample treatment is shown in Figure 2.1. All chemicals used in this experimental work were of analytical reagents grade and used without further purification. The fabrication of thin films of NiO_x requires the preparation of stock solutions of different concentration in the right proportions as described below.

2.2.1 Preparation of stock solutions

Different molar concentrations of the nickel precursor were initially prepared to optimize the deposition conditions described in the previous sections. 0.1 M and 0.25 M solutions of NiSO₄·6H₂O (Sigma-Aldrich, CAS Number: 10101-97-0) mol. Wt. 262.9 g/mol used as precursor reagent were obtained by dissolving 1.310 g and 3.275 g of NiSO₄·6H₂O separately in 50 ml of deionized water, respectively. Other concentration such as 0.5 M and 0.75 M solution of NiSO₄·6H₂O with molecular weight of (262.9 g/mol) were obtained by dissolving 6.550 g and 9.825 g of NiSO₄·6H₂O separately in 50 ml of deionized water respectively. 1 M solution of NiSO₄·6H₂O (262.9g/mol) were obtained by dissolving 13.10 g of NiSO₄·6H₂O in 50 ml of deionized water. Other reagents that were used for the experiment, such as potassium chloride as an additive for smoothing and moderating film thickness, were also weighed and recorded. Accordingly, 0.5 M solution of KCl with molecular weight of (74.55 g/mol) was obtained by dissolving 18.65 g of KCl in 500 ml of deionized water. Polyvinylpyrrolidone (PVP) (Sigma-Aldrich, CAS Number: 9003-39-8)

solution, which serves as surface passivation agent, was prepared and aged for 24 hours by dissolving 2.000 g of PVP in 500 mL of deionized water. This was stirred with a magnetic stirrer at 70 °C for 1 hour. The obtained solutions were kept in well labeled beakers as stock solutions from which the quantities required for bath preparation were collected.

2.2.2 Substrate cleaning

The choice of the substrate and methods used for the cleaning of the surface of the substrate is very important in the formation of thin films with reproducible process. Substrate cleaning usually involves removing surface contaminations like greasy particles and dust. To that effect, the Pyrex glass substrates we used in our experiment were cleaned by sonicating in detergent for 15 minutes, followed by rinsing with distilled water. Two additional sonication steps using first acetone and then methanol each for 15 minutes were performed. Clean substrates were dried in air and stored in clean petri dishes.

2.2.3 Deposition of Ni(OH): NiO_x

The optimized reaction bath for the deposition of thin films of Ni(OH): NiO_x contains 0.3 ml, of 1.0 M NiSO₄·6H₂O, and 1 ml of 30% aqueous ammonia (Sigma-Aldrich, CAS Number: 1336-21-6) added drop-wise into the mixture until a clear and blue coloured solution was formed. 7 ml of PVP solution was added to the mixture and stirred continuously for 1 minute to allow for sufficient mixing of the reactants. The pH of the mixture was kept in the range of 12.0 – 12.5 at 70 °C for 16 hours of deposition time. Five substrates of equal dimensions can be vertically immersed into the solution bath and supported on the walls of the beaker. In this way, the samples are deposited under the sample conditions and only the post-deposition annealing temperatures were varied for our studies on the electrical conductivity of NiO_x thin films and the fundamental intrinsic factors that control their transport properties widely reported in the literature.

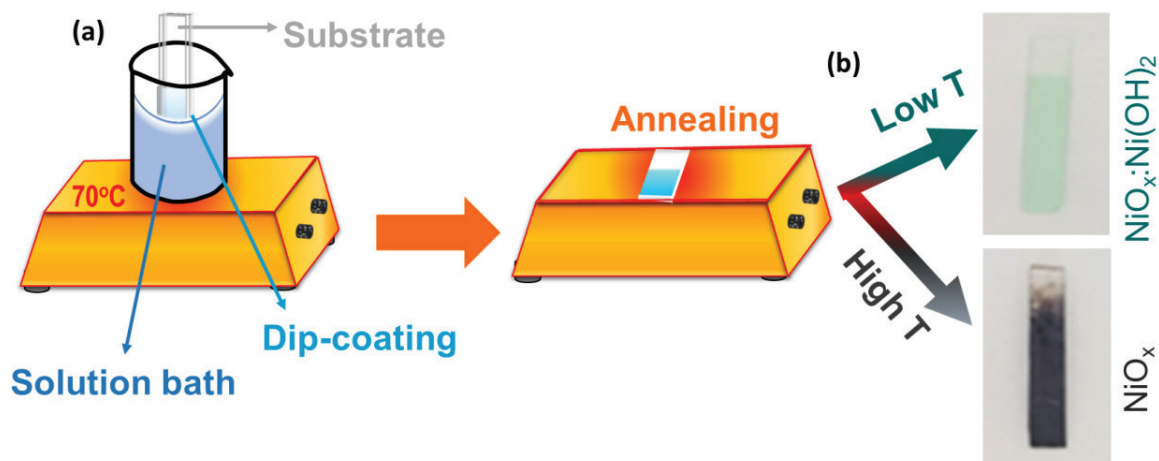
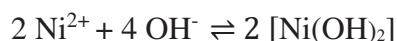


Figure 2.1: (a) Steps involved in the solution-growth method used for the deposition of NiO_x thin film. The set up consists of a beaker with precursor solution along with the Pyrex glass substrate inserted in it. (b) Post-deposition heat treatment from low to high temperatures of 225–500°C was used to control the thin- film properties. The as-deposited samples and those annealed below 300°C are greenish in color which changes to brownish to black color with increasing annealing temperature. The visually observed changes in the color of the films are expected to be accompanied by changes in the properties of the films and will be investigated in this thesis work.

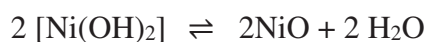
The step reaction involved in the complex ion formation and film deposition process for NiO_x is as follows. Nickel sulphate hexahydrate combine with ammonia in the alkaline medium to form tetra amine nickel ($[\text{Ni}(\text{NH}_3)_6]^{2+}$) complex ions which dissociate in solution to form nickel (II) ion complex and ammonia.



In the above reactions, ammonia solution was used as a complexing agent and is responsible for gradual release of nickel ions during the course of reaction. As we mentioned previously, to control the number of ions and rate of reaction, a complexing agent is needed to keep the metal ion in the solution and to prevent fast precipitating of hydroxide ions that are released by hydrolysis [29]. For the case of our nickel precursor complexed with ammonia, firstly, there is dissociation of the complexes to release Ni²⁺ ions as follows:



The nickel (II) ion combines with hydroxyl ion to form nickel hydroxide, which then precipitates and nucleates on the substrates. The as-deposited films were removed from the reaction bath, rinsed with deionized water to eliminate any overgrowth and dried in air. The uniformly deposited films are greenish in colour, as can be seen in the picture shown in Figure 2.1, panel (b). Deposited samples were subsequently annealed in air at different temperatures of 225 °C, 300 °C, 350 °C, 400 °C, 425 °C, 450 °C, 470 °C and 500 °C for 1 hour in order to determine the annealing condition at which nickel hydroxide films are converted to NiO_x nanostructure as expected from the following reaction.



Also, the visually observed changes in the colour of the films is expected to be accompanied by changes in some of the properties of the films and will be investigated in this thesis work.

2.3 Deposition of Nickel Oxide Powder samples

Nickel oxide powder samples were also prepared by using the same solution growth method described above. These samples were used for characterization by electron spin resonance (ESR) as described in section 2.4.4. The deposition was carried out at the same conditions of the deposited thin films with 0.3 ml, 1.0 M of NiSO₄.6H₂O, 1 ml of aqueous ammonia, and 7 ml of PVP. In the absence of substrates, homogenous nucleation became relevant and used to form a mass of Ni(OH)₂ on the deposition beaker shown previously in Figure 2.1. The resulting composite mixture was dried for 8 h at 80 °C in air to remove the solvent and water. Finally, the solid mass was annealed using a crucible at 450°C for 1 h to convert nickel hydroxide to nickel oxide nanostructures. The prepared NiO_x sample was split into two parts; one part for the bulk grains ESR measurements and the other part was further ground with mortar and pestle to be used for the ground grains measurement.

Crystal structure of the deposited film was verified by XRD characteristic which conforms with those obtained from thin film samples

2.4 Sample Characterization

2.4.1 X -ray Diffraction

Diffraction is the spreading of waves around obstacles and can happen with mechanical waves, very small moving particles which show wavelike properties such as electrons, neutrons, atoms or with electromagnetic radiations [30]. The phenomenon is most pronounced when the wavelength, λ of the radiation is comparable to the linear dimension of the obstacle. An array of obstacles, such as atomic lattice points can cause incident radiation to interfere with one another after diffraction. Since the interatomic spacing in crystals is $\sim 2 - 3 \text{ \AA}$, X -rays are the most suitable electromagnetic radiation to perform diffraction experiments. Geometrical interpretation by Bragg sets the limit to the interplanar distances for which diffraction is observed within a finite radius, $2/\lambda$ as:

$$\lambda = 2d \sin \theta, \quad 2.1$$

where θ is the diffraction angle and d is the interplanar distance shown in Figure 2.2. Constructive interference will occur if the extra distance traveled by the component of the wave that reflects off the further layer of atoms is an integer, n multiple of the wavelength:

$$n\lambda = 2d \sin \theta. \quad 2.2$$

Several points of equivalent planes can be in diffraction condition simultaneously which leads to multiplicity of a diffraction peak [31]. Since diffraction patterns of pure substances are unique, XRD experiments are routinely used to study the crystal structure of materials by measuring the position of diffraction peaks, given by 2θ , its intensity, I_{hkl} , where h, k, l are the Miller indices [32], and the peak profile shape.

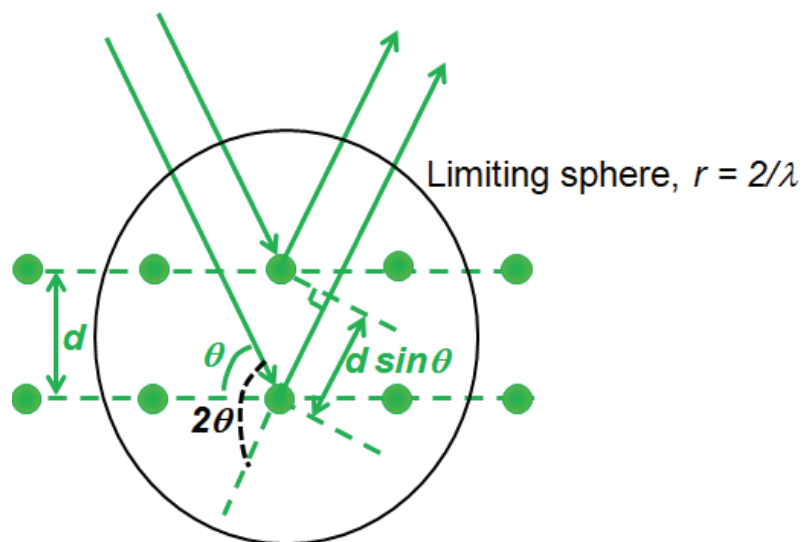


Figure 2.2: Bragg scattering off of a plane of atoms in a crystal. The extra distance traveled by the wave striking the lower plane is $2d\sin\theta$. All points representing planes that can diffract are inside a sphere of finite radius, $2/\lambda$

Figure 2.3 shows that the XRD experimental set up comprised of a sample irradiated with a collimated beam of X-rays of known wavelengths, a detector to intercept the scattered x-rays and a way to vary angle. The x-ray source is focused on the sample at some angle θ , while the detector opposite the source reads the intensity of the x-ray it receives at 2θ angle away from the source path. The incident angle is then increased over time while the detector angle always remains 2θ above the source path. Powder diffraction or the Debye–Scherrer method is the use of wave scattering on a sample which is not single crystalline, but is powdered [33]. Because one does not need single crystals, the method can be used on a much wider variety of samples. In this case, the incoming wave can scatter off any one of many small crystallites which may be oriented in any possible direction [31]. The most pertinent results of powder XRD characterization consist of plot of peaks in the scattered x-ray intensity as a function of scattering angle, one can obtain information on phases present, crystal structure, defects, crystallite sizes, crystal orientation, strain, as well as its location.

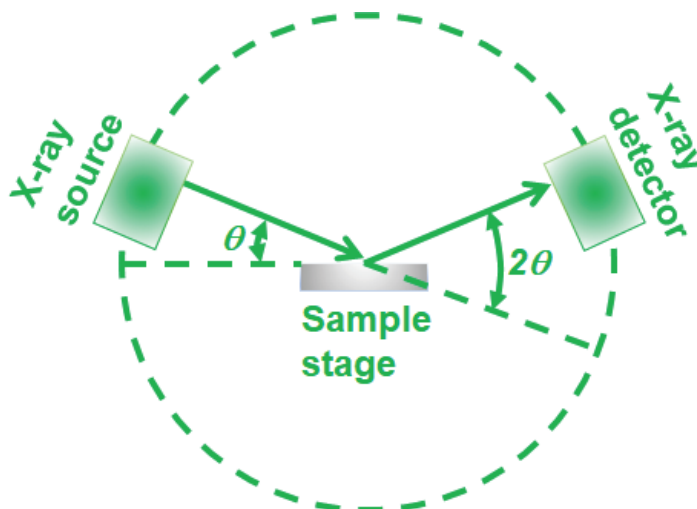


Figure 2.3: Debye Scherrer powder diffraction experiment set-up comprises of an x-ray source oriented at an angle θ to the sample stage and a detector opposite the source that records the intensity of the diffracted x-ray at 2θ angle. The incident angle of the x-ray can be increased during sample exposure while the detector angle always remains at 2θ above the source path.

In this thesis work, the crystal structure of NiO_x thin films were studied by x-ray powder diffraction using the Nonius Kappa CCD powder x-ray facility in the Department of Chemistry at Western University Canada. The picture in Figure 2.4 shows that the x-ray diffractometer is enclosed in a glass house to minimize possible exposure risks. With this diffractometer, the structural compositions of the sample are determined by observing the sample from all possible directions, and measuring the spacing for several orientations and subsequently comparing them with the known spacing. In this experiment, a $\text{Cu K}\alpha$ source operated at a wavelength, λ of 1.5418 \AA were used to obtain the diffraction patterns of thin films of NiO_x at diffraction angle (2θ) in the range of 35° to 110° . In this way, I studied the crystal structure of my sample as a function of the annealing temperature and determined at what temperature the as-deposited sample of predominantly Ni(OH)_2 is completely transformed to the oxides, NiO_x .

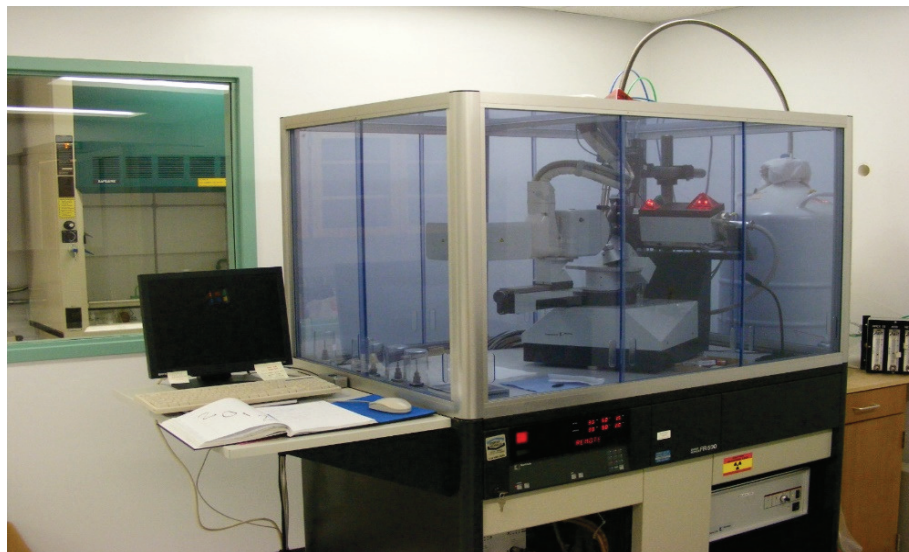


Figure 2.4: Nonius Kappa CCD powder X-ray facility in the Department of Chemistry at Western University, Canada. The diffractometer was used in this work to study the crystal structure of NiO_x thin films at different annealing temperatures.

From the profiles of the x-ray diffractograms, we calculated the crystallite size of NiO_x fabricated in this work as a function of the post-deposition annealing temperature. The average grain size, D of the film was determined from the width of the diffraction peaks using Scherrer's formula,

$$D = 0.9\lambda / \beta \cos \theta \quad (2.3)$$

where λ is the wavelength of the x-ray, θ is the Bragg angle and β is full width at half maximum (FWHM) of the diffraction profile. To compare the X-ray diffraction peaks observed in my samples selection rule also known as systematic absence was employed since it tells us which scattering peaks must be absent for a given lattice. In this analysis, simple cubic allows scattering from any plane (h, k, l), in bcc, (body centered cubic) the lattice plane (h + k + l) must be even and in FCC, face centered cubic (h, k, l) plane must be all odd or all even [32]. The lattice planes (hkl) were identified from the selection rules which correspond to JCPDS data for our sample of NiO_x. The interplanar distance of the films was calculated using the relations for cubic structure given by

$$d = \frac{a}{\sqrt{h^2 + k^2 + l^2}} \quad (2.4)$$

where h, k, l are miller indices and a , the lattice constant of NiO_x is 4.175 Å. The XRD analyses of NiO_x nanostructure of as-grown sample, and the samples annealed at 300°, 450° and 500° are shown in Table 2.1. The table comprises of the theoretical and experimental results of the diffracted peaks, diffraction angle (2θ) and intensity. The theoretical intensity, I was calculated from the relation following relation:

$$I \propto M_{\{hkl\}} |S_{\{hkl\}}|^2 \quad (2.5)$$

where $M_{\{hkl\}}$ is the multiplicity factor and the structure factor, $S_{\{hkl\}}$ is expressed as:

$$S_{\{hkl\}} = \sum f_j e^{2\pi i(hx_j + ky_j + lz_j)} \quad (2.6)$$

Table 2.1: Comparison of the experimental and theoretical values of the Bragg angle and intensity of XRD reflection of NiO_x showing fcc structure.

{hkl} fcc	2θ (degree)		Intensity	
	Theory	Experiment	Theory	Experiment
111	37.0	37.2	1.000	0.604
200	43.3	43.1	0.766	1.000
220	63.3	62.6	0.445	0.491
311	76.4	76.2	0.398	0.226
222	80.3	80.4	0.093	0.264
400	95.2	95.7	0.036	0.113
333	107.4	108.1	0.157	0.226

All the peaks reflection from the XRD diffraction displays face-centered cubic (FCC) nickel oxide structure. Above 300°C, peaks associated to Ni(OH)₂ phases observed in as-

grown sample are absent. This observation indicates that when fabricated and at annealing temperatures below 300°C, the sample is composed of NiO_x:Ni(OH)₂, but as the annealing temperature increases above 400°C, the mixture of NiO_x:Ni(OH)₂ is completely converted to NiO_x nanostructure. To further confirm that our sample consists of nanostructure NiO_x, we compare the theoretical and experimental result for both scattering intensity with the corresponding 2θ angle of diffraction for sample annealed at 500°C and is shown in Figure 2.5. The result confirms that our sample consists of NiO_x fcc cubic structure since the experimental intensities are comparably close to the theoretical results based on FCC structure for the entire range of 2θ angle studied.

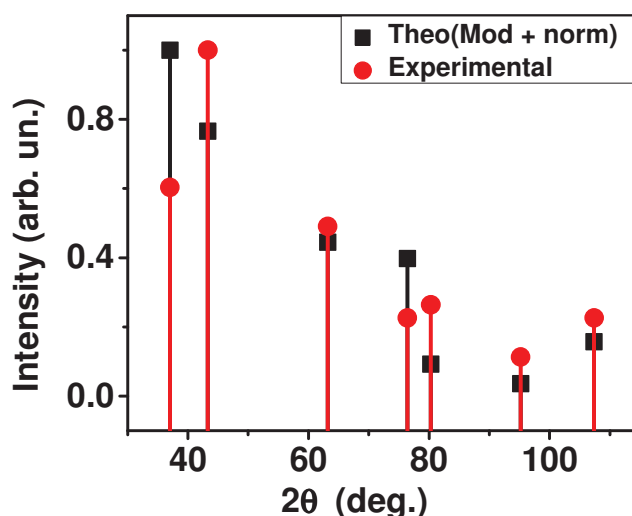


Figure 2.5: Plot of theoretical and experimental scattering intensities versus 2θ angle for NiO_x thin films annealed at 500°C. The experimental intensities match well with the theoretical calculation based on FCC structure.

2.4.2 Atomic force microscopy

Atomic force microscopy (AFM) is an imaging technique used to probe the shape of a surface in three-dimensional detail, down to the nanometer scale [34]. The technique is apt

to study the surface topography of both hard and soft materials, synthetic and natural, irrespective of opaqueness or conductivity. As a result of its versatility, sensitivity and high resolution, the Witec Alpha 300S atomic force microscope was used by us to measure the surface topography and the thickness of NiO_x thin films studied in this thesis work. The Witec Alpha 300S system comprised of a microscope stage, an integrated optical microscope to view the sample and the tip, and a computer to control the software and acquires and displays AFM images. The microscope stage contains the scanner that moves the AFM tip relative to the sample, sample holder and a force sensor to monitor the tip. The stage is supported on a vibration isolation platform which reduces noise and increases the resolution obtainable.

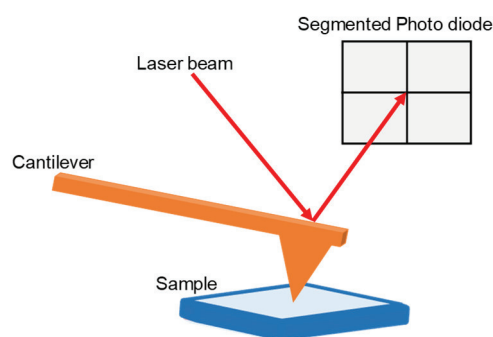


Figure 2.6: The AFM cantilever showing the laser beam centrally positioned on a segmented photodiode at which the cantilever is considered to have zero deflection. Movement of the cantilever during a sample scan deflects the laser beam relative to the initial position and be used to reconstruct the topography of the scanned surface at nano/micro scale resolution.

In a typical AFM measurement to acquire the topography images of a surface, a sample is scanned under the tip by using a piezoelectric scanner that moves the sample precisely in x , y , and z directions in response to an applied voltage. The sample and the tip exert forces on each other, which results in cantilever deflection. The deflection of the cantilever is detected by measuring the displacement of a laser beam reflected from the back side of the cantilever using a position sensitive photodetector such as the segmented photodiode shown in Figure 2.6. In this configuration, the shifts in the position of the laser beam from the initial central spot on the segmented photodiode in response to the deflection of the cantilever are detected, measured and subsequently processed by the computer to create

the surface morphology of the sample. The actual deflection of the cantilever and the way topography images are constructed can vary, depending on the mode of operation of the system, which includes contact mode operation, intermittent-contact and non-contact mode. The differences between the modes lead not only to different experimental procedures, but to differences in the information available, differing suitability for samples, and even to differences in interpretation of data as described below.

2.4.2.1 Contact mode operation of AFM

In contact mode AFM, the tip is brought into close proximity of the sample, on the order of a few angstroms, to create soft physical contact. At such a distance, the electronic clouds of the tip and the sample's atoms strongly interact, which results in a strong repulsive force between them [12, 35]. The force -distance curves shown in Figure 2.7 describes the atomic interaction forces between the AFM tip and a sample surface used to classify the modes of AFM operation into contact, non-contact and tapping modes. As shown in this Figure, when the tip is far from the sample surface, the cantilever is considered to have zero deflection and the focused laser beam is assigned a central spot in the segmented photodiode shown previously in Figure 2.6. In operation, the change in the cantilever amplitude due to the tip-sample spacing produces a corresponding deflection of the laser beam on the photodiode and is used to extract the topographical data of the scanned sample.

In contact mode AFM, the sample can be said to be in a physical contact with the tip as the instrument pushes the cantilever towards the sample surface, within a few angstroms, to achieve sample - tip interaction in the repulsive regime [34]. As a result of the proximity and repulsive force between the tip and the sample, the sample or the tip or both can be damaged by the scanning process. This makes this mode of operation limitedly applied to soft and sensitive samples. However, the method is suitable for measurements requiring physical contacts such as those required for imaging steps or abrupt transition in sample surface to obtain sample thicknesses. Since our sample of NiO_x is stable under such measurement conditions, their thicknesses were determined using the AFM operation in contact mode.

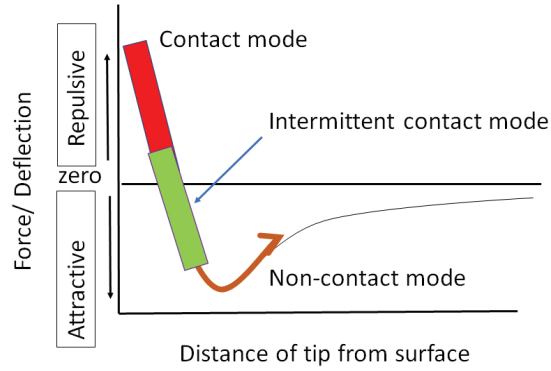


Figure 2.7: Atomic interaction forces between the AFM tip and the sample surface, which classifies the modes of AFM operation into contact, non-contact and (tapping) modes.

2. 4.2.2 Non-contact mode/close-contact mode

To achieve non-contact AFM, the tip must be close enough to the sample surface without passing into the repulsive regime used for contact mode AFM. Non-contact AFM is therefore carried out in the attractive regime, as shown in Figure 2.7. By using a highly stiff cantilever and monitoring the dynamic effects of the attractive force in this regime, it is possible to maintain the cantilever very close to the surface without jumping to the repulsive regime. Unlike the case of contact mode in which the oscillation amplitude of the cantilever is the parameter of interest, with/in non-contact AFM operation, it is possible to observe both the cantilever oscillation amplitude and the phase. These effects are caused by a change in the cantilever resonant frequency which is in turn caused by forces from the surface acting on the tip. Such resonant frequency ω_0 is given in terms of the spring constant, k of the cantilever as described by the following equation:

$$\omega_0 = c\sqrt{k}, \quad (2.7)$$

where c is a function of the cantilever mass. Due to the additional force f from the surface the actual resonant frequency ω_0' during the AFM operation is:

$$\omega_0' = c(\sqrt{k - f'})f \quad (2.8)$$

where f' is the derivative of the force normal to the surface. All AFM modes involve the probe moving into the force field of the sample surface, including 'non-contact' AFM [36].

2.4.2.3 Intermittent contact (or tapping mode)

Intermittent contact mode, also called AC or tapping mode, is like non-contact mode except that the tip is brought closer to the sample. The tip barely touches or taps the sample surface at the end of its vibration without any sliding towards the sample surface. The interatomic force between the tip and sample is repulsive when the tip touches the sample surface, while the force is attractive for the rest of the tip oscillation. In intermittent contact mode, as the tip gets closer to the sample, the amplitude of the vibrating cantilever decreases and can be controlled by applying another voltage to prevent contacting and dragging the tip to the sample surface. Similar to the non-contact regime, the change in the cantilever amplitude due to the tip-sample spacing is used to extract the topographical data. Intermittent contact mode has proved to be beneficial for many applications. In comparison to contact mode, the intermittent contact mode is less sample damaging because it eliminates lateral forces, including friction, between the tip and sample. This prevents surface deformation and tip degradation, which may occur in contact mode scans. Detecting both repulsive short range and attractive long-range forces in the intermittent contact mode increases the signal-to-noise ratio of the detected forces between the tip and sample in comparison to the non-contact mode, which only detects the attractive long-range forces. This is beneficial for easier measurements of the force and, in turn, morphological investigation [12,35]. As a result, this mode of operation was adopted in this work to measure and obtain the topography images of the NiO_x thin films studied in this thesis work.

2.5 Magnetic force microscopy

Magnetic force microscopy (MFM) is an intermittent AFM based technique in which a ferro-magnetic tip is used to probe local magnetic fields with the typical AFM spatial resolution, thus allowing one to acquire images reflecting the local magnetic properties of the samples at the nanoscale [37]. In MFM/AFM based measurement, only the long-range tip-sample interaction forces i.e., electrostatic and magnetic forces affect the cantilever motion [38]. Two scans are made at the same sample location: A first scan is made prior to tip magnetization and only probes the electrostatic forces and a second scan is made after the tip magnetization probes the resultant of electrostatic and magnetic forces. The phase

shift value between the demagnetized and magnetized images indicate the existence of ferromagnetic surface due to extended states residing at the surface of the material.

Herein, the magnetization patterns, specifically the ferromagnetic ordering of NiO_x thin films, was characterized by magnetic force microscopic (MFM) using a Witec Alpha 300S AFM system based technique with a silicon SPM magnetic tip of 75 kHz resonance frequency and 3.0 N/m spring constant of cantilever was used to probe the samples. MFM images indicate the existence of ferromagnetic surface due to surface defect residing at the surface of the material by calculating the phase shift value between the demagnetized and magnetized MFM image. The observed ferromagnetic surface occurred when the magnetic tip is brought into close proximity with the sample and antiferromagnetic spins present in the material tend to align parallel to the direction of the applied external magnetic field from the tip [39].

2.6 Electron spin resonance

Electron spin resonance (ESR) was firstly established in 1945 [40] and is employed for studies of free radicals, transition-metal ion complexes, and other paramagnetic substances, most commonly in liquids and solids. The absorption of microwave energy causes a transition from a lower energy state to a higher energy state. The microwave radiation in the gigahertz range (GHz) with a wavelength of a few cm (or 3 cm) is used for EPR experiments and such radiation lies far outside the visible region. The energy differences studied in EPR spectroscopy are predominately due to the interaction of unpaired electrons in the sample with a magnetic field produced by a magnet in the laboratory. This effect is called the Zeeman Effect. Thus, the energy becomes split in $(2s+1) = 2$ “Zeeman levels”, as shown in Figure 2.8. \mathbf{S} is an intrinsic angular momentum of electron called spin. The magnetic field, \mathbf{B} , produces two energy levels for the magnetic dipole moment, μ_B , of the electron in eq. (2.9) and (2.10). Because the electron is a spin $\frac{1}{2}$ particle, the parallel state is designated as $m_s = -\frac{1}{2}$ and the antiparallel state is $m_s = +\frac{1}{2}$. The energy of each orientation is the product of μ_B and \mathbf{B} . For an electron, $\mu_B = m_s g_e \beta$, and g_e is the spectroscopic g -factor of the free electron and equals 2.0023192778 (≈ 2.00). Therefore, the energies for an electron with $m_s = +\frac{1}{2}$ and $m_s = -\frac{1}{2}$ are respectively,

$$E_{1/2} = \frac{1}{2} g_e \beta B, \quad (2.9)$$

$$E_{-1/2} = -\frac{1}{2} g_e \beta B, \quad (2.10)$$

The two spin states have the same energy in the absence of a magnetic field, so without a magnetic field, there is no energy difference to measure. The energies of the spin states diverge linearly as the magnetic field increases and the energy difference depends linearly on the magnetic field. Transition between the two Zeeman levels can be induced if the system takes up energy in the form of electromagnetic radiation of a suitable frequency ν . The resonance condition then applies:

$$\Delta E = g_e \beta B = h \nu \quad (2.11)$$

where ΔE is the energy between the two spin levels, Planck's constant $h = 6.62607004 \times 10^{-34} \text{ m}^2 \text{ kg / s}$ and ν is the microwave frequency. Since β is a constant and the magnitude of \mathbf{B} can be measured, all we need do to calculate g is determine the value of ΔE , thus:

$$g = \frac{h \nu}{\beta B} \quad (2.12)$$

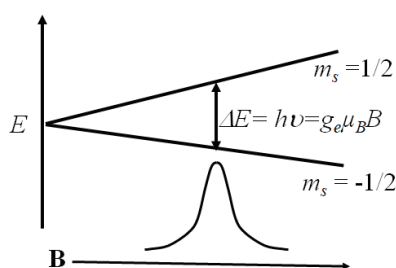


Figure 2.8: Zeeman splitting of energy levels of an electron placed in a magnetic field, \mathbf{B} . The absorption of microwave energy causes a transition from a lower energy state to a higher energy state.

The frequency is usually kept constant, and the magnetic field strength is varied so that resonance occurs. The system will then absorb energy from the electromagnetic field. This field contains both an electric and a magnetic component. When the magnetic field has a value corresponding to the applied microwave radiation known as field resonance, energy

is absorbed and the power reaching the detector decreases and ESR spectra is obtained. Absorption can occur as long as the number of particles, atoms, radicals etc. in the lower state, N_- exceeds the number N_+ of the upper state. At equilibrium the ratio predicted by the Boltzmann distribution is $N_+/N_- = e^{-\Delta E/kT}$. To get a strong signal, ΔE must be large, which in turn implies that the sensitivity increases with increasing energy difference ΔE , that is the microwave frequency [41].

The principle of ESR spectrometer and its operation have been discussed in section 2.6. However, we will focus on the description ESR spectrometer. A simple electron spin resonance spectrometer consists of a microwave generator that transmits electromagnetic energy via a waveguide through a cavity containing the sample and to a detector. The cavity is located between the poles N and S of a magnet. Modern ESR spectrometers are much more complex than the simple instrument. The continuous wave (CW) spectrometers are still mostly employed [40]. The cavity is placed in a microwave bridge, thus avoiding the microwaves to reach the detector except at resonance. The magnetic field is modulated at high frequency, where 100 kHz is commonly employed. Because of the field modulation and the phase-sensitive detection, the spectrum is recorded as the first derivative of the absorption. The details of phase-sensitive detection scheme will be shown in section 2.6.4 of this chapter. Therefore, major components of an ESR spectrometer are the Helmholtz-coil electromagnets, the microwave unit, the resonator, the field modulation system, the power attenuator, able to attenuate the microwave power from 200 mW down to a few nW, and the detection system comprising a locked-in diode [42]. A block diagram showing the components of the ESR spectrometer is shown in Figure 2.9.

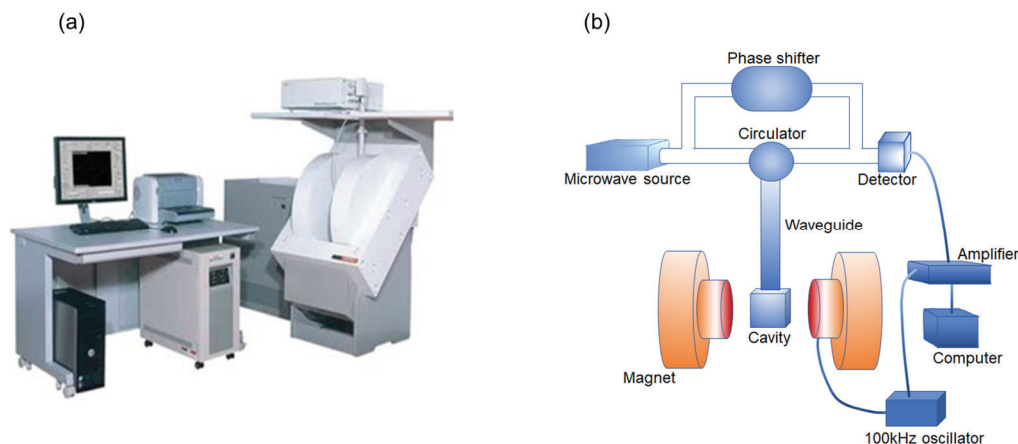


Figure 2.9: (a) Jeol JES-FA200 ESR spectrometer; and (b) block diagram of the main components of an ESR spectrometer employing magnetic field modulation. The method is utilized to improve the signal-to-noise ratio by phase-sensitive detection. The principle for obtaining the derivative of the absorption is shown.

My ESR measurements were carried out on a Jeol JESFA200 ESR spectrometer, shown in Figure 2.9, equipped with a rectangular- TE_{102} resonator, a 200 mW X-band microwave generator (9-10 GHz frequency) and a liquid-nitrogen cryostat for measurements below room temperature, down to 100 K.

2.6.1 Microwave power and relaxation times

The ESR signal intensity depends on the square root of microwave power as shown in Figure 2.10, because the power that can be stored in the spin system in the form of magnetization is proportional to the square of magnetization field H :

$$P_{\mu W} = H^2/2\mu_0. \quad (2.13)$$

If low enough microwave power is used, the signal intensity, proportional to the magnetization, grows as $P_{\mu W}^{1/2}$ and at higher power levels, the signal grows more slowly, or even diminishes, with increasing microwave power levels. This behavior is called saturation [43].

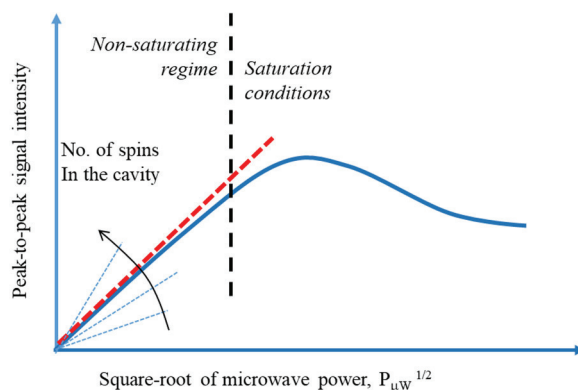


Figure 2.10: Power saturation curve, in which the signal amplitude is expressed as a function of the square root of the incident microwave power.

A simple way to check the lack of saturation is to increase the power by a factor 4, as the spectrum amplitude should double in these conditions in a non-saturating system. Saturation occurs if a significant proportion of the spin population is in the excited state with limited possibility to release its energy. The release of energy may occur via spin relaxation, characterized by a spin–lattice relaxation time, T_1 , and a spin-spin relaxation time, T_2 . In spin-spin relaxation processes there is energy exchange only within the ensemble of the spins, without dissipation of energy. Hence, T_2 is related to signal width, i.e., $T_2 \propto \Delta H_{pp}^{-1}$. Relaxation time of a system due to T_2 long means that spins are very localized. Long T_2 spins interact less with each other and are more isolated. This is consistent with localized defects near a vacancy either Ni^{3+} or O^- . T_1 is the time taken by the excited electron spin to dissipate energy and transfer heat to the system in the form of lattice vibrations, or phonons. In this way, the microwave energy is released as heat. Saturation occurs if the spin-lattice relaxation rate is too slow, compared to the amount of energy introduced in the system in the form of microwave power, to dissipate microwave energy to the lattice. Therefore, measurements under saturation conditions can be used to estimate T_1 under specific assumptions [43].

2.6.2 Magnets

The magnetic field controller defines the center field and sweeps the magnetic field for the scan. The ESR spectrum is measured by placing the sample between the two magnetic coils in the resonant cavity. The magnitude of the field generated by the electromagnets can be

varied between 0 T to 1.7 T in our spectrometer. For $g \sim 2$, X-band resonance typically occurs at about 330 mT [44]. The magnetic field regulation occurs via a Hall probe placed in the gap of the magnet. It produces a voltage that is dependent on the component of the magnetic field that is perpendicular to the probe. Regulation is accomplished by comparing the voltage from the Hall probe with the reference voltage given by the other part of the controller. When there is a difference between the two voltages, a correction voltage is sent to the magnet power supply that changes the amount of current flowing through the magnet windings and hence the magnetic field [42].

2.6.3 Radiation source and resonator system

The resonator is responsible for the sensitivity of the ESR spectrometer. This is most commonly a resonant cavity, which admits microwaves through an iris. Resonator is a cavity with a metal box and the inner walls is coated by high reflectivity metal in the microwave range i.e., gold and houses the sample during the measurements. The cavity is either rectangular or cylindrical shape which resonates with microwaves. The cavity or resonator is designed to set up a pattern of standing microwaves in its interior. Standing electromagnetic waves have their electric and magnetic field components exactly out of phase - where the magnetic field is maximum, the electric field is minimum and vice versa. The place where the sample is situated has a minimum electric field and maximum magnetic field. The importance of having a minimum electric field at the location of the sample is to reduce dielectric losses of the microwave field. Resonance means that the cavity stores the microwave energy; therefore, at the resonance frequency of the cavity, no microwaves will be reflected, but will remain inside the cavity. Energy can be lost to the side walls of the cavity because the microwaves generate electrical currents in the side walls of the cavity which in turn generates heat. The microwave and the magnetic field drives the absorption in ESR. Therefore, if the sample is placed in the microwave electric field minimum and the magnetic field maximum, the biggest signals and the highest sensitivity is achieved [42].

2.6.4 Phase-sensitive detection system

ESR use a technique known as phase-sensitive detection to enhance the sensitivity of the spectrometer. This process encodes the ESR signals to make it distinguishable from sources

of noise or interference that are almost always present in a laboratory. The detection scheme works as follows. The magnetic field strength which the sample sees is varied sinusoidally at the modulation frequency (usually 100 kHz, see Figure 2.11). This modulation is accomplished by placing a pair of coils on both sides of the cavity along the axis of the direct current (DC) field in which the coils are driven by an alternating current at 100 kHz that produces the modulation. If there is an ESR signal, the field modulation quickly sweeps through part of the signal and the amplitude of microwaves reflected from the cavity is modulated at the same frequency. The signal channel (more commonly known as a lock-in amplifier or phase sensitive detector) produces a DC signal that is proportional to the amplitude of the modulated ESR signal. It compares the modulated signals with a reference signal having the same frequency as the field modulation, and it is only sensitive to signals that have the same frequency and phase as the field modulation. Any signals (such as noise and electrical interference) that do not fulfill these requirements are suppressed [42]. This scheme limits the amplification of electrical noise that normally occurs at frequencies that are different from the reference, which leads to dramatic improvements in the signal-to-noise ratio. Only the amplitude modulated signals are detected. By this scheme, the ESR signal is transformed into a sine wave with an amplitude proportional to the slope of the absorption curve. Consequently, the output of the 100-kHz phase-sensitive detector is the derivative of the absorption curve. There are two parameters associated with the phase sensitive detection: modulation amplitude, and modulation frequency. These parameters should be chosen wisely. With more magnetic field modulation, the intensity of the detected ESR signals increases; however, if the modulation amplitude is too large (larger than the linewidths of the ESR signal), the detected ESR signal broadens and becomes distorted [44].

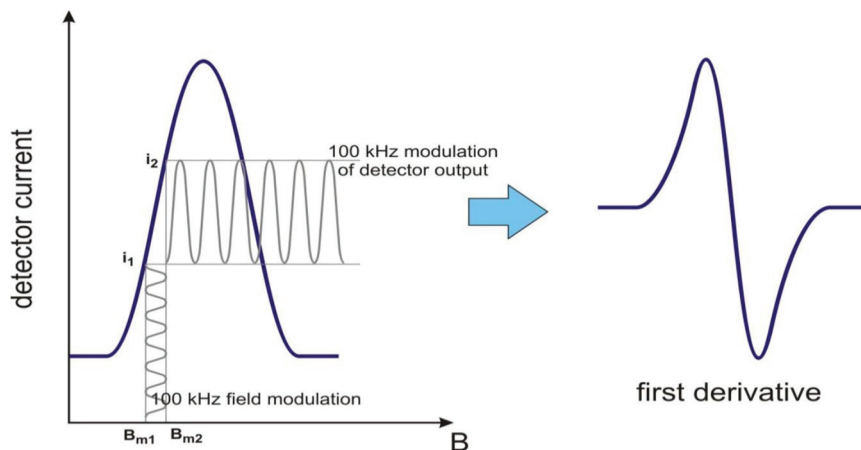


Figure 2.11: Schematic of phase-sensitive detection system. As the main field is scanned slowly through the ESR line, a small additional oscillating magnetic field, B_m , is applied in the same direction as the main magnetic field. B_m is commonly at 100 kHz. As B_m increases from the value B_{m1} to B_{m2} , the crystal detector output increases from i_1 to i_2 . If the magnitude of B_m is small relative to line width, the detector current oscillating at 100 kHz has a peak-to-peak value that approximates the slope of the absorption curve. Consequently, the output of the 100-kHz phase-sensitive detector is the derivative of the absorption curve.

2.6.5 Signal intensity

The integrated intensity of the ESR signal is proportional to the concentration of unpaired electrons in the sample, provided that appropriate operating conditions are used. The ESR signal is recorded as the first derivative of the absorption spectrum, because it is achieved through lock-in detector at modulation frequency [45]. Figure 2.12 is an illustration of the area under the absorption curve obtained from double integration and is needed to precisely quantify the ESR signal intensity shown in Figure 2.12, where I_s is ESR signal intensity, B is the main magnetic field, N_{sample} is the number of spins in the sample.

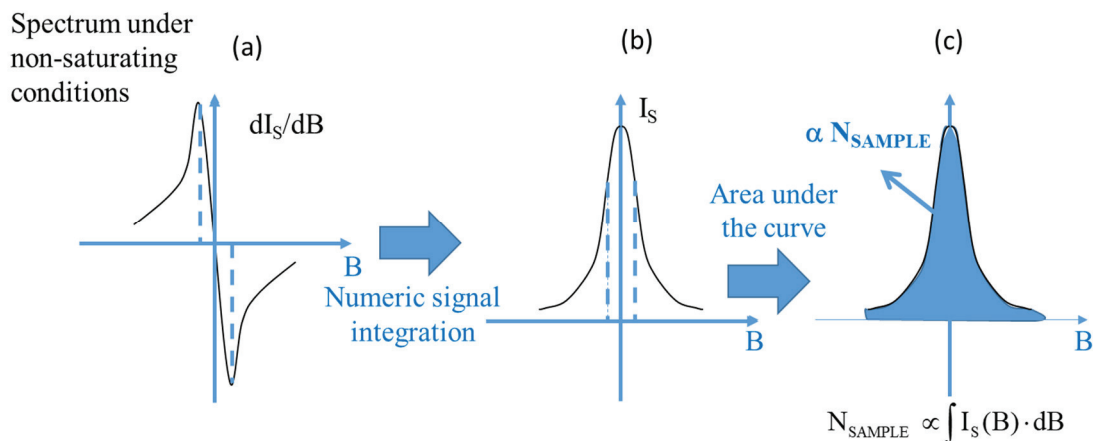


Figure 2.12: (a) Schematic diagram of first derivative of the absorption spectrum, (b) Area under the absorption curve (obtained from double integration) and (c) The number of spins in the sample is proportional to the area under the curve.

2.6.6 Spin density and areal spin density calculations

Estimates of the spin density must be carried out by comparison with a reference sample. A signal marker is placed in a dedicated compartment of the resonant cavity simultaneously with the sample. In our case, the marker is made by a rod of MnO, a paramagnetic oxide that gives an ESR signal formed by six equally spaced and equally intense narrow resonance lines, easily recognizable from most of the sample signals. The MnO rod can be inserted or extracted from the cavity to produce a marker signal intensity comparable to the sample signal intensity, but the number of spins in the marker cannot be used to infer the total spin number in the sample because different cavity regions have a different sensitivity to magnetization. Therefore, the estimate of N_s , the total number of spins in the sample requires two distinct experiments: in the first measurement, a reference system with known total spin number N_T is placed in the cavity, and the intensity of its signal is compared to the marker signal intensity; in the second experiment, the NiO_x sample with unknown spin number N_s is measured under the same conditions, and comparison of the intensity of the MnO marker signal, which can be different in the two runs, allows for an accurate comparison of the intensities of the reference and sample signal, which leads to the determination of N_s .

Further assumptions are required to determine the sample spin concentration from the total sample spin number. One can assume that spins are uniformly distributed in the sample volume, which leads to the determination of a uniform spin density (n_s) by dividing the total spin number by the sample volume. More so, One can assume that spins are uniformly distributed over the sample surface, where specific paramagnetic centers may be more likely to form, which leads to the determination of an areal spin density (α_s) by dividing the total spin number by the area of the sample surface, determined, for instance, by AFM. Both estimates require the determination of the sample spin number.

The reference system with known spin number used in our project is (2,2,6,6-tetramethylpiperidin-1-yl)oxidanyl (TEMPO). As TEMPO has a molecular weight of 156.25 a.m.u., Avogadro's law indicates that 156.25 μg of this radical compound, corresponding to 1 μmol , will contain a total of $N_T = 6.02 \cdot 10^{17}$ unpaired spins. The chemical structure of TEMPO is shown in Figure 2.13, along with its ESR spectrum that is formed by three equally spaced and equally intense narrow resonance lines, easily distinguishable from the signal of all of our samples. The three peaks of TEMPO are due to nitrogen nucleus (odd, odd proton and neutron spins) aligning in 3 configurations. As TEMPO is very soluble in alcohols, the desired concentration leading to a TEMPO signal comparable to the sample signal can easily be obtained.

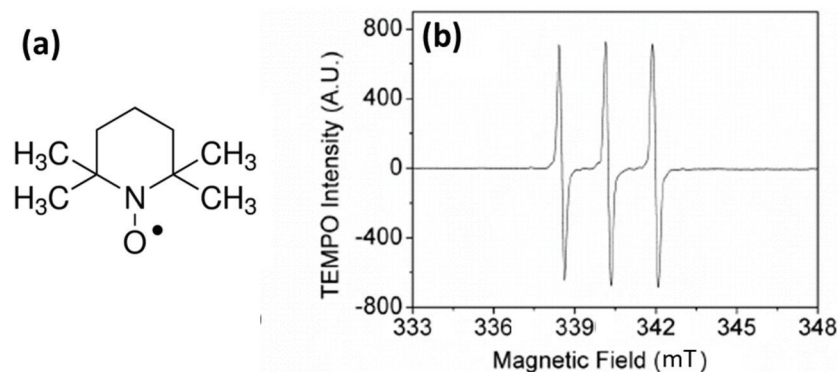


Figure 2.13: (a) Chemical structure of TEMPO; and (b) ESR spectrum of TEMPO formed by three equally intense resonance lines due to hyperfine splitting from nuclear spins of nitrogen [46] Adapted by permission from Begell House Inc. Copyright (2011).

Both in TEMPO and NiO_x, the signal area can be obtained either numerically, from a double integration of the ESR spectrum $I(B)$, or analytically by multiplying the peak-to-peak intensity ($I_{pp,j}$) by the peak-to-peak linewidth ($\delta B_{pp,j}$) of the spectra, which all have a Lorentzian line shape:

$$A_j = \int_0^{\infty} \int_0^B I(B') dB' \approx \begin{cases} 3I_{pp,T} \delta B_{pp,T} & \text{for } j = \text{TEMPO} \\ I_{pp,s} \delta B_{pp,s} & \text{for } j = \text{NiO}_x \end{cases} \quad (2.14)$$

Once A_{TEMPO} and A_s are determined from equation (2.14), the spin number in the sample can be determined from a simple proportion:

$$N_s = N_T \cdot \frac{A_s}{I_{M,s}} \cdot \frac{I_{M,T}}{A_T} \quad (2.15)$$

where $I_{M,s}$ and $I_{M,T}$ represent the intensity of the ESR signal from the marker when recorded, respectively, with the NiO_x sample and with TEMPO in the cavity. In this way, the spin density and the areal spin density of our NiO_x thin films are calculated.

A g -factor (also called g value or dimensionless magnetic moment) is a dimensionless quantity that characterizes the magnetic moment and gyromagnetic ratio of an atom, a particle or nucleus. The g -factor helps to distinguish and identify types of samples. Metal ions have very different g -factors. For example, the g -factor of an experimental ESR spectrum was determined as follows:

2.7 UV-Visible spectrophotometry

UV-visible absorption spectroscopy investigates the absorption due to interband transitions in the UV- visible photon energy region. A major assumption of our measurements is that the optical absorption of our samples mainly affects their transmittance, which is substantiated by the fact that, normally, TCO thin films are weakly reflecting. UV-VIS transmittance of our samples was measured at normal incidence in a range of wavelengths between 350 nm and 800 nm by an automated Varian DMS80 spectrophotometer. A

schematic diagram of the main components of a spectrophotometer is shown in Figure 2.14. The tungsten filament lamp is the source of visible and near infrared radiation. The light source from the lamp is passed to the rotating beam splitter through a monochromator. Radiation of only a wavelength leaves the monochromator. Part of the light from the beam splitter serves as the reference beam while the second part serves as a sample beam. The instrument records directly the transmittance of a test sample by measuring the percentage of the light that pass through the sample relative to that of the reference beam at specific wavelength. The transmittance of a sample is the ratio of the intensity of the light that emerges from the sample to the intensity of the light incident on it:

$$T = \frac{I}{I_o}. \quad (2.16)$$

UV-visible transmittance spectroscopy measurements are referenced by simultaneously scanning two bare substrates, identical to the substrate on which the film is deposited, in the range of wavelength selected. An identical measurement is carried out with the thin film sample placed on the sample holder while the reference substrate remains in the reference holder. The transmittance data of our samples were obtained at a step scan of 10 nm per second in a range of wavelength between 350 nm and 800 nm.

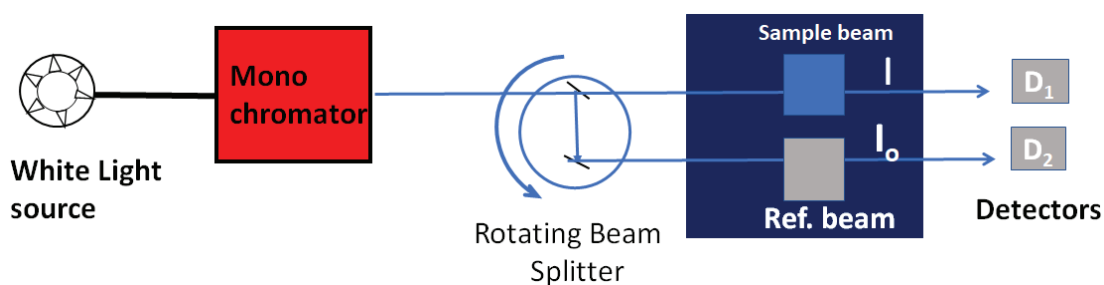


Figure 2.14: Schematic diagram of a double-beam spectrophotometer. The monochromator ensures that the sample is scanned continuously over a range of wavelengths at a pre-set scan rate.

2.8 Conclusion

In this chapter, I described the experimental details and different characterization techniques of nickel oxide thin film and powder samples. Nanostructured NiO_x was deposited by a solution growth method that is based on the formation of solid phase from a solution that involves two steps namely nucleation and particle growth. The samples were all annealed at different temperatures ranging from 225°C to 500°C and were characterized by the following techniques; ESR spectroscopy, AFM, UV-Visible spectroscopy, XRD and electrical conductivity measurement performed using two-point probe current-voltage at different annealing temperatures. Hence, the results of the measurements will be shown and discussed in Chapter 3 of this thesis.

2.9 References

- [1] W. Boyd, *J. Ceramics Int.* **22**, 429-434 (1996).
- [2] A. L. Olga, T. S. Nair, P. K. Nair, *J. Semi. Technol.* **12**, 1323-1330. (1997).
- [3] D. P. Padiyan, A. Marikani and K. R. Murali, *J. Mater. Chem. Phys.*, **78**, 51-58 (2002).
- [4] F. I. Ezema, S. C. Ezugwu, P. U. Asogwa, A. B. C. Ekwealor and R. U. Osuji, *J. Opto. and Adv. Mat.*, **5**, 747-750 (2010).
- [5] D. S. Dhawale, S. S. Lathe, K. Y. Rajpure and C. D. Lokhande, *J. Appl. Surf. Sci.*, **254**, 3269-3273 (2008).
- [6] D. Kołodyńska, *J. Environ Sci Pollut Res Int*; **20**, 5939–5949 (2013).
- [7] M. A. Vidales-Hurtado, A. Mendoza-Galvan, *J. Mat. Chem. and Phys.*, **107** 33 -38 (2008).
- [8] S. H. Lin, F. R. Chen and J. J. Kai, *J. Appl. sur. Sci.*, **254**, 2017-2022 (2008).
- [9] S.V Green, M. Watanabe, N. oka, G. Niklasson, C.G Granqvist and Y. Shigesato, *J.*

- Thin Solid Film, **520**, 3839-3842 (2008).
- [10] M. Ristova, J. Velevska and M. Ristov, *J. Sol. Energy Mater. Sol. Cells*, **71**, 219 (2002).
- [11] S.C Ezugwu, F.I Ezema and P.U. Asogwa, *J. Chalco. Letts.*, **75**, 341-348 (2009).
- [12] M. L. Breen, J. T. Woodward, D. K. Schatz and A. W. Apblett, *J. Chem. of Mats.*, **10** 710-717 (1998).
- [13] D. Lincot and R. Ortega Borges, *J. Electrochem. Society*, **139**, 1880-1889 (1992).
- [14] W. B. Zhang, N. Yu, W. Y. Yu and B. Y. Tang, *J. Eur. Phys.* **64**, 153–158 (2008).
- [15] G. Hodes, *Chemical Solution Deposition of Semiconductor Films*, Marcek Dekker, Inc., New York, Basel, (2003).
- [16] M. Wu, H. H. Hsieh, *J. Electrochemica Acta* **53**, 3427–3435 (2008).
- [17] S. M. Pawar, B. S. Pawar, J. H. Kim, O. Joo and C. D. Lokhande *J. Appl. Phys.*, **11**, 117-161 (2011).
- [18] G.F. Liptrot, *Modern inorganic chemistry*, Society/Unwin Hyman, London (1989).
- [19] J. M Dona, and J. Herrero *J. Electrochemical Society*, (2008).
- [20] M. Tadic, D. Nikolic, M. Panjan G. R. Blake, *J. of Alloys and Compounds*, **647**, 1061- 1068 (2015).
- [21] A. Begum, A. Hussain and A. Rahman, *J. Nanotechnology* **3**, 438 -443 (2012).
- [22] A. Castillo, F. S. Aguirre-Tostado, A. Salas-Villasenor, I. Mejia, B. Egnade, M. Sotelo-Lerma and M. A. Quevedo-Lopez, *J. Chalco. Letters*, **10**, 105-111, (2013).
- [23] [K. Govender, D. S. Boyle, P. B. Kenway and P. O. Brien, *J. Mater. Chem.*, **14**, 2575- 2591, (2004).
- [24] S. H. Lin, F. R. Chen and J. J. Kai, *J. Applied sur. Sci.* 254 -2022 (2017).

- [25] R. Zhai, R. Wang, H. Wang, M. Zhu and H. Yen, *J. Phys. D. Appl. Phys.*, **40**, 4039-4042 (2007).
- [26] S. Seghaier, N. Kamoun, R. Brini and A. B. Amara, *J. Mater. Chem. and Phys.* 97 71-80 (2006).
- [27] A. Begum, A. Hussain and A. Rahman, *Arab J. Sci. Engr.* **38**, 163-168 (2013).
- [28] A. U. Ubale, A. R. Junghare, N. A. Wadibhasme, A. S. Daryapurkar, R. B. Mankar and V. S. Sangawar, *Turk J. Phys*, **31**, 279–286 (2007).
- [29] K. L. Chopra and S. R. Das, *Thin film Solar Cells*, Plenum Press, New York (1983).
- [30] R. E. Dinnebier and S J. L. Billinge, *Principles of Powder Diffraction*. Royal Society of Chemistry. (2008)
- [31] B. von, Y. Waseda, E. Matsubara, K. Shinoda, *X-Ray Diffraction Crystallography Introduction, Examples and Solved Problems Auflage*, (2011).
- [32] S. H. Simon, *The Oxford Solid State Basics*. of Oxford of University (2013).
- [33] A. Blake, *Crystal Structure Analysis: Principles and Practice*, Oxford University Press, 2001.
- [34] P. Eaton, P. West, *Atomic Force microscopy* Oxford University Press, (2010).
- [35] F. Sharifi, *kelvin probe force microscopy on graphene thin films for solar cell and bio sensing applications*. The School of Graduate and Postdoctoral Studies Western University Canada (2014).
- [36] R. Garcia, Dynamic atomic force microscopy methods. *Surface Science Reports* **47**, (6-8), 197-301 (2002),
- [37] I. Sugiyama¹, N. Shibata, Z. Wang Zhongchang Wang S. Kobayashi, T. Yamamoto and Y. Ikuhara, *J. Nature Nanotech.* **45**, 2013.
- [38] D. Passeri¹ C. Dong, M. Reggente, F. De, and A. Fiorenzo, *Biomatter* 4, 29507 J. Landes Bio science (2014).

- [39] D. Rugar, H. J. Mamin, P. Guethner, S. E. Lambert Citation: *J. Appl. Phys.*, **68**, 1169 (1990).
- [40] A. Lund, M. Shiotani and S. Shimada, *Principles and Applications of ESR Spectroscopy* Springer (2010).
- [41] E. Duin, *Electron Paramagnetic Resonance Theory*. Word press, (2008).
- [42] G. R. Eaton, I. S. Sandra, D. P Eaton and T. Ralph, *Quantitative EPR* Weber Springer Wien New York Springe Quantitative EPR 2010.
- [43] D. M. Murphy, *Electron Paramagnetic Resonance Spectroscopy of Polycrystalline Oxide Systems*, Wiley Online Library (2013).
- [44] J. Weil, *Electron paramagnetic resonance Elementary Theory and Practical Applications*, (2007).
- [45] M. A. Tamskia, W. M. Dale, B. G. Breeze, J. V. Marpherson, P.R. Unwin, M. E. Newton, *J. Electrochimica Acta* **213** 802–810 (2016).
- [46] R. Wang, H. Zhou, P. Sun, H. Wu, J. Pan, W. Zhu, J. Zhang, and J. Fang, *J. Plasma Medicine*, **1**, 143–155 (2011).

Chapter 3

Properties of Nanostructured NiO_x fabricated from chemical bath deposition method

In this chapter, I will present the results of the measurements I performed on nanostructured NiO_x thin films. These results include the morphological, compositional and structural properties, as well as the electrical and paramagnetic properties of nanostructured NiO_x thin films deposited by solution-growth method. Although, there are a number of parametric studies that can be performed to enhance the properties of chemically deposited thin films, the change in post-deposition thermal annealing plays a significant role to tailor the properties of NiO_x thin films to a specific end. After careful optimization of the deposition conditions, such as the time to achieve a uniform film fixed at 16 hours, the concentration of the precursors, solution temperature that was maintained at 70°C and pH of 12.0-12.5, I varied only the annealing temperature of the deposited thin films. Consequently, in Section 3.1, I will discuss the morphological evolution of thin film of NiO_x as function of the annealing temperatures. The results of crystal phase identification using XRD and crystal size obtained with Debye-Scherrer's classical formula will also be presented. Section 3.2 is comprised of current-voltages characteristics and the transport properties of samples of NiO_x thin films annealed at different temperatures.

The results of the electron spin resonance (ESR) and magnetic force microscopy studies are presented in Sections 3.3 and 3.4, respectively. In these sections, the electrical conductivity in nanostructured NiO_x thin films is correlated to the paramagnetic defect density extracted from ESR. Two types of ESR-active centers are identified and assigned, respectively, to localized paramagnetic defects and surface electronic states.

3.1 Structural properties of nanostructured NiO_x thin films

3.1.1 Morphology and thickness

The AFM topography images of NiO_x thin films annealed at 300 °C to 500 °C are shown in Figure 3.1. The morphology of the samples shows that the grains of NiO_x thin films increased in size, which can be attributed to nucleation and coalescence of nickel oxide particles and islands with annealing temperature. In thin-films technology, high temperature thermal annealing tends to favour particle migration and coalescence which can result to changes in the overall morphology of the film [1]. For the NiO_x thin films fabricated in this work, the AFM images show that the sample annealed at 300°C has a spherical-like surface structure with an average diameter of 100 nm. At this annealing temperature, the deposited sample is composed of a mixture of NiO_x and Ni(OH)₂ because only at a higher annealing temperature is Ni(OH)₂ completely transformed to NiO_x [2]. It can be observed from panel (b) of Figure 3.1 that at 400 °C, the nickel oxide sample is transformed to needle-like nanostructure with a corresponding decrease in surface area density height. With a further increase in annealing temperature, the morphological structure changes from needle-like NiO_x nanostructured to nanobelts and microbelts structure at 450 °C. Besides the morphological transformation, the film annealed at 500 °C also exhibits higher porosity but interconnected nanobelt-like structures as witnessed in panel (e) of Figure 3.1. Significantly, changes in morphology of our sample could affect the electrical and transport properties of our NiO_x sample, and this will be explored in more details in Section 3.2.

To estimate the thickness of NiO_x thin films at different annealing temperatures, I performed contact-mode AFM scanning on a step between the samples and their substrates. The step height was created during the fabrication of NiO_x thin film using a Kapton tape to mask a portion of the substrate. After thin film deposition, the tape is lifted and taken off to reveal the step height. A 30 μm by 30 μm contact-mode AFM scan was subsequently carried out to determine the height, which ultimately gives the thickness of the thin films. Panels (a) and (b) of Figure 3.2 are the topography image and line profile of the scan performed on the NiO_x sample annealed at 450 °C. Panel (c) shows that the thickness of

the samples determined from the line profile of the scan decreases with increasing annealing temperature. Accurate knowledge of the thickness of the samples is required to determine other interesting properties of NiO_x thin films, such as the electrical conductivity that is the subject of Section 3.2.

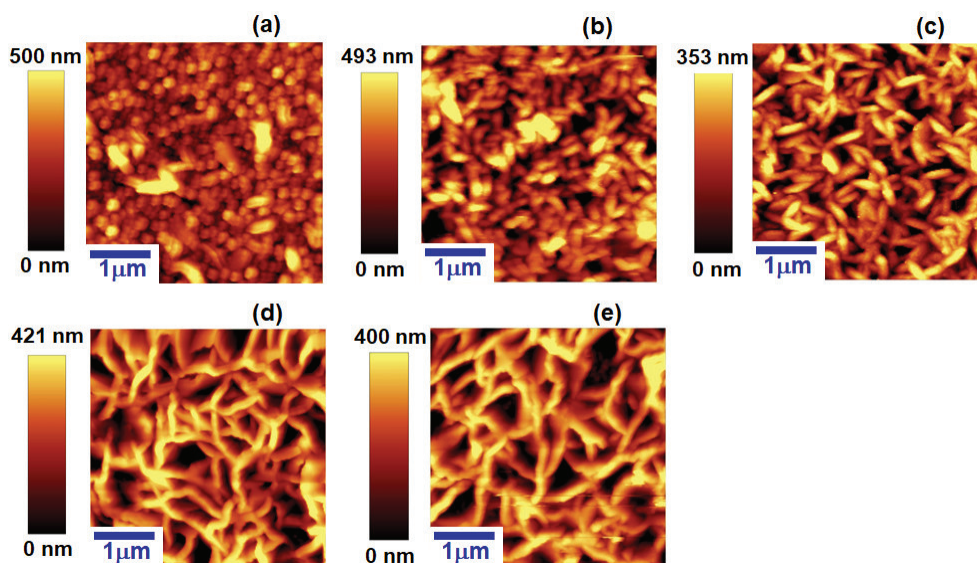


Figure 3.1: AFM topography images of nanostructured NiO_x thin films annealed at different temperatures of (a) 300°C, (b) 350°C, (c) 400°C, (d) 450°C and (e) 500°C. Images show films with different grain sizes and morphologies: spherical, needle-like, as well as nanobelts and microbelts at increasing annealing temperature.

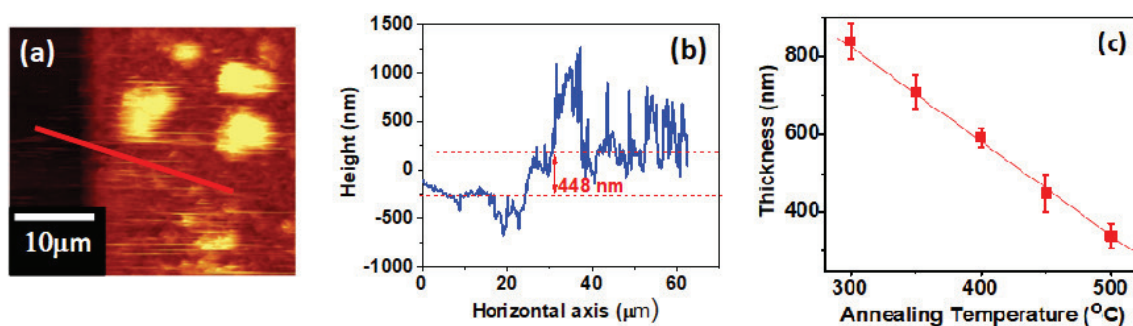


Figure 3.2: (a) Contact mode AFM image of NiO_x thin film used to determine the thicknesses, (b) profile of the line drawn along the substrate-sample interface (red line in (a)). The height of the gap from substrate to sample in the line profile gives the required thickness of the sample, and (c) variation of the thickness of NiO_x thin films with annealing temperatures.

3.1.2 SEM / EDX analysis of NiO_x thin films

The composition of NiO_x thin films fabricated by solution-growth method was investigated using a LEO (Zeiss) 1530 field emission microscope operating at 5-kV electron acceleration voltage. A scanning electron microscope (SEM) image, showing a morphology similar to the AFM images was acquired prior to energy dispersive X-ray (EDX) analysis is presented in Figure 3.3(a). This image shows that the NiO_x samples deposited in this work are generally uniform with only a few clusters of overgrowth. This is particularly significant for application of these materials as transparent electrodes in devices, such as solar cells and LED, in which structural defects constitute undesirable channels for charge recombination and energy losses [3].

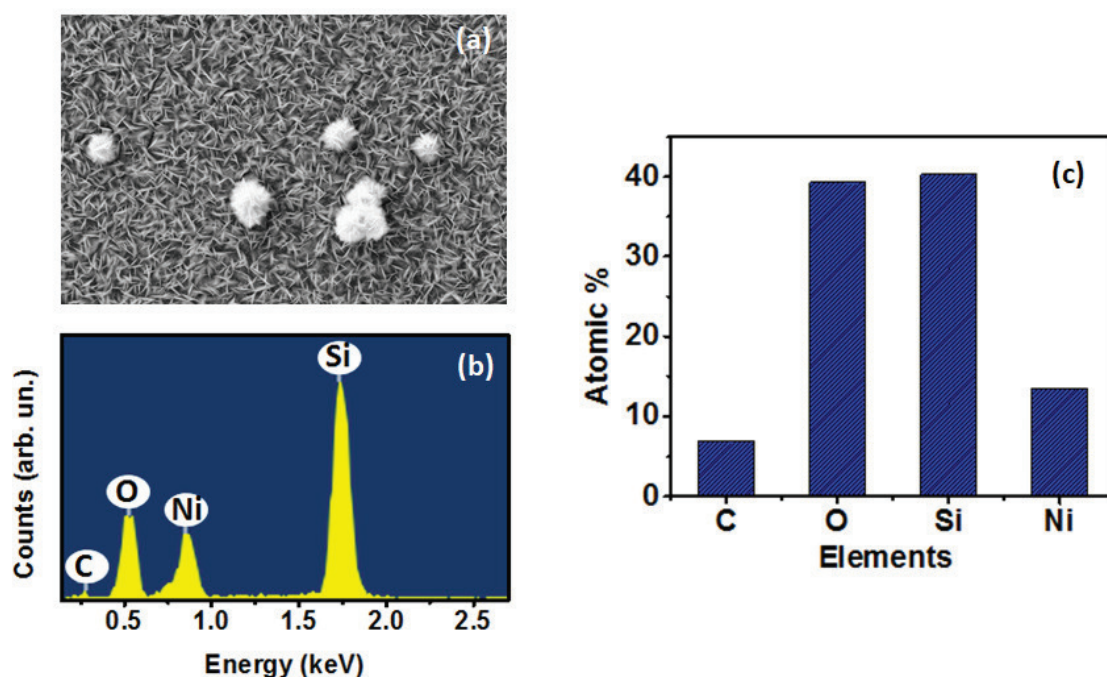


Figure 3.3: (a) SEM image of NiO_x thin films obtained using LEO (Zeiss) 1530 field emission microscope shortly before EDX spectra were acquired. (b) EDX spectra showing the composition of NiO_x thin films annealed at 400 °C for 1 h in air and (c) a histogram of the elemental composition from panels (b). Si is from the silicon substrate used to deposit the sample, C is impurity in trace amount.

The energy dispersive X-ray (EDX) spectra and a histogram of the elemental composition of NiO_x sample deposited on a silicon substrate and annealed at 400 °C in air is displayed in Figure 3.3, panel (b) and (c), respectively. Except for the Si from the substrate and traces of C, only the peaks of Ni and O appeared in the spectra, as expected. This is a confirmation level of the purity of NiO_x thin films that can be fabricated by inexpensive, easy to use solution growth method. As we now know how to tune the morphology and the thickness and have confirmed the composition of our samples, next I explored the crystal structure of these samples using phase identification of XRD.

3.1.3 Crystal structure of NiO_x thin films deposited from solution growth method

Figure 3.4(a) gives the x-ray diffraction pattern of nanostructured NiO_x samples under different annealing conditions and the as-grown sample. The diffraction peaks positioned at 2θ of 37.0°, 43.3°, 63.2°, 76.4°, 80.3°, 95.2° and 107.4° are indexed as (111), (200), (220), (311), and (222), (400), (331) crystallographic planes of NiO_x. All the peaks reflection displays face-centered cubic (FCC) nickel oxide structure. The as-grown sample fabricated using solution-growth method is comprised mostly of the hydroxide component of nickel (Ni(OH)₂) and is known to decompose and convert to pure NiO_x when subjected to thermal annealing [2]. The lower the temperature at which the sample can be completely converted to NiO_x the better, especially for applications in flexible devices requiring polymer substrates such as polyethylene terephthalate (PET), which decompose above 350 °C [4]. It can be observed in Figure 3.4 (a) that at 300 °C and above, the (001) crystal plane disappears, indicating that the mixture of NiO:Ni(OH)₂ phases are converted to NiO_x nanostructure, an improvement to previously observed onset of Ni(OH)₂ conversion at 400°C [5]. Figure 3.4 (a) also shows a progressive increase in the intensity of the XRD spectra, with the sample annealed at 450°C exhibiting the maximum intensity. Above this annealing temperature, the intensity starts to diminish. We can attribute this variation of the intensity of XRD spectra as indicative of conversion of Ni(OH)₂ to NiO_x with possible complete conversion and highest level of crystallinity at 450 °C annealing temperature. A further increase in the thermal annealing temperature tends to destroy the crystal structure of the sample as demonstrated by the reduced intensity of XRD spectra annealed at 500°C.

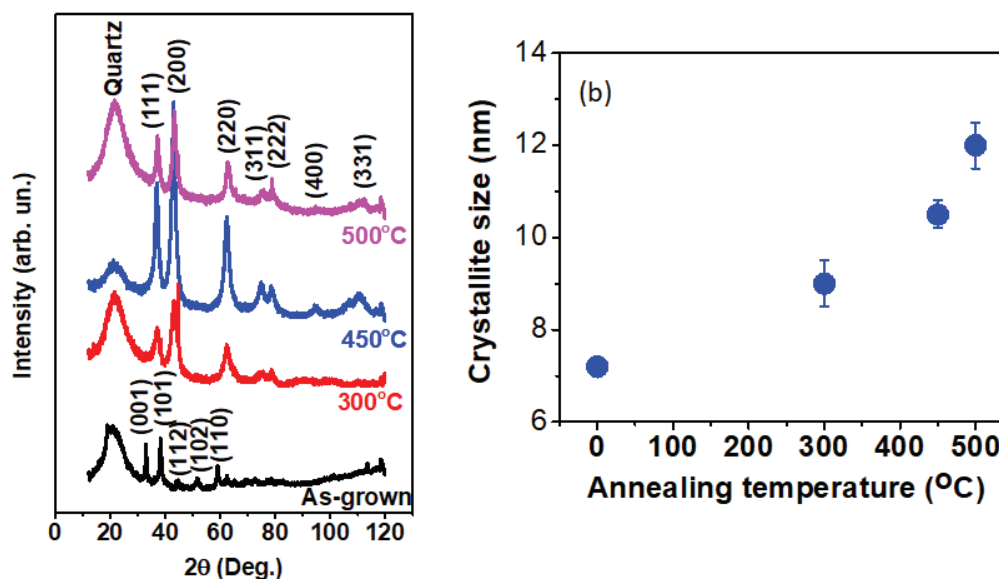


Figure 3.4: (a) X-ray diffraction patterns of NiO_x thin films annealed at different temperatures, showing a crystalline face-centered cubic (FCC) lattice; (b) variation of crystallite size of NiO_x thin films as a function of annealing temperature, determined from the XRD patterns using the Debye-Scherrer's relation (equation 3.1). It can be observed that the crystallite diameter increases at increasing annealing temperature.

The crystallite size of NiO_x was determined from the XRD profiles in Figure 3.3(a) using Debye-Scherrer's relation given as

$$D = 0.9\lambda / \beta \cos \theta \quad (3.1)$$

where λ is the wavelength (1.5418 Å), β is the full width at half maximum, θ is Bragg diffraction angle, and κ is a constant equivalently fixed at 0.9. The result of this calculation is presented in panel (b) of Figure 3.4, which shows that the crystalline size is increased with increasing annealing temperature of the nanostructured NiO_x thin films. The crystallite sizes of NiO_x obtained in this work were 7.2 nm, 9 nm, 10.5 nm and 12 nm for annealing temperature of 0°C, 300°C, 450°C and 500°C respectively. These crystallite results are close to the value of 9 nm for NiO:Cu nanoparticles reported by [6]. In addition, the result showed an exponential effect in temperature since nucleation theory is exponential in temperature. The annealing process not only increases the average crystallite

size, but it can also be used to introduce controlled defects required to induce electrical conductivity from insulating non-stoichiometric nickel oxides [6].

3.2 Electrical properties of NiO_x thin films

3.2.1 Electrical conductivity

The electrical conductivity of thermally annealed nanostructured NiO_x thin films was measured from I-V curves (Figure 3.5(a)) recorded on a Signatone S-725 probe station using a Keithley 2400 source meter. Voltages in the ±10 V range were applied in order to obtain the current – voltage curves from the configuration depicted in panel (b) of Figure 3.5. With this configuration, the electrical conductivity, σ , can be determined from the following relation

$$\sigma(\Omega^{-1}m^{-1}) = \frac{S \times w}{l \times t} \quad (3.2)$$

where S is the slope of the Ohmic I-V curves of Figure 3.5, (a), t is the thickness of NiO_x samples determined from the contact mode AFM scan (see Figure 3.2), l is the length of Al contact, and w is the gap or distance between neighboring contacts. The calculated electrical conductivity of nanostructured NiO_x thin films are presented as a function of the annealing temperatures in panel (c) of Figure 3.5.

From Figure 3.5(c), it can be observed that the electrical conductivity of solution processed NiO_x thin films slightly increases at increasing annealing temperature between 225°C and 350°C, then jumps and reaches maximum at 450°C and decreases with further increase in the annealing temperature to almost insulating at 500°C. Two significant changes are expected when solution-processed NiO_x are subjected to various level of thermal treatment. Firstly, heat treatment causes the decomposition of the hydroxide component to oxides (NiO_x) as the annealing temperatures are increased, and secondly, induces non-stoichiometry in the nickel oxide, thus make the sample electrically conducting [23]. Consistently with the XRD results presented earlier, an increase in thermal treatment of our chemically fabricated NiO_x in the temperature range of 300–450°C increases the

decomposition of the hydroxide component to oxides (NiO_x), and consequently induces the high electrical conductivity observed in Figure 3.5 (c). Similarly, the suppression of the electrical conductivity at the highest annealing temperature of 500°C can be attributed to low density of defects due to defect quenching at high temperatures [7] as will be demonstrated in Section 3.3.

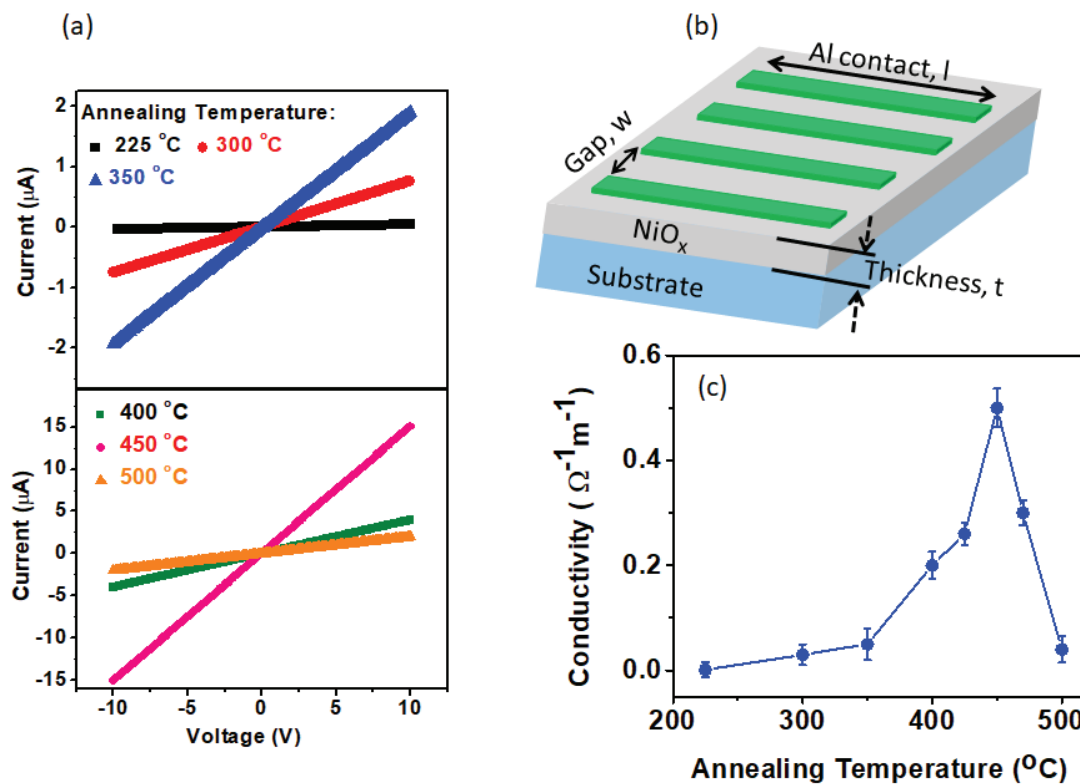


Figure 3.5: (a) Current–voltage characteristics of NiO_x thin films annealed at different temperatures. (b) Schematic of planar configuration used to measure the I–V curve of NiO_x thin films. (c) electrical conductivity versus annealing temperature of NiO_x thin film determined from the I–V characteristics. The conductivity is non-monotonic and peaked at 450°C .

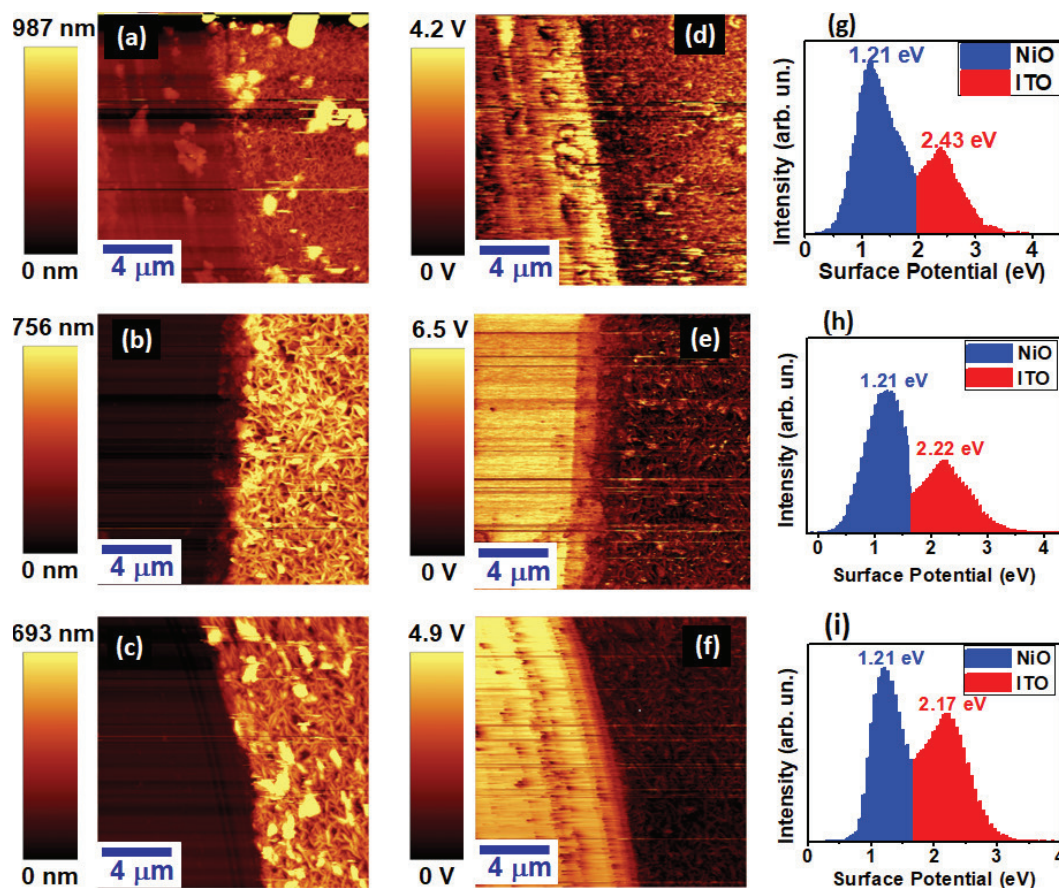


Figure 3.6: Leftmost column: AFM of NiO_x (right side of the images) and ITO substrate (left side) annealed at different temperatures: (a) 300°C; (b) 400°C; and (c) 450°C. Middle column: corresponding Kelvin probe force microscopy images at (d) 300°C, (e) 400°C and (f) 450°C. Rightmost column: work function histograms obtained from the KPFM images at (g) 300°C, (h) 400°C and (i) 450°C.

3.2.2 Work function of nanostructured NiO_x thin films

To gain further insight to the suitability of our NiO_x samples for application in solar cells and other opto-electronic based devices, we measured the work function of the samples using Kelvin probe force microscopy (KPFM) technique [8-9]. With this technique, the work function of a sample can be accurately determined from the surface potential images of a KPFM scan performed on a sample in the proximity of a material whose work function is known. Both AFM and KPFM images are simultaneously recorded during the measurements. Figure 3.6 shows the AFM topography (left images) and the corresponding

surface potential (right images) of nanostructured NiO_x thin films performed in the proximity of ITO substrate after different thermal treatment. The histogram of the surface potential is shown in panels (g), (h) and (i) for samples annealed at 300°C , 400°C and 450°C , respectively.

The surface potential image is indicative of the potential difference between the KPFM tip and the samples (in this case ITO substrate and NiO_x thin film) due to differences in their energy level (work function and Fermi energy). Since an electrostatic force exists whenever potential difference exists between two objects, corresponding to differences in their work function, the KPFM images show a gradual decrease in the value of surface potential as the annealing temperature increases indicate the variation of work function with thermal annealing in chemically processed NiO_x thin films. To confirm the visual observation, we calculated the work function of our samples using ITO work function of 4.5 eV as the calibrating factor. The result is presented in Figure 3.7, panel (a) and consistent with the visual observation, the work function of NiO_x thin films decreases with the annealing temperature.

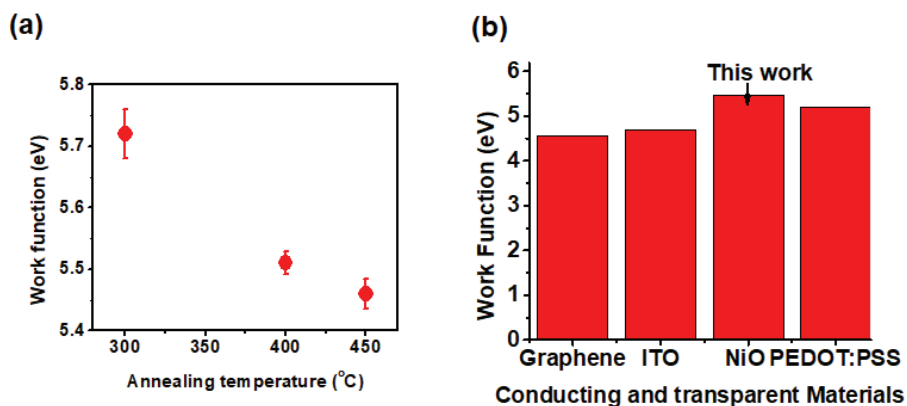


Figure 3.7: (a) Variation of the work function of NiO_x thin films with the annealing temperature and (b) histogram of the work function of transparent conducting thin films frequently used in optoelectronic devices, including our NiO_x thin film annealed at 450°C . The work function of the NiO_x thin film is very close to the work function of PEDOT:PSS.

Figure 3.7, panel (b), compares the work function of frequently used transparent conducting electrodes, also including PEDOT:PSS used as a hole transport layer in bulk heterojunction solar cells and a NiO_x thin film fabricated in this work. The result shows that the work function of our sample is closer to the work function of PEDOT:PSS than those of ITO and graphene. Consequently, the NiO_x thin films can serve as possible replacement for PEDOT:PSS in heterojunction solar cell devices to circumvent most of the problems associated with PEDOT:PSS, such as degradation and high electrical resistivity. Also, due to good energy level matching, a NiO_x thin film annealed at 450°C may possibly serve as a cathode material, replacing ITO [10] and graphene [3].

3.3 Electron spin resonance

In this Section, we present the ESR investigation of both powder and thin-film samples of nanostructured NiO_x . The objective is to gain insight into the specific magnetic centers that may be responsible for the electrical conductivity of this material. Although stoichiometric NiO is antiferromagnetic, we anticipate that an intense ESR signal is present in all of our samples, and contains the signature of two distinct types of magnetic centers. We will attempt at correlating the electrical conductivity of our samples with the concentration of either type of magnetic centers. In addition, special emphasis will be placed on understanding the origin of the two types of magnetic centers from specific sample region, in the crystalline bulk or at the surface of the grain boundaries.

3.3.1 Origin of magnetic centers in NiO_x from ESR powder spectra

To understand the origin of the two types of paramagnetic centers, NiO_x powder was synthesized, as discussed in Chapter 2, and measured by ESR. Powder samples with two distinct grain sizes were prepared, and the results are shown in Figure 3.8. Panel (a) shows the ESR spectra from fine grains. These grains have been grinded in a mortar and were sieved through a stainless-steel mesh of $130\text{-}\mu\text{m}$ mesh size. The small size of the grains has been confirmed using an optical microscope. It can be observed that two ESR signals (A and B) are present in these samples. Signal A is very narrow, indicating very long spin-spin relaxation time T_2 . In conduction electrons, long T_2 is normally indicative [11] of long charge carrier relaxation times and good transport properties. If transport occurred through

this type of defects, this would anticipate an efficient hopping transport mechanism. A zoom of Signal A is shown in panel (b). It can also be observed from panel (c) that the signal intensity increases linearly with the mass of powder being measured, which is consistent with the fact that paramagnetic center type A originates from the bulk of the sample as it is proportional to its mass and volume.

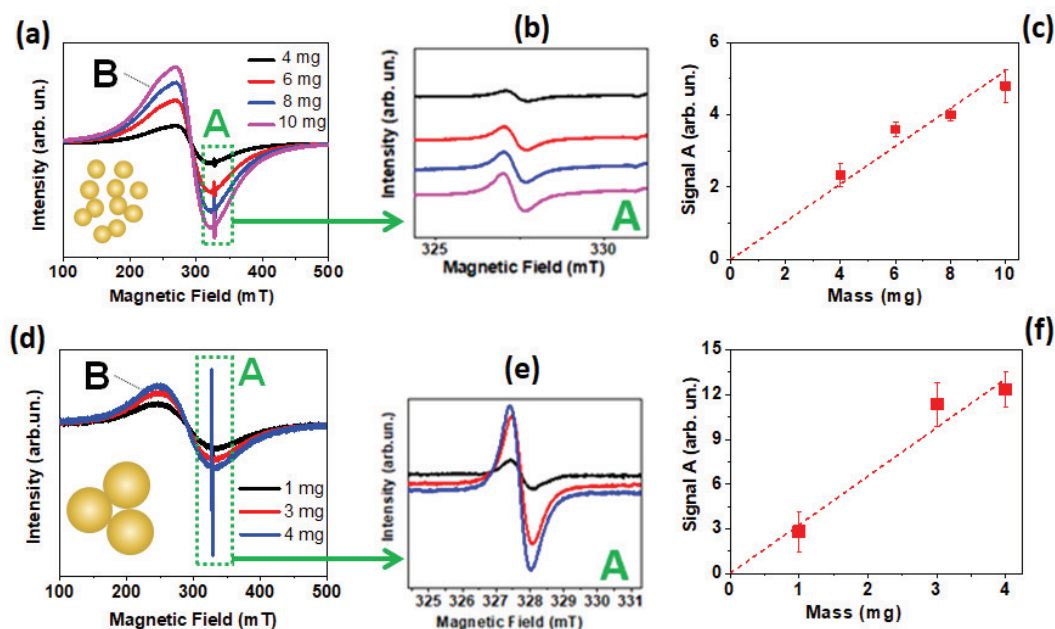


Figure 3.8: (a) NiO_x powder ESR spectra at room temperature from fine grains, less than 130 μm , and measured quantities from 4 mg to 10 mg; (b) zoom of “A” signal recorded from the same sample; (c) direct proportionality between the double-integrated intensity of “A” signal and the sample mass, suggesting that signal “A” comes from defects in the grain bulk; (d) NiO_x powder spectra at room temperature from coarse grains of 1.2 ± 0.2 mm diameter, exhibiting a significantly lower intensity of signal “B” over signal “A” due to the lower amount of surfaces; (e) zoom of “A” signal showing comparable line widths with panel b; and (f) signal intensity as a function of mass. Both samples were annealed at 450 $^{\circ}\text{C}$.

Panel (d) shows the ESR spectra from coarse grains, as obtained from the synthesis process. The same two ESR signals as before, A and B, are also present in this sample. However, the ratio between signal B and signal A is significantly smaller than in the previous sample.

As this sample contains a lower density of surfaces per unit volume, due to the larger size of the grains, we assign signal B to defects relating to the surface of the grains. On the one hand, panels (e) and (f) show that, also in this second sample, signal A is proportional to the measured mass and volume of powder; on the other hand, it is immediate from panel (d) that signal B grows at a significantly lower rate with the measured quantity of powder. This confirms that signal B may be a surface-related signal, as also witnessed by its non-isotropic line width. Further evidence of and insight into these assignments will be presented in the next sections.

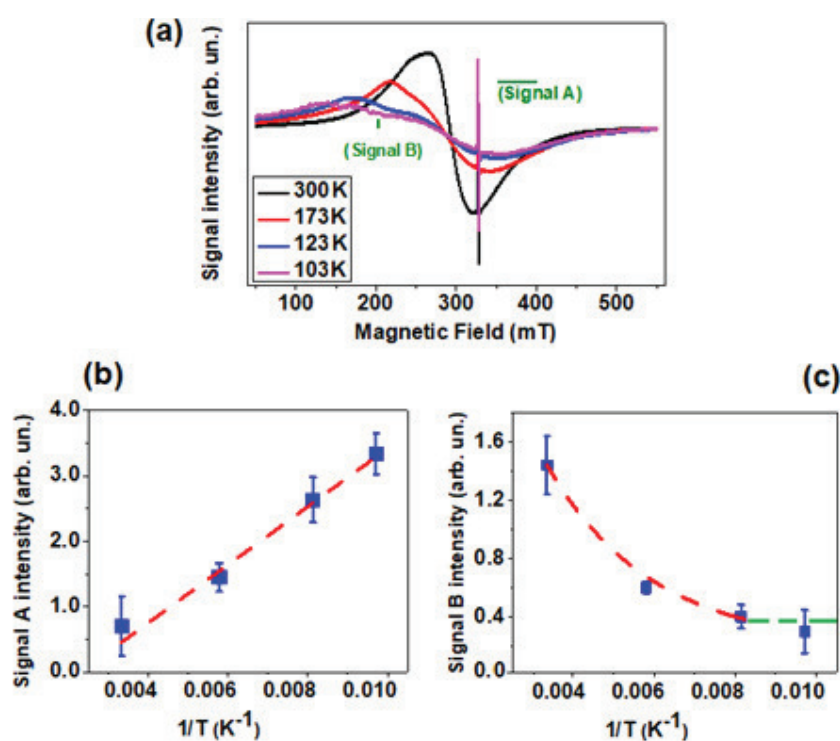


Figure 3.9: (a) ESR signal intensity of fine-grain NiO_x powder sample as a function of temperature, consisting of two observed signals A and B. Signal B becomes progressively broader, anisotropic, and surface-related at lower temperature; (b) Curie plot for the intensity of signal A, strongly suggesting that it originates from localized states; and (c) intensity of signal B as a function of inverse temperature, showing neither Curie nor Pauli paramagnetism, but becoming constant below 120°K – a temperature that we identify as the Neel temperature below which signal B becomes constant, anisotropic, and likely confined in the proximity of the surface.

3.3.2 ESR signal at varying measuring temperature

The ESR spectra of fine-grain NiO_x powder at temperatures from 102 K to 300 K are shown in Figure 3.9. Both signal A and signal B are present at all of the investigated temperatures. At 300 K, signal B is nearly isotropic, but the intensity of signal B appeared deformed, and broadening towards higher g-values as the measurement temperature decreases. The signal becomes fairly constant below about 120°K, after the signal intensity has significantly diminished with temperature, a trend not consistent with either Curie or Pauli paramagnetism [see equations (1.15) and (1.18)]. The significant signal anisotropy of the A signal at low temperature is consistent with spins localized at the surface, while the more isotropic signal at higher temperature is consistent with a signal extending towards the bulk. This is consistent with the fact that the bulk of the sample becomes antiferromagnetic at about 120°K – a temperature that we identify as the Neel temperature of our system, below which signal B becomes constant, anisotropic, and likely confined in the proximity of the surface. T_N is 523 K in ideal NiO crystals [12] but, as shown in Table 1.2, T_N is influenced by several factors such as crystallite size and shape, as well as defects and impurities

Panel (b) in Figure 3.9 shows the ESR intensity of signal A in a Curie plot, as a function of the reciprocal of the temperature. The linear trend as a function of T⁻¹ is an indication of Curie paramagnetism. If localized moments are responsible for the magnetization, Curie's law predicts that ESR signal is inversely proportional to temperature. [13]. Therefore, this result is in consistent with the assignment of signal A to point defects localized at specific lattice sites. Panel (c) in Figure 3.9 shows that signal B is associated to magnetic centers that do not show neither Curie nor Pauli paramagnetism, but becoming constant below 120°K – a temperature that we identify as the Neel temperature below which signal B becomes constant, anisotropic, and likely confined in the proximity of the surface. Bulk NiO exhibits a Neel temperature of 523 K [Rubinstein et al]. Nevertheless, the T_N is influenced by certain factors such as defects, impurities and crystallite sites, which may explain the significantly lower T_N exhibited by our system. Above T_N antiferromagnets become paramagnetic, with delocalized spins, which explain the significant increase in the density of paramagnetic centers at increasing temperature.

In conclusion, signal A can be associated with localized bulk states, while signal B can be associated with extended surface states at $T < T_N$ and, at $T > T_N$, these states tend to extend towards the bulk of the sample as the temperature increases. From this picture, both paramagnetic centers relating to signal A (which can be defects such as oxygen vacancies or Ni^{3+} centers) or magnetic systems relating to signal B (extended states at the surface or in the bulk of the material) may be responsible for the electrical transport in nickel oxide thin films. For example, if signal B were responsible for the electrical transport, a surface conductivity process at the grain boundary might be hypothesized in samples in which T_N is above room temperature. However, we will demonstrate in the next section that this is not the case. Irrespective of the fabrication conditions, a correlation exists between the intensity of signal A and the electrical conductivity of our samples.

3.3.3 Spin density versus annealing temperature in NiO_x thin films

The spin density and ESR signal intensity of nickel oxide thin film for the variation of annealing temperatures is shown in Figure 3.8. The results indicate two types of ESR-active centers (labelled as Signal A and B) are identified. The spin density in our samples was obtained from equation (2.15). Normally, the spin density account for the unpaired spins per volume of the sample. It is found that spin density increases with annealing temperature for signal A, up to 450°C , where conductivity seems to be maximum and gradually decreases with further increased in annealing temperature. A similar trend was observed for signal B with maximum conductivity at 425°C . Hence, the decrease in spin density with the increase in annealing temperature is noted to be region where defects densities due to vacancies are tremendously reduced. In this context, we are suggesting that signal A could be the localized bulk states owing to the fact that the vacancies in the material annealed out at further temperature of 450°C , unlike signal B with decreased vacancies at 425°C and maybe showing some extended surface states relating to antiferromagnetic below T_N . This will be discussed more extensively in the next section.

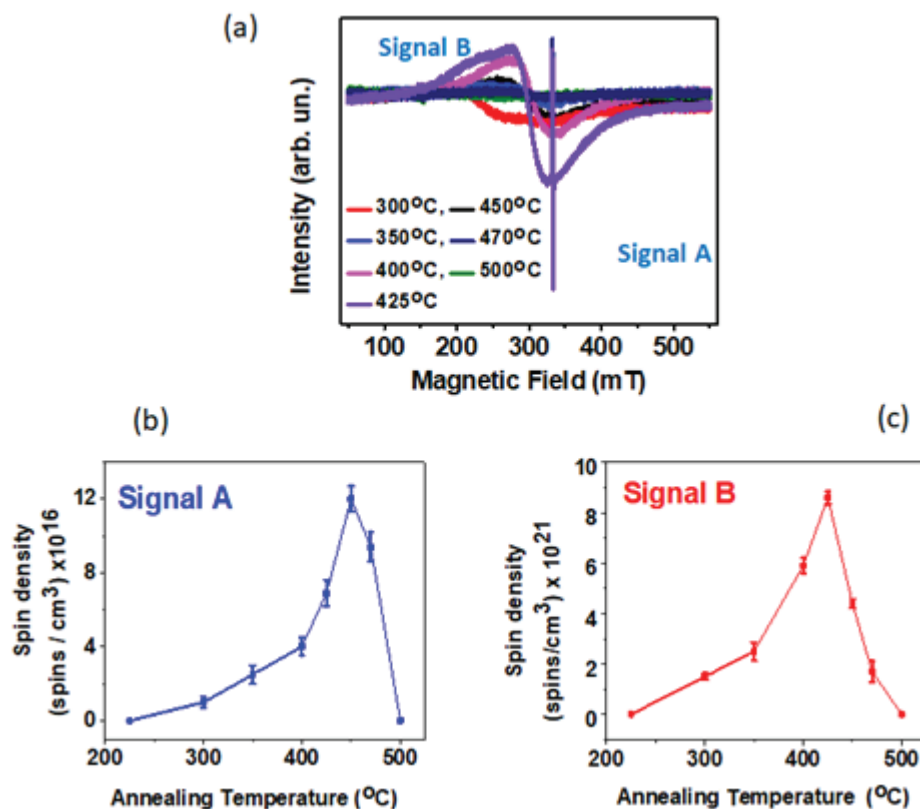


Figure 3.10: (a) The ESR signal intensities of signal A and signal B, (b) spin density of signal A from bulk grains and (c) spin density of signal B surface grains with different annealing temperature from (225 – 500) °C of NiO_x thin films.

3.3.4 Correlation between electrical conductivity and spin density

In order to investigate the predominant defects existing between the bulk and surface states which are associated respectively to signal A and signal B, I plotted the graph of spin density versus electrical conductivity shown in Figure 3.9. The results showed good linear relationship between the spin density of signal A and the electrical conductivity. On the contrary, no good relationship was found between Signal B corresponding to extended surface states. Therefore, conductivity must be related to signal A.

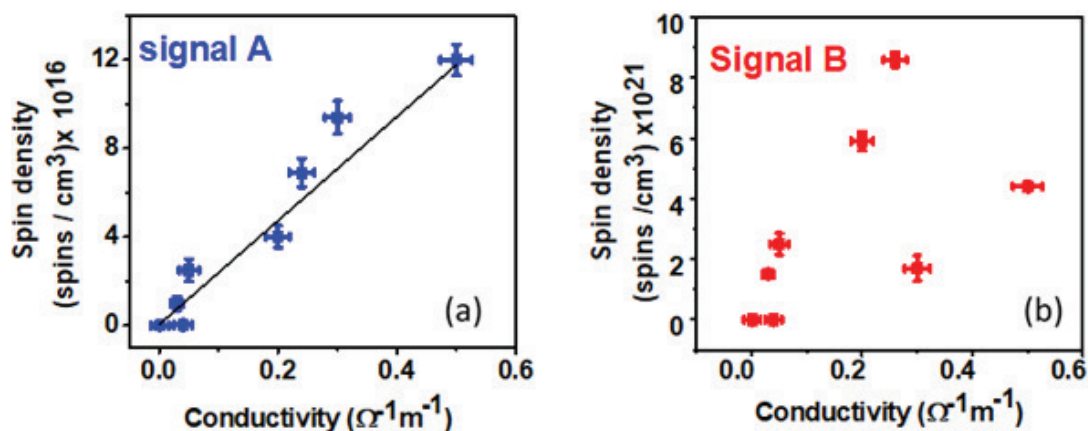


Figure 3.11: Electrical conductivity versus spin density of (a) signal A, (b) signal B. good linear relationship exist between the electrical conductivity and spin density of signal A related localized bulk states and contrarily, no correlation was found between Signal B related extended surface state.

Correlation between the electrical conductivity and bulk paramagnetic defects is further ascertained by temperature dependent ESR intensity measurement of signal A shown in Figure 3.9. This result indicates that electrons in solids are localized in the defects and with more engineered defects, electrons can hop from one defect to the other that will lead to enhanced conductivity in NiO_x thin film. Consequently, localized point defects associated to signal A contribute immensely to the electrical conductivity in NiO_x.

Published work by Kwom *et al.* [7] suggested that the electrical transport mechanism in non-stoichiometric nickel oxide films are technically due to point defects related to Ni³⁺ ions residing at the surface of the sample since X-ray photoelectron spectroscopy (XPS) and scanning ion mass spectra (SIMS) characterizations they used were all surface sensitive quantitative spectroscopy techniques that measure the elemental composition and electronic state that exist within a material. The results further showed that Ni³⁺ ions interstitial or oxygen vacancies are the dominant defects responsible for the enhanced electrical properties of nanostructured NiO_x prepared by RF magnetron sputtering [14] However, all these surface sensitive techniques mentioned here are geared towards surface studies as to understanding the origin of electrical conductivity due to point defects residing

at the surface of NiO_x thin-film, though with very limited insight to detailed bulk characterization technique such as ESR spectroscopy. XPS technique detects and assigns defect peaks on the samples and it could be attributed to surface defects but the detection of such defects was limited to a few surface studies, and no confirmation of such defects in the bulk of the samples was presented.

In other words, we verified if the point defects are due to the presence of Ni³⁺ ions centers as they would have the g-factor of 2.14 published by [6] which is not the case here because, in this thesis, the g-factor value from electron spin resonance signal was 2.008. Certainly cannot be Ni²⁺ ions centers because they would have g-factor of 2.022 as reported by [15]. So, we provisionally assign signal A, the bulk states to be responsible for the electrical conductivity in NiO_x. Thus, this finding emphasized that bulk paramagnetic centers due to oxygen vacancies are predominantly responsible for the observed electrical conductivity in non-stoichiometric NiO thin film with minimal contributions from signal B, the extended surface states.

To further confirm the existence of extended surface state residing at the surface of nickel oxide film, Madhul et al. [16] reported the core-shell model of the vacancy concentration and magnetic behaviour of NiO nanoparticle and by using X-ray absorption fine structured (XAFS) characteristics, it was shown that Ni²⁺ vacancies reside mostly on the surface and are responsible for the weak ferromagnetic surface in NiO nanoparticle. Additionally, madhu et al. reported the result obtained by X-ray absorption fine structured (XAFS) characteristics that confirm the presence of Ni²⁺ ions at the surface structure of NiO_x being ferromagnetism while O²⁻ vacancies is mostly at the core being the antiferromagnetic and this result is in consistent with our result except for the fact that signal A related to O²⁻ vacancies are bulk paramagnetic at the bulk, while signal B, related surface grains are antiferromagnetic at $T < T_N$ tending to the bulk at $T > T_N$.

3.4 Magnetic force microscopy (MFM) study of NiO_x films

Room-temperature MFM images are shown in Figure 2.12. From these images, it can be observed that the phase shift of MFM images is not significant in samples annealed at 300°C and 400°C, while it is very strong at 500°C annealing temperature. This indicates the existence of ferromagnetic surfaces in this sample. As far as ferromagnetic surfaces form when the bulk is antiferromagnetic, surface ferromagnetism indicates that the sample annealed at 450°C is below the Neel temperature at room temperature, i.e. $T < T_N$ while samples annealed at 300°C and 400°C possess a Neel temperature lower than room temperature, i.e. $T > T_N$. [17] Sugiyama *et al.* have studied the magnetic properties of crystalline NiO using MFM, and they noticed ferromagnetic dislocations at the surface. However, to the best of our knowledge, ours is the first MFM study of nanostructured and nonstoichiometric NiO_x. Our MFM results importantly confirmed that extended states residing at the surface, with behavior correlating with ESR signal B, are responsible for surface ferromagnetism and bulk antiferromagnetism in NiO_x thin films. These extended states do not seem to have any relationship with the electrical conductivity of the samples, which appears to be related to localized paramagnetic states in the bulk, persisting at any measuring temperature and exhibiting Curie-like behaviour.

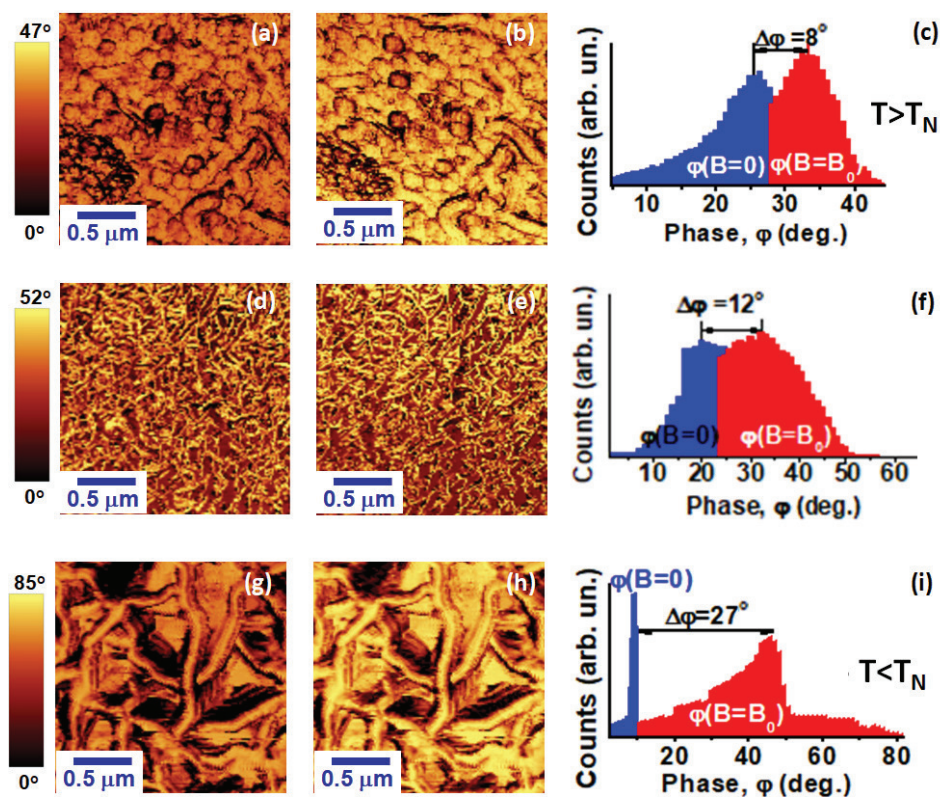


Figure 3.12: MFM phase images obtained by tapping mode AFM technique for nanostructured NiO_x thin films at three distinct annealing temperatures: (a) 300 °C scan with demagnetized tip and the corresponding (b) magnetized tip, and (c) histogram of the two scans to obtain the phase shift. (d) 400 °C scan with demagnetized tip and the correspondence (e) magnetized tip and (f) histogram of the phase profile from the two scans. (g) 450 °C scan with demagnetized tip and the corresponding (h) magnetized tip and (i) histogram of the two scans to obtain the phase shift.

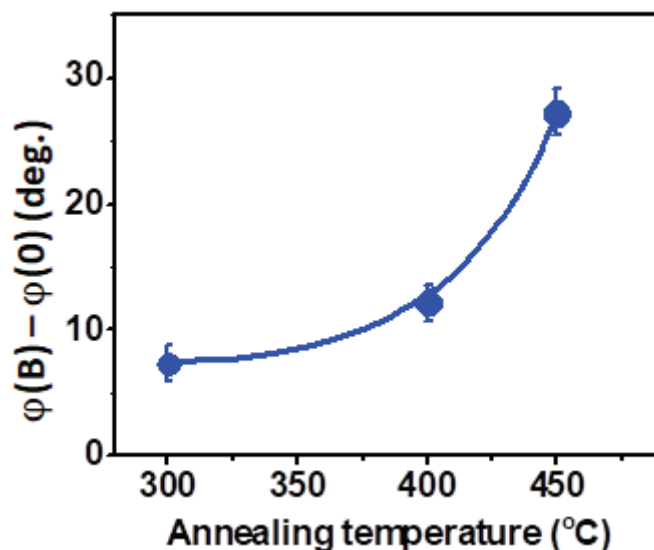


Figure 3.13: MFM phase shift in non-stoichiometric nickel oxide thin films. The reported phase corresponds to the average peak value in Figures 3.12 c, f, and I and is plotted as a function of annealing temperature. The increase in phase shift strongly suggests that the Neel temperature transitions from above room temperature to below room temperature at annealing temperatures about 400 °C.

3.5 Conclusion

The results of the measurements I performed on nanostructured NiO_x thin films are shown in Chapter 3 of my thesis. At temperature below the Neel temperature ($T < T_{\text{Neel}}$), the material is antiferromagnetic NiO at the bulk with the existing ferromagnetic (111) surfaces, while at temperature above the Neel temperature $T > T_{\text{Neel}}$, the material is paramagnetic bulk NiO_x thin-film related to ESR signal B. On the other hand, at any Neel temperature, ESR signal A is bulk paramagnetic associated to Oxygen vacancies and is responsible for the electrical conductivity.

Additionally, the annealing temperature of 300°C to 475°C, increases the grain size of NiO_x progressively and stabilizes the formation of vacancies while annealing temperature $> 475^\circ\text{C}$ leads to quenching of O^\cdot vacancies and electrical conductivity start to decrease.

3.6 References

- [1] M. Ohring, *The Material Science of Thin Films*, Academic Press, (1992).
- [2] M. Wu, H. H Hsieh, J. Electrochemica. Acta **53** 3427–3435, (2008).
- [3] K. X. Steirer, J. P. Chesin, N. E. Widjonarko, J. J. Berry, A. Miedaner, D. S. Ginley, D. C. Olson, J. Organic Electronics **11** 1414–1418, (2010).
- [4] F. Bensebaa J. Interfccc Sci. and Tech. (2013).
- [5] M. El-Kemari, N. Nagy, and I. El-Mechassed, 1747-1752 (2013).
- [6] P. Ravikumar, B. Kisan, A. Perumal, J. of Appl. Phys. Advances **5**, 087116 (2015)
- [7] Y. H. Kwon, S. H. Chun, J. H. Han, H. Koun Cho, J. Met. Mater. Int., **18**, 1003-1007 (2012).
- [8] F. Sharifi, *kelvin probe force microscopy on graphene thin films for solar cell and bio sensing applications*. The School of Graduate and Postdoctoral Studies Western University Canada (2014).
- [9] A. Akbari-Sharbaz, S. Ezugwu, M. S. Ahmed, M. G. Cottam and G. Fanchini. *Carbon* **61** 595 – 601(2015).
- [10] Y. Liu, Y. Li and H. Zeng, J. nanomaterials (2013).
- [11] A. Lund, M. Shiotani and S. Shimada, *Principles and Applications of ESR*
- [12] M. Rubinsteina, R. H. Kodamab, S. A. Makhlof J. of Magnetism and Magnetic Materials **234** (289–293 (2001).
- [13] Daid D. Jiles, introduction to Magnetism and Magnetic Materials, Chapman and hall, (1990).
- [14] J. Jeng, K. C. Chen, T. Y. Chiang, Pei-Ying Lin, Tzung-Da Tsai, Y. C. Chang, T. F. Guo, P. Chen, T. C. Wen, Y. J. Hsu, J. Adv. Mater, **26**, 4107–411, (2014).
- [15] R. Zamiri, H. A. Ahangar, A. Rebelo, G. Zamiri, and A. Zakaria, J. Chem Intermed 432881–2888(2017)
- [16] G. Madhu, K. Maniammala and V. Biju, Chem.Chem.Phys., **18**, 12135 (2016).
- [17] Sugiyama¹, N. Shibata, Z. Wang Zhongchang Wang³, S. Kobayashi, T. Yamamoto and Y. Ikuhara, J. Nature Nanotechnology **45**, 2013.

Chapter 4

Conclusions and Future work

4.1 Conclusions

In this thesis, I studied defects-induced electrical conductivity in nanostructured NiO_x thin films synthesized by solution growth technique and treated to different annealing temperatures in the range, 225 °C – 550 °C. We utilized suite techniques such as atomic force microscopy (AFM), Kelvin probe force microscopy (KPFM), electron spin resonance (ESR), X-ray diffraction technique (XRD) and two-probe method for characterizing these samples. The XRD pattern of NiO_x showed good crystalline face centered cubic structure at an optimal thermal annealing temperature of 450 °C. However, the as-grown samples comprised mostly of the hydroxides, Ni(OH)₂, which decomposed to pure NiO_x when subjected to thermal annealing at 300 °C and above. The result of AFM measurement showed that the NiO_x sample studied in this thesis work evolved through different morphologies with annealing temperatures, ranging from spherical, needle-like and nanobelts structures. The observed changes in the morphology of our samples was accompanied with changes in their electrical and transport properties.

The electrical conductivity of solution processed NiO_x thin films slightly increased lower annealing temperatures, between 225 °C and 350 °C. At the annealing temperature of 450 °C, the sample showed very large XRD profile peaks and a nanobelt-like structure, and also maximum electrical conductivity of $0.5 \pm 0.04 \text{ } \Omega^{-1}\text{m}^{-1}$. A further increase in the annealing temperature only resulted to a decrease in the electrical conductivity and at 500 °C, the sample became almost an insulator. The investigated electrical conductivity in these samples were correlated to the two paramagnetic environment obtained from electron spin resonance measurements. But before this, it will be pertinent to summarize the origin of the magnetic centers observed in our sample.

The two types of paramagnetic centers observed in our sample were investigated by measuring NiO powder ESR spectra at room temperature from fine and coarse grains. The fine grains showed two signal A and B and the signal intensity of A increases linearly with

the mass of the powder being measured, which is consistent with the fact that paramagnetic center of Type A originates from the bulk of the sample as it is proportional to its mass and volume, and supports efficient hopping mechanism. On the other hand, the ESR spectra from coarse grains have also both signal A and B, and the ratio between signal B and signal A is significantly smaller in the previous sample. This sample is said to have a lower density of surfaces per unit volume, due to the large size of the grains. As such, signal B is assigned to defect relating to the surface of the grains. This was further ascertained with the varying measuring temperature of ESR signal intensity of fine-grain powder to be discussed in the next paragraph.

ESR signal intensity of fine-grain NiO_x powder sample versus varying temperature consist of two observed signals A and B stated in Figure 3.9. The intensity of signal B as a function of inverse temperature, showed neither Curie nor Pauli paramagnetism, but becoming constant below 120°K – a temperature that we identify as the Neel temperature below which signal B becomes constant, anisotropic, and likely confined in the proximity of the surface. This is consistent with the fact that the bulk of the sample becomes antiferromagnetic at about 120°K . Curie plot for the intensity of signal A, can be associated to localized bulk states, while signal B can be associated to extended surface states at $T < T_N$ and, at $T > T_N$, these states tend to extend towards the bulk of the sample being paramagnetic as the temperature increases. From this picture, both paramagnetic centers relating to signal A (which can be defects such as oxygen vacancies or Ni^{3+} centers) or magnetic systems relating to signal B (extended states at the surface or in the bulk of the material) may be responsible for the electrical transport in nickel oxide thin films. Hence, there is a need to discern the predominant paramagnetic centers responsible for the electrical conductivity of our sample.

Correlation between the spin density of the two magnetic centers; (the surface related signal B and bulk related signal A) versus conductivity was shown in Figure 3.11. A good linear relationship exists between the electrical conductivity and the spin density arising from signal A, and none with spin density corresponding to signal B. Therefore, conductivity must be related to the signal A, the localized bulk states. Further verification was made by considering the g-factor values of 2.14 and 2.022 for the localized point defects due to the

presence of Ni^{3+} ions centers or Ni^{2+} ions vacancies respectively. The g-factor value of 2.008 obtained for our NiO_x indicates that the magnetic center is due to oxygen vacancies. This finding emphasized that paramagnetic centers due to oxygen vacancies relating to signal A are predominantly responsible for the observed electrical conductivity in non-stoichiometric NiO_x thin film with minimal contributions from magnetic systems relating to signal B (extended states at the surface but at $T > T_N$, these states tend to extend towards the bulk of the sample being paramagnetic. In order to use NiO_x as an electrode such as in bulk heterojunction solar cell, its work function is highly essential.

Therefore, the work function of our NiO_x studied with KPFM is closer to the work function of PEDOT:PSS than those of ITO and graphene frequently used as electrodes in optoelectronic devices. Therefore, the NiO_x thin films can serve as possible replacement to PEDOT:PSS in heterojunction solar cell devices to evade most of the problems associated with PEDOT:PSS, such as degradation and high electrical resistivity. Also, with accurate energy level matching, the NiO_x thin films fabricated and annealed at 450 °C that showed optimal performance can serve as transparent electrodes, replacing cost intensive ITO and difficult-to-fabricate graphene.

4.2 Future work

As seen in section 3.2, higher annealing temperatures of 500°C and above do not favour good electrical transport in NiO_x materials. As a future work, the electrical conductivity of NiO_x annealed at temperatures above 550°C should be investigated to ascertain if the defect density is subject to quenching at such temperatures. In future, we intend to fabricate a bulk heterojunction solar cell by incorporating non-stoichiometric nickel oxide thin film to serve as hole transport layer electrode.

Appendix A: Copyright permissions

The permission granted by IOP publishing for reusing Figure 1.1, is presented.



Note: Copyright.com supplies permissions but not the copyrighted content itself.

1
PAYMENT

2
REVIEW

3
CONFIRMATION

Step 3: Order Confirmation

Thank you for your order! A confirmation for your order will be sent to your account email address. If you have questions about your order, you can call us 24 hrs/day, M-F at +1.855.239.3415 Toll Free, or write to us at info@copyright.com. This is not an invoice.

Confirmation Number: 11728003
Order Date: 07/02/2018

If you paid by credit card, your order will be finalized and your card will be charged within 24 hours. If you choose to be invoiced, you can change or cancel your order until the invoice is generated.

Payment Information

Angela Ezugwu
The University of Western Ontario
aezugwu@uwo.ca
Payment Method: n/a

Order Details

Journal of Physics : Condensed Matter

Order detail ID: 71278913
Order License Id: 4381100281714
ISSN: 0953-8984
Publication Type: Journal
Volume:
Issue:
Start page:
Publisher: IOP Publishing
Author/Editor: American Institute of Physics ;
Institute of Physics (Great Britain)

Permission Status: **Granted**

Permission type: Republish or display content
Type of use: Thesis/Dissertation

Requestor type: Academic institution

Format: Electronic

Portion: image/photo

Number of images/photos requested: 1

The requesting person/organization: Angela Ezugwu

Title or numeric reference of the portion(s): NiO portion of Figure 1,

Title of the article or chapter the portion is from: Accurate screened exchange band structures for the transition metal monoxides MnO, FeO, CoO and NiO

Copyright Clearance Center

Editor of portion(s)	N/A
Author of portion(s)	Roland Gillen and John Robertson
Volume of serial or monograph	25
Page range of portion	3
Publication date of portion	2013
Rights for	Main product
Duration of use	Life of current edition
Creation of copies for the disabled	no
With minor editing privileges	yes
For distribution to	Canada
In the following language(s)	Original language of publication
With incidental promotional use	no
Lifetime unit quantity of new product	Up to 499
Title	DEFECT-RELATED MAGNETIC PROPERTIES OF NANOSTRUCTURED NICKEL OXIDE THIN FILMS FOR SOLAR CELL APPLICATIONS
Instructor name	Giovanni Fanchini
Institution name	Western University Canada
Expected presentation date	Jul 2018

Note: This item will be invoiced or charged separately through CCC's **RightsLink** service. More info

\$ 0.00

Total order items: 1

This is not an invoice.

Order Total: 0.00 USD

CURRICULUM VITAE

ANGELA EBELE EZUGWU

HIGHLIGHTS

- MSc level researcher with background in experimental physics.
- Experience in nanomaterials synthesis, and implementation of new concepts and deposition techniques.
- A history of mentoring students and working with users on experimental projects in laboratory environment.
- Meticulous and detailed analytical thinker who works well independently or as part of a team.
- Excellent communication skills.

EDUCATION

- 2015–2018 **Master of Science (Physics)**, The University of Western Ontario, Canada.
Thesis: *Defect-Related Magnetic Properties of Nanostructured Nickel Oxide Thin Films for Solar Cell Applications.*
Supervisor: Prof. Giovanni Fanchini.
- 2011–2013 **Master of Science (Phys. & Ind. Phys)**, Nnamdi Azikiwe Uni Awka, Nigeria
Thesis: *Lead Sulphide/Zinc Sulphide Semiconductor Matrix Thin Films Using Chemical Bath deposition methods.*
Supervisor: Prof. P. I. Ekwo.
- 2005–2009 **Bachelor of Science (Solar Physics)**, University of Nigeria, Nsukka.
Project Title: *Growth and Characterization of Zinc Oxide Thin Films by Chemical Bath Deposition Method.*
Supervisor: Prof. B. A. Ezekoye.

TEACHING AND LEADERSHIP

- 2018 - date** **Volunteer Activity:** Organize the bi-weekly meetings of Giovanni's Research Group, Western University Canada.
- 2015 - 2018** **Undergraduate Laboratory Physics Demonstrator (140 hours per term):** Demonstrated and monitored labs of 35-40 undergraduate students, including grading of laboratory reports.
- 2004 - 2006** Precious Academy, Secondary School, Wukari, Taraba, Nigeria.
Responsibility: Teaching Senior Classes Mathematics and Physics.
- 2012 - 2013** Member Student Union Government, Nnamdi Azikiwe University Awka, Anambra State, Nigeria. **Responsibility:** Governor, Postgraduate Hostel.
- 2009 - 2010** University of Nigeria, Nsukka. **Responsibility:** Physics Demonstrator

Conference Presentations

- (8) **A.E. Ezugwu**, V. Wong, P. Bazylewski and G. Fanchini. Oral Presentation, "Are solar-cell antiferromagnetic nickel oxide transparent electrodes antiferromagnetic?". *International Conference of Energy, Materials and Photonics*, Montreal, Canada 8 – 11 July 2018.
- (7) **A.E. Ezugwu**, V. Wong, A. Akbari-Sharbaf and P. Bazylewski, and G. Fanchini. Oral Presentation, Electron Spin Resonance as a Probe of Defect-Related Magnetism in Nanostructures and Nanosystems. *101st Canadian Chemistry Conference and Exhibition* Edmonton Alberta May 27-31, 2018
- (6) **A.E. Ezugwu**, Paul Bazylewski and G. Fanchini. Oral Presentation, "Correlating Electrical Conductivity with Defects in NiOx thin Films". *The Canadian Semiconductor Science and Technology Conference (CSSTC)* Waterloo, August 20-24, 2017.

Publications

- (5) **A.E. Ajuba (Ezugwu)**, V. Wong, P. Bazylewski, G. Fanchini. Relationship between growth conditions, paramagnetic centers and electrical transport in nickel oxide thin films. Under preparation.
- (4) C.I. Amaechi, S.C. Ezugwu, F.I. Ezema, P.U. Asogwa. **A.E. Ajuba (Ezugwu)**. Composition, Optical and solid state properties of quaternary $\text{Cd}_{0.39}\text{Ba}_{0.28}\text{S}_{0.10}\text{O}_{0.23}$ thin films. *Journal of Non Oxides Glasses* 3(1), 1-7 (2011).
- (3) S.C. Ezugwu, F.I. Ezema, P.U. Asogwa. **A.E. Ajuba (Ezugwu)**, M.P. Ogbu, D.O. Eya. The effect of deposition time on the structural and optical properties ZnO thin film by aqueous chemical growth technique. *Digest Journal of Nano Material and Biostructure* 6(3), 1301 -1310 (2011).
- (2) **A.E. Ajuba (Ezugwu)**, S.C. Ezugwu, F.I. Ezema, P.U. Asogwa. Composition and optical characterization of ZnO/NiO multilayer thin film: Effect of annealing temperature. *Chalcogenide Letters* 7(10), 573-579 (2010).
- (1) **A.E. Ajuba (Ezugwu)**, S.C. Ezugwu, B.A. Ezekoye, F.I. Ezema, P.U. Asogwa. Influence of pH on the structural, optical and solid state properties of chemical bath deposited ZnO thin films. *Journal of Optoelectronics and Biomedical Materials*, 2(2), 73-78. (2010).